Dissertation
submitted to the
Combined Faculties for the Natural Sciences and for Mathematics
of the Ruperto-Carola University of Heidelberg, Germany
for the degree of
Doctor of Natural Sciences

presented by
Antje-Christin Knopf
born in Seeheim-Jugenheim, Germany
Oral exam: 22nd of April 2009

Physical and Clinical Potential of offline PET/CT Imaging after Proton Radiotherapy

Referees: Prof. Dr. U. Oelfke
Prof. Dr. T. Bortfeld

Zusammenfassung

Physikalisches und klinisches Potential von zeitversetzten PET/CT-Messungen nach Strahlentherapiebehandlungen mit Protonen

Bei der Behandlung von Krebserkrankungen mit Protonenstrahlen können empfindliche Gewebestrukturen direkt hinter dem Zielvolumen durch den schnellen Dosisabfall am Ende der Reichweite von Protonen vor Strahlung geschützt werden. Dieser ernorme Vorteil von Protonen wird jedoch nicht immer voll genutzt, da die Behandlungsplanung und -durchführung oft schwer einschätzbare Unsicherheiten beinhaltet. Die erfolgversprechendste In-Vivo-Methode zur nicht invasiven Kontrolle von Protonenstrahlbehandlungen ist die Positron Emissions Tomographie (PET). Positronenemitter, wie zum Beispiel ^{11}C und ^{15}O, werden bei nuklearen Reaktionen entlang des Strahlengangs produziert und können als räumliche Indikatoren für die deponierte Dosis genutzt werden. So lassen sich PET/CT-Messungen als Qualität sichernde Maßnahme zur Überprüfung der tatsächlich verabreichte Dosis und zur Quantifizierung von Unsicherheiten nutzen.

In dieser Arbeit werden die physikalischen und klinischen Möglichkeiten von zeitversetzten PET/CT-Messungen zur Behandlungskontrolle untersucht. In einer Phantom-Studie wird die physikalische Reproduzierbarkeit, die Konsistenz und die Sensivität der Methode erkundet. In einer Patienten-Studie wird ihre klinische Leistungsfähigkeit qualitativ und quantitativ betrachtet. Dafür werden Daten von 23 Patienten (9 Patientendatensätze wurden vor, 14 im Rhamen dieser Arbeit gesammelt) mit vielfältigen Tumorerkrankungen unterschiedlicher Art und Lokalitätern analysiert. Es werden Patientenuntergruppen bestimmt, die aus der Anwendung der Methode am meisten profitieren. Darüber hinaus werden technische und methodische Verbesserungen untersucht, die eine breitere Anwendbarkeit von PET/CT-Messungen zur Behandlungskontrolle bei der Strahlentherapie mit Protonen ermöglichen.

Abstract

Physical and Clinical Potential of offline PET/CT Imaging after Proton Radiotherapy

The rapid fall-off of dose at the end of range of proton beams has the potential of sparing critical structures just distal to the target volume. This tremendous advantage of protons is, however, not always used to its full extent, because treatment planning and delivery in proton radiotherapy often implies unpredictable uncertainties. The most promising method for an in vivo and noninvasive monitoring of proton radiotherapy is positron emission tomography (PET). Positron emitters such as ^{11}C and ^{15}O are produced via nuclear interactions along the proton beam path, and can be imaged as a spatial marker of dose deposition. This way PET/CT imaging can be employed as a quality assurance tool, to verify the actually delivered dose, and to quantify uncertainties.

In this thesis we investigate the physical and clinical potential of offline PET/CT imaging for proton treatment verification. In a phantom study we determine the physical reproducibility, consistency, and sensitivity of the approach. The presented patient study qualitatively and quantitatively evaluates its clinical performance. Data of 23 patients (9 patient data sets were acquired before, 14 within the framework of this work) with various tumor sites are analyzed. The influence of different challenging factors is studied with respect to different tumor locations. This way patient subgroups that benefit most from the approach are determined. Furthermore, possible technological and methodological improvements to allow for a wider applicability of PET/CT treatment verification are identified.

Preface

This PhD thesis was carried out at the Massachusetts General Hospital (MGH) between January 2006 and January 2009. The thesis describes the approach to verify dose distributions, delivered during the course of fractionated radiotherapy with protons, by PET/CT imaging.

Parts of this work have already been published in a paper called "Quantitative assessment of the physical potential of proton beam verification with PET/CT" [Kno08c] and a second paper called "Proton beam range verification with offline PET/CT scans - Clinical performance challenges and limitations" [Kno09], which will be submitted soon. Chapter 4 is mainly covered by the first papers [Kno08c], while chapter 5 widely presents the contents of the second paper [Kno09]. Parts of the work were presented at five international conferences [Kno07, Kno08a, Kno08b, Kno08d, Shi08]. For the contribution at the AAPM Conference 2007 in Minneapolis [Kno07], a second place as young investigator was awarded. The contribution at the ESTRO Conference 2008 in Gothenburg [Kno08d] was honored with the ESTRO Varian Research Award.

CONTENTS

1. INTRODUCTION

1.1 Cancer: disease and treatment

Cancer is a synonym for a suite of diseases with very different symptoms and courses. According to the American Cancer Society, 7.6 million people died from cancer in the world during 2007 [Acs07], corresponding to about 13% of all deaths per year [Who06]. For more than hundred years, researchers have explored the causes of cancer, have searched for diagnostic tools, and researched options for cure. The reasons for cells loosing operator control and turning cancerous are complex. Nearly all cancers are caused by abnormalities in the genetic material of the transformed cells. These abnormalities may be due to the effects of carcinogens such as tobacco smoke, radiation, chemicals, or infectious agents. Education campaigns and laws that restrict smoking in public attempt to decrease the cancer risk due to tabacco consumption. Radiation protection regulations and environmental legislation try to ameliorate the risk for cancer due to radiation and chemicals. The Nobel prize awarded development of a vaccine against cervical cancer raises the hope to control infectious agents as causes of cancer. However, besides these somehow controllable effects other cancer-promoting genetic abnormalities are acquired randomly through errors in DNA replication or are inherited and thus present in all cells from birth.

The possibilities and strategies of cancer therapy are as manifold as the manifestations of cancer. Cancer can be treated by surgery, chemotherapy, radiation therapy, immunotherapy, monoclonal antibody therapy or other methods. The choice of therapy depends upon the location and grade of the tumor, the stage of the disease, and the general state of the patient. The ultimate goal of cancer treatment is the complete removal of the tumor without damage to the rest of the body. The earlier the cancer can be diagnosed the more probable it is that this can be accomplished by surgery. However, the propensity of cancers to invade adjacent tissue or to spread to distant sites by microscopic metastasis often limits the effectiveness of surgery. Chemotherapy is the treatment of cancer with drugs that can destroy cancer cells. Chemotherapy drugs interfere with cell division in various possible ways, e.g. with the duplication of DNA or the separation of newly formed chromosomes. Most forms of chemotherapy target all rapidly dividing cells and are not specific for cancer cells. Hence, the effectiveness of chemotherapy is often limited by toxicity to healthy tissues in the body.

Aside from surgery and chemotherapy, radiation therapy is one of the three main options for treating tumors in patients. Radiation therapy (or radiotherapy) is the medical use of ionizing radiation to control malignant cells. Radiotherapy can be used as palliative treatment, where a cure is not possible and the aim is local disease control or symptomatic relief. Furthermore radiotherapy offers the possibility of therapeutic treatment, with the chance to cure the disease. Radiation therapy has been in use as a cancer treatment for more than 100 years, with its earliest roots traced from the discovery of X-rays in 1895. The concept of therapeutic radiation was invented by the German physicist Wilhelm Conrad Röntgen. The field of radiation therapy began to grow in the early 1900s largely due to the groundbreaking work of Nobel Prize-winning scientist Marie Curie-Sklodowska, who discovered the radioactive elements polonium and radium. This began a new era in medical treatment and research [UoA]. Radium was used in various forms until the mid-1900s when cobalt and caesium units came into use. Medical linear accelerators have been developed since the late 1940s. With Godfrey Hounsfields discovery of computed tomography (CT), three-dimensional planning became a possibility and created a shift from 2-D to 3-D radiation delivery. Orthovoltage and cobalt units have largely been replaced by mega voltage linear accelerators, useful for their penetrating energies and lack of physical radiation source. In the last few decades, the advent of new imaging technologies, e.g., magnetic resonance imaging (MRI) in the 1970s and positron emission tomography (PET) in the 1980s, as well as new radiation delivery and visualization products has moved radiation therapy from 3-D conformal to intensity modulated radiotherapy (IMRT) and eventually to image guided radiotherapy (IGRT) in the near future. These advances have resulted in better treatment outcomes and fewer side effects. Now 70% of cancer patients receive radiation therapy as part of their cancer treatment.

While the majority of irradiation involves high energy photons, there is a rising interest in treatments with proton beams as the number of clinical proton therapy facilities increases worldwide. The first suggestion that energetic protons could be an effective treatment method was made by Robert R. Wilson in a paper published in 1946 [Wil46] while he was involved in the design of the Harvard Cyclotron Laboratory (HCL). The first treatments were performed at Particle accelerators built for physics research, notably Berkeley Radiation Laboratory in 1954 and at Uppsala in Sweden in 1957. In 1961, a collaboration began between HCL and the Massachusetts General Hospital (MGH) to pursue proton therapy. Over the next 41 years, this program refined and expanded these techniques while treating 9116 patients before the Cyclotron was shut down in 2002. Following this pioneering work, the first hospital based proton treatment center in the United States was built in 1990 at the Loma Linda University Medical Center in Loma Linda, California (LLUMC) (recently renamed the James M. Slater Proton Therapy Center). This was followed by The Northeast Proton Therapy Center at Massachusetts General Hospital (recently renamed the Francis H. Burr Proton Therapy Center), to which the HCL treatment program was transferred during 2001 and 2002.

1.2 The need of treatment verification tools

One of the major advantages of proton therapy and heavy charged particle radiation therapy in general, is the possibility to deliver a high tumor dose while minimizing dose to healthy tissue. While penetrating material, electromagnetic as well as hadronic forces act on the ions. The most important interaction is the electromagnetic Coulomb interaction between the projectile and electrons, through which the ions continuously lose energy. The loss of energy increases with increasing depth of penetration. The description of this phenomena due to the Bethe-Bloch [Bet30, Blo33] equation leads to the characteristic depth dose curve for ions, known as the Bragg curve. The Bragg curve is characterized by a relatively low dose in the entrance region and a high-dose peak in the target. The finite beam range is the main advantage of the use of protons in radiation therapy. However, due to the steep dose gradient at the distal edge of each individual beam, uncertainties in the dose calculation and in the treatment delivery can have a profound impact on the applied dose. Slight errors may result in severe under dosage of the tumor volume and over dosage of the surrounding critical structures. Discrepancies between planned and actual delivered dose can be due to patient specific uncertainties like setup errors, motion and anatomical changes [Eng05]. Furthermore dosimetric uncertainties, like errors in the treatment planning algorithm, artifacts in the planning CT and ambiguity in the Hounsfield Unit (HU) conversion [Jia07] contribute to differences between planned and delivered dose. Solely the conversion from HU to stopping power can lead to a range uncertainty of about 1 - 3 mm in a typical treatment situation [Sch98].

Because of the steep dose fall-off, a very precise treatment delivery is important and strategies to verify the actual delivered dose and in particular the beam range in the patient are required. The complete stopping of the protons in the patient prevents the application of electronic portal imaging methods used in conventional radiotherapy. At present, the most promising method for in vivo and noninvasive monitoring of radiation treatments with proton beams is PET imaging.

A short historical overview of the use of PET imaging for proton treatment verification was given in [Par04]. Pioneering and very preliminary investigations on the potential of 2D on line imaging of β^+-emitting target fragments (mainly ^{11}C, ^{15}O and ^{10}C) induced by proton irradiation of phantoms and animals were carried out in Brookhaven at the end of the 1970s [Ben75, Ben78]. Starting from the beginning of the 1990s the topic was again addressed in preliminary phantom experiments using an on-line 2D array of scintillating detectors of low spatial resolution operated in coincidence as well as a commercial off-line PET system [Lit93, Lit99]. In the same year simulation studies [Del94] as well as off-line PET measurements after proton irradiation of phantoms [Paa93, Oel96] and of one patient [Vyn93] were done by various groups. Despite the common agreement on the potential usefulness of PET imaging for proton therapy monitoring, no definitive conclusion on the clinical feasibility and effectiveness was drawn. The lack of activation in the few last millimeter of penetration due to the energy threshold of about 15 - 20 MeV for the proton induced nuclear reactions, as well as the poor spatial correlation between β^+-activity and dose depth profiles were recognized as a nontrivial complication for the extraction of range information and dose localization [Oel96].

Instead of comparing the measured activity distribution and the dose distribution for treatment verification the challenge of their complex relation can be overcome by the use of predicted β^+-activity distributions. Following the approach of treatment monitoring for carbon ion therapy [En99, Poe04], detailed Monte Carlo (MC) simulated activity distributions can be used for validation [Par00, Par07c]. Alternatively, an analytical approach based on Gaussian power-law convolutions was proposed to calculate the expected activity distributions [Par06]. Extensive in beam phantom experiments carried out with proton beams at the Association for Heavy Ion Research (GSI) Darmstadt, Germany strongly encouraged the applicability and the accuracy of the method when comparing measured and expected activity distributions [Par02, Par05]. A recent phantom study [Par07a] and a clinical pilot study [Par07b] on a small population of 9 patients investigated the feasibility of offline PET/CT treatment verification for proton radiotherapy on site at MGH. It was shown that the beam range could be verified within an accuracy of 1 - 2 mm in low perfused bony structures of head and neck patients, for which an accurate co-registration of predominate bony anatomy was possible. At other positions and for other tumor sites, however, millimeter-accurate range verification failed. The most likely reason was attributed to limitations of washout and rigid co-registration, as well as motion uncertainties in the prolonged scan time of 30 min.

1.3 Aim and outline of the thesis

To employ PET/CT range verification clinically, it is crucial to know whether disagreements between measured and calculated activity maps reflect errors in the treatment planning, calculation or delivery, or whether they are caused by inherent limitations of the method. The aim of this thesis is the qualitative and quantitative specification of the physical and the clinical potential of offline PET/CT treatment verification.

The physical potential of the offline PET/CT approach, independent of and unaffected by other factors, is investigated in a comprehensive phantom study. The data analysis aims to:

- Test the reproducibility of the measured PET signal. The irradiation and PET scan of a phantom are repeated twice and activation depth profiles at identical geometrical positions within the phantom are compared.
- Test the consistency of the measured PET signal. Activation depth profiles within identical material arrangements, but at different positions within the irradiation field, are compared.
- Investigate the sensitivity of the PET/CT range verification method. Activation depth profiles through air/lung, air/bone and lung/bone interfaces parallel to the beam direction, as well as 6° angled, are studied to determine whether small range changes due to small tissue inhomogeneities are reflected in the measured PET signal.

The clinical potential is investigated for a larger population of 23 patients (9 patient data sets were acquired before [Par07b], 14 within the framework of this work) and a variety of tumor locations including the head, eye, spine, prostate and the sacrum. The following aspects are addressed:

- Restrictions on the accuracy of the offline PET/CT range verification method due to biological washout processes: Range verification ability is compared at positions where the proton beam ranged out in bone and at positions where the beam ranged out in well-perfused tissue.

- Effects on the accuracy of the offline PET/CT verification method due to patient motion: Lateral agreement between measured and simulated activity distributions for tumors in the thorax and abdomen are compared to the lateral conformity in head and neck tumor cases.

- Uncertainties in the MC-simulated activity distributions due to the restricted correlation in the mapping of HU to elemental compositions and washout characteristics: HU domains for different organs in the abdomen and pelvis are determined to investigate whether the HU mapping is sufficiently correlative to assign organ specific elemental compositions and washout characteristics in the MC simulations. To test the influence of uncertainties, MC simulations for different HU mappings are performed and compared.

- PET/CT range verification ability with respect to the tumor location: Patients were grouped and average absolute range deviations for different tumor locations were calculated. Site-specific challenges in addition to the three factors listed above are evaluated and an importance factor, indicating the degree of limitation on the PET/CT range verification method at this tumor location, is introduced for each aspect.

The general aim of this thesis is to identify the clinical extent of practicability of the investigated implementation of PET/CT treatment verification for proton radiotherapy, and to determine possible technological and methodological improvements to allow for wider applicability.

This thesis is organized as follows: The second chapter reviews the physical rationale of proton therapy, briefly describes factors that contribute to uncertainties in proton dose distributions, and gives an overview of strategies to handle these uncertainties. In chapter three, the physical background of the offline PET/CT verification approach is described and strategies how to predict activity distributions are introduced. Furthermore, the clinical implementation of PET/CT range verification from data acquisition to data analysis at MGH is described. The fourth chapter concentrates on the evaluation of the physical potential of offline PET/CT treatment verification, while the fifth chapter explores its clinical performance. The conclusions are summarized and discussed in the sixth chapter. An overview on the work in progress is given in the outlook. The appendix contains a flowchart of all steps involved in the PET/CT range verification approach, and gives practical advice on input parameters and adjustments of the different routines that needs to be run for a complete analysis.

2. TUMOR THERAPY WITH PROTON BEAMS

2.1 The physical basis of proton radiotherapy

The goal of radiotherapy with external beams is to deliver a dose distribution precisely localized in the tumor volume, while least affecting the surrounding healthy tissue and critical structures. As pointed out by R.R. Wilson [Wil46], the main argument for the use of protons in radiotherapy is their superior physical selectivity due to the lower energy, i.e. dose, in the entrance channel (plateau) and a steep increase and fall-off towards the end of penetration. Thus protons are highly suitable to deliver high tumor dose while sparing the surrounding tissue.

For protons passing through matter, the most important interaction is the electromagnetic Coulomb interaction with electrons, by means of which the protons continuously lose energy. The loss of energy increases with increasing depth of penetration. This is due to the fact that a proton with smaller velocity v has more time to interact with the electrons of the atom. The energy loss due to Coulomb interactions in a medium with a density ρ is described through the stopping power $S(E)$ of charged particles with energy E:

$$S(E) = -\frac{1}{\rho}\frac{\partial E}{\partial z}. \tag{2.1}$$

For charged particles with masses bigger than the electron mass m_e, $S(E)$ is analytically described by the Bethe-Bloch-equation [Bet30, Blo33]. For protons it reads:

$$S(E) = 0.307\frac{Z}{A}\frac{1}{\beta^2}\left(\frac{1}{2}\ln\frac{2m_ec^2\gamma^2\beta^2T_{max}}{I^2} - \beta^2\right) \tag{2.2}$$

The kinematic terms β and γ are defined as $\frac{v}{c}$ and $\frac{1}{\sqrt{1-\beta^2}}$; T_{max} denotes the maximum transferable energy to an electron and I is the mean ionization potential of the particular medium with the nuclear number A and the atomic number Z. The decrease of energy loss for charged particles in material as a function of the increasing velocity v becomes apparent through the relation $S(E) \propto \frac{1}{v^2}$. The Bethe-Bloch equation together with the statistical nature of the Coulomb interaction for an ensemble of protons [Oel02] leads to the characteristic depth dose curve for protons, known as the Bragg curve [Bra04].

Besides the electromagnetic Coulomb interaction with electrons, protons also undergo inelastic hadronic interactions with nuclei. Inelastic hadronic interactions have mainly two effects on the depth dose curve. As a first consequence the fluence distribution of the primary particles is exponentially attenuated in depth x according to the expression:

$$\phi(x) = \phi_0 e^{-N_{\sigma_R x}} \tag{2.3}$$

where ϕ_0 is the initial fluence, σ_R is the total crossection and N is the atomic density of the medium. This means the so far discussed depth dose curve for the Coulomb interaction has to be scaled down by a depth dependent factor. Furthermore, secondary particles produced in hadronic reactions contribute extra dose. For protons secondary particles can only be target fragments. Neglecting the heavy target fragments which stay almost at rest in the interaction place, the most important effect on the energy deposition is rendered by the production of secondary protons and neutrons liberated in (p, xp') and (p, xp'yn) reactions. From this yield only the secondary protons are found to give a significant dose contribution (up to 10% of the total dose at 160 MeV [Pag02]) in the proximal part of the Bragg-curve because of the lower energy spectrum with respect to the attenuated primary beam. Figure 2.1 shows calculated Bragg curves for proton energies between 59.4 MeV to 255 MeV in steps of approximately 2.5 MeV taking into account electromagnetic as well as hadronic interactions. The curves were simulated using Geant4 MC code.

The lateral part of charged particle dose distributions at a point with a given water equivalent path length η and a lateral distances x and y from the central ray can be approximated by a Gaussian distribution with a depth dependent sigma value [Nil01]:

$$L(\eta, x, y) = \frac{1}{\sqrt{2\pi\sigma_{x'}^2(\eta)}} \exp\left(-\frac{x^2}{2\sigma_{x'}^2(\eta)}\right) \times \frac{1}{\sqrt{2\pi\sigma_{y'}^2(\eta)}} \exp\left(-\frac{y^2}{2\sigma_{y'}^2(\eta)}\right) \tag{2.4}$$

$$\sigma_{x'}(\eta) = \sqrt{\sigma_x^2 + \sigma_{MCS}^2(\eta)} \tag{2.5}$$

$$\sigma_{y'}(\eta) = \sqrt{\sigma_y^2 + \sigma_{MCS}^2(\eta)} \tag{2.6}$$

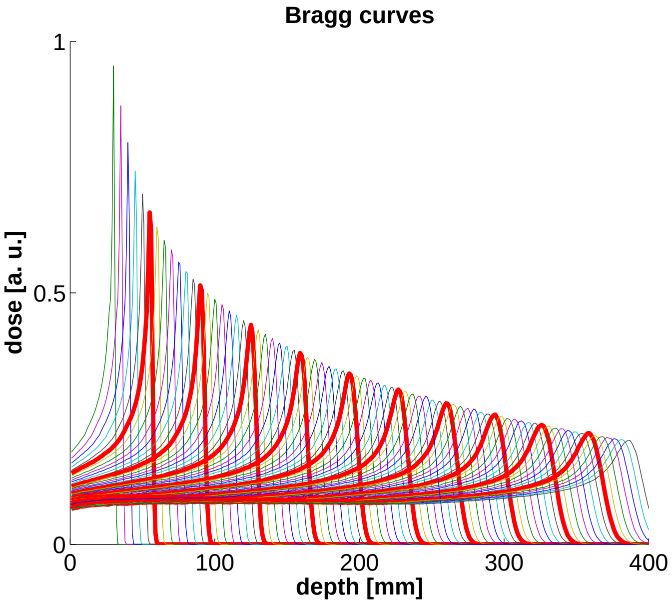

Fig. 2.1: 75 MC simulated Bragg curves for proton energies of 59.4 MeV up to 255 MeV

The sigma of the off-axis part of the pencil beam is split into two components.

> $\sigma_{x,y}$: Due to the finite size of the proton source and the scattering of the primary protons within the nozzle and the air gap between treatment head and patient, the proton beam already has a lateral extension before it enters the patient. The values that are used for both sigmas can be obtained by measuring the primary fluency with an ionization chamber in air.
>
> $\sigma_{MCS}(d)$: The beam broadening inside the patient is due to the multiple Coulomb scattering of the charged particles, and can be modeled by using a depth dependent sigma value. σ_{MCS} values for protons with energies between 59.4 MeV to 255 MeV in steps of approximately 2.5 MeV taking into account hadronic interactions are shown in Figure 2.2. The curves were simulated using Geant4 MC code.

Most tumor volumes are extended spatially and therefore demand three dimensional, uniform dose distributions. The longitudinal widening of the dose distribution is accomplished by a proper superposition of several Bragg-peaks of different depths to a spread out Bragg-Peak (SOBP). This can be either obtained through passive energy degraders (modulation

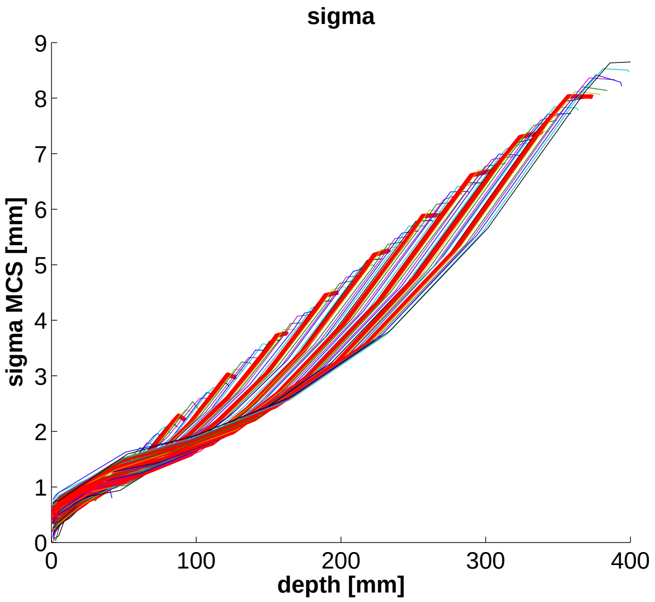

Fig. 2.2: σ_{MCS} distribution for protons with energies between 59.4 MeV and 255 MeV.

wheel) or active variation from the accelerator energy. A lateral spread of the dose distribution is achieved either by broadening the transverse beam profile by means of scattering systems, or by exploiting lateral magnetic deflection of pencil-like proton beams. To laterally shape a passively scattered broad treatment field to a desired target profile, custom milled apertures can be used. The distal part of the dose distribution can be shaped according to the desired treatment field using patient specific milled compensators. Figure 2.3 shows a sketch of the beam modeling devises used at MGH.

2.2 Uncertainty factors

Due to the steep dose gradient at the distal edge of proton beams, uncertainties can have a profound impact on the applied proton range. The numerous sources of uncertainty can be classified in patient and physics related.

Motion is one of the main patient related uncertainties. During treatment, motion can either cause density changes of traversed tissue (for example breathing motion during lung treatment), or displacements of different tissues within the beam path (for example bowel

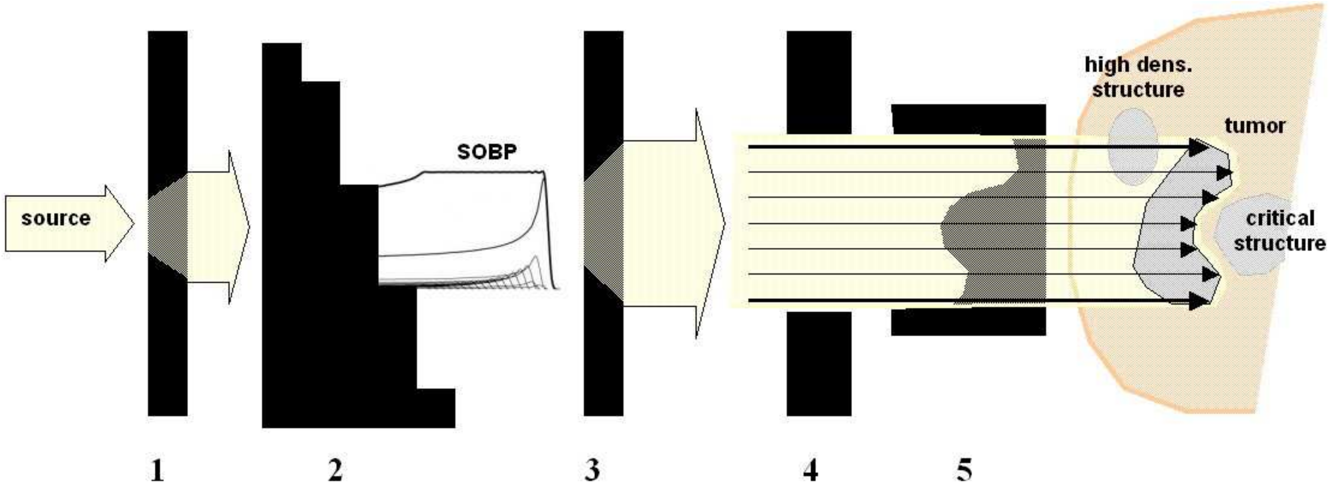

Fig. 2.3: Sketch of beam line element in the gantry-treatment rooms at MGH: 1. First scatterer, 2. Modulation wheel, 3. Second scatterer, 4. Patient specific aperture and 5. Patient specific range compensator

motion during prostate treatment) that effect the residual proton range [Eng05, Zha07]. Another patient related uncertainty factor is the daily setup. For prostate patient small variations in the leg positioning lead to different fractions of bone in the beam path which modify the proton range [Xu08]. Furthermore, during the course of fractionated proton treatment, the patient contours can change due to weight loss or gain. If this geometry change is not considered in the planned dose distribution it leads to deviations between planned and actual delivered proton range [Al08].

An example for a physics related uncertainty is the CT number conversion. For proton treatment planning CT Hounsfield numbers have to be translated in relative stopping powers. Empirical conversions are experimentally validated in tissue substitutes or samples, but cannot be directly verified within the patient [Schn96, Sch98, Schn00, Jia07] and thus contain uncertainties. Furthermore, the segmentation of the tumor and the critical structures based on medical images is inherently uncertain and error prone. For example CT artifacts can result in range overestimation at positions where a proton beam travels along a shaded region or to range underestimation at positions, where artifacts prevent an exact implant delineation [Jäk07]. Another source of physics related uncertainties of the proton range in radiotherapy is the dose calculation. Conventional treatment planning algorithms, based on pencil-beam dose calculations, have a limited capability to handle dose degradation due to Coulomb scattering in complex tissue inhomogeneities. Finally the dose delivery itself presents a source for uncertainties in the proton range.

2.3 Strategies to handle uncertainties

There are a variety of strategies to monitor and control each source of uncertainty in proton radiotherapy. Advances in 4D medical imaging, including time-resolved volumetric CT, magnet resonance imaging (MRI), PET, PET/CT, single photon emission computed tomography (SPECT) and ultrasound (US) allow to study, characterize, and minimize patient motion during the processes of imaging and radiotherapy [Li08]. To quantify the water equivalent path length variations resulting from respiration, analyzing tools based on 4D CT data [Mor08] have been proposed. The availability of advanced in-room imaging like cone-beam CT enables an on-line 3D target setup not limited to external patient information [Thi06]. Low-cost daily patient imaging detects and helps to account for contour changes in the patient during the course of fractionated proton treatment.

One promising way to handle the physics related problem of imprecise stopping powers for different tissue from conventional CT data is proton radiography [Koe68]. Through proton-computed tomography (pCT) direct information about the stopping powers of the therapy beam can be gained [Schn95]. Recent publications investigate the density and spatial resolutions of proton radiography [Ryu08] and report on the first proton radiography of an animal patient [Schn04]. One way to conquer deficiencies in conventional treatment planning is provided by MC simulations. MC methods have been applied to verify the results of the approximate dose calculation algorithms implemented in commercial treatment planning tools [Car97, Ma00]. They are considered to be the most accurate method to compute doses in radiation therapy, because simulations take into account the physics of particle interactions on a particle-by-particle basis using theoretical models or experimental cross-section data for electromagnetic and nuclear interactions [Pag08]. Currently, however, MC based treatment planning is not commercially available, mainly because of time inefficiency.

The tools mentioned thus far are only capable of controlling or monitoring specific sources of uncertainties. For treatment and quality assurance, in vivo verification tools that monitor *all* involved sources for range uncertainties are desired.

The unique time dependence of the dose rate function produced by range-modulated, passive-scattered protons was investigated recently for the use of in vivo range verification [Lu08]. By measuring such time dependence at the points of interest, the residual range of the proton beam at these points can be readily determined with millimeter accuracy, as long as these points fall in the plateau of the SOBP depthdose distribution. This approach would be capable of handling interactive adjustment of the proton range. However it only permits point wise verification of the delivered range and is limited to tumor sites that allow intra-cavity dosimeters in the beam path or implantable dosimeters with time-resolved external read-out. Another attempt for in vivo range verification is the use of prompt gammas. MC studies [Seo06] and preliminary experimental studies [Kie89, Min06, Bel07] indicate a correlation between the gamma distributions and the distal falloff region of proton beams. While this technique is very promising to verify the range at each position in the patient for scanned proton beams, it does not permit three-dimensional range verification in broad scattered proton beams.

PET/CT imaging is currently the only promising tool for in vivo range verification in passively scattered proton beams. It offers the unique advantage of direct verification of the applied three-dimensional contour of the distal dose ends.

3. PET IMAGING FOR PROTON TREATMENT VERIFICATION

3.1 The physical basis of PET imaging

In proton radiotherapy positron emitters are produced as a by-product in the penetrated tissue, as illustrated in Figure 3.1. Besides electronic interactions, protons undergo nuclear interactions where they can separate neutrons from nuclei in the tissue. The residual nuclei then undergo β^+-decays where a proton turns into a neutron under emission of a positron and a neutrino. Then, the positron annihilates with an electron from the surrounding tissue under emission of two photons in opposite directions which can be detected by PET scanners.

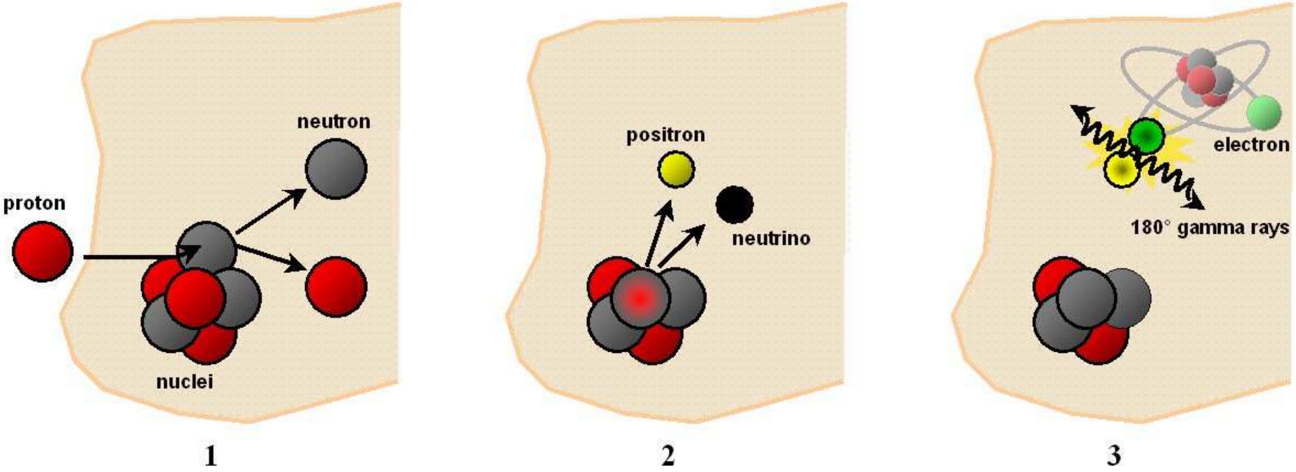

Fig. 3.1: β^+ decay: 1. Neutron separation, 2. Positron emission and 3. Positron annihilation.

β^+-emitting target fragments are produced along the penetration path until the energy of the primary protons drops below the threshold of nuclear reactions, which typically corresponds to few millimeters residual range in tissue. Energy thresholds for the main (p,pn) reaction channels leading to the production of ^{11}C and ^{15}O are 16.6 MeV and 20.3 MeV, respectively [Vyn93]. Experimental cross sections for (p,pn) channels yielding in positron emitters ^{11}C [Vas60, Gau62] and ^{15}O [Alb62, Saj85] are shown in Figure 3.2 [Nuc00]. Besides ^{11}C and ^{15}O also small fractions of ^{10}C, ^{13}N, ^{30}P and ^{38}K are produced.

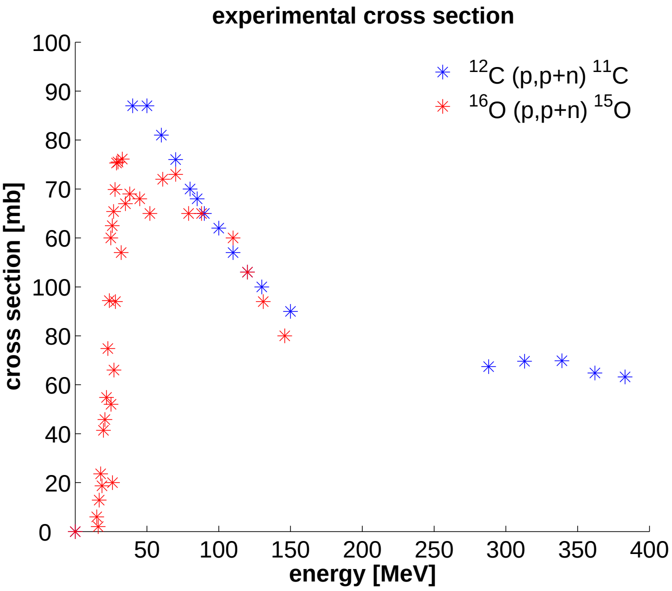

Fig. 3.2: Experimental cross section for the (p,pn) reaction on ^{12}C and ^{16}O nuclei [Nuc00].

The predicted total amount of β^+ emitters and the devision into the different nuclei produced within the treatment volume by a therapeutic proton irradiation of 1 Gy(RBE) target dose is shown in Figure 3.3. Gy(RBE) dose was computed using an REB of 1.1 for proton beams. The quantitative analysis in [Par04] supported the feasibility of PET signal detection during or shortly after a therapeutic proton irradiation. For on line data acquisition the signal from ^{12}C and ^{16}O nuclei is comparable as shown in the left graph of Figure 3.3. The ^{12}C fraction increases relative to the ^{16}O fraction with increasing delay between irradiation and PET scan as shown in the right graph of Figure 3.3. This is due to the different half-life $T_{1/2}$=20.39 min and $T_{1/2}$=2.03 min for ^{12}C and ^{16}O, respectively.

The produced neutron deficient nuclei can undergo a β^+ decay, where a positron e$^+$ and an electron neutrino ν_e is emitted:

$$A(Z,N) \rightarrow A(Z-1,N+1) + e^+ + \nu_e \tag{3.1}$$

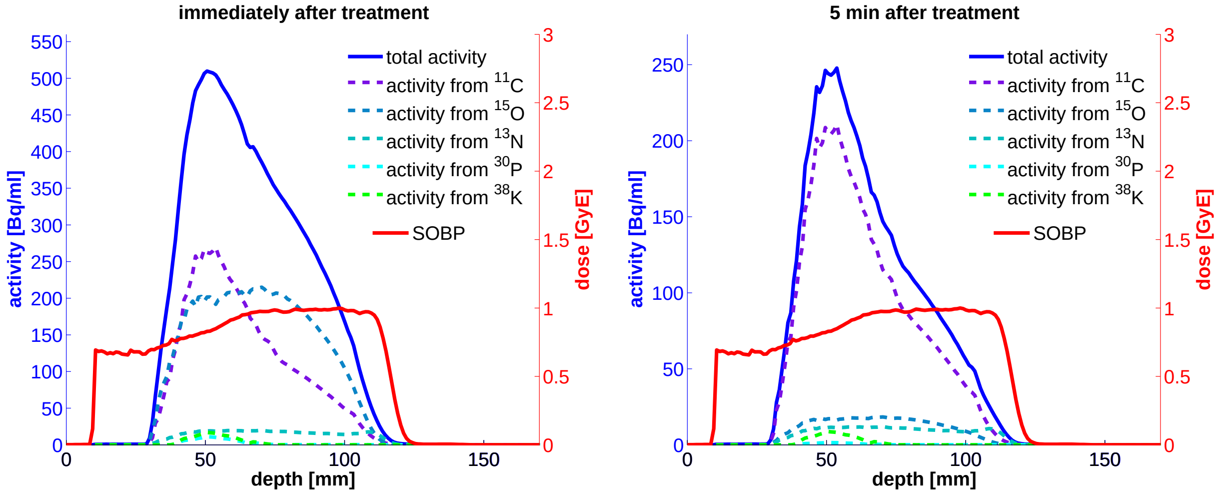

Fig. 3.3: Total and pro rata depth activity distribution from ^{11}C, ^{15}O, ^{13}N, ^{30}P and ^{38}K produced in a patient by proton irradiation resulting in 1 Gy(RBE) target dose according to FLUKA [Par07c] predictions at time 0 min (left) and 5 min (right) after the treatment. The calculated depth dose profile is additionally shown.

In this three-body decay the positron can share the available energy with the neutrino in an arbitrary proportion. Thus the energy spectrum of the positron is continuous up to maximum possible energy values. For the most abundant induced isotopes ^{11}C and ^{15}O these values lie between 1 and 2 MeV. The distance a positron travels through matter before it annihilates with an electron is a function of its initial energy and the electron density of the medium, and is typically $\simeq 4.5 \ldots 10$ mm in tissue. While the positron travels through tissue it loses energy in inelastic Coulomb collisions with atomic electrons and suffers several angular deflections. Once almost at rest, the positron either annihilates with an electron of the medium into two photons or captures an electron to form an unstable bound state. Possible bound states either annihilate into two or three photons. The 3γ-emission is however negligible and all the detectable radiation can be attributed to the 2γ annihilation.

The photons are emitted at almost 180° in opposite direction and carry each an energy of 511 keV equal to the positron and electron rest mass. The γ-ray pairs are isotropically emitted in the full solid angle of 4π and can be detected by couples of opposite detectors operated in coincidence. With tomographic acquisition techniques and suitable reconstruction algorithms it is possible to retrieve the spatial distribution of the β^+ activity source. The two basic assumptions of the reconstruction are that (i) the nucleus from which the positron originated is exactly located along the line at which the two photons are emitted and (ii) the two annihilation photons are emitted at 180°[Ben98].

The limited validity of the assumptions for the reconstruction algorithm, for example due to the distance the positron travels before annihilation, restricts the intrinsic achievable resolution of PET to 2-3 mm [Wie89]. This value is however below the $\simeq$ 5 mm practical spatial resolution of current commercial PET scanners. Their resolution is mainly determined by the dimension of the single detector units. Furthermore the attenuation of the photons within the scanned object, as well as the detection of random and scattered coincidence affect the measured data. These effects can however be well quantified and corrected.

A mono energetic proton beam and an SOBP proton field with the same maximal energy result in almost the same induced activity distribution, as shown in [Oel96] . This indicates that a depth dose profile cannot be uniquely determined from the proton induced activity pattern. Therefore this study mainly concentrates on the range verification rather than on the complete spatial verification of the dose distribution. The position of the distal activity fall-off is mainly influenced by the energy thresholds for the (p,pn) reaction channels leading to the production of ^{11}C and ^{15}O. The distance between the 50% level of the distal edge of the total positron emitter distribution and the dose maximum varys slightly, depending on the residual proton range at energies below the reaction thresholds and on the carbon to oxygen ratio of the medium composition. Depending on the time course of irradiation and the delay to the beginning of imaging, different isotopes contributed to the measured PET signal in a different extent as seen in Figure 3.3. Furthermore, biological washout effects redistribute the induced β^+ emitters. Ways to model these effect were introduced in [Par07a] and are described in subsection 3.2.1.

Because of the complex relation between dose and activity distribution, range verification has to be performed by comparing measured PET images with realistic predictions based on the individual treatment plan of the patient and the time course of the specific irradiation. Ways to perform reliable predictions of the induced activity pattern were described in [Par06, Par07c] and are discussed in section 3.2. Either CT-based MC simulated distributions as described in subsection 3.2.1 or analytical calculated distributions as described in subsection 3.2.2 can be used, both complemented by functional information.

3.2 Realistic prediction of induced positron emitters

3.2.1 MC simulations

As described in section 3.1 an essential step in the PET/CT treatment verification approach is the comparison of the measured activity distribution with calculated activity distributions. MC simulations based on the treatment plan, the planning CT data and the time course of irradiation and imaging provide a very realistic prediction for the induced activity pattern [En99, Poe04, Par07a, Par07c] due to the statistical nature of the involved processes.

The MC framework for the PET/CT range verification approach was mainly developed prior to the work of this thesis. MC simulations used in this work are based on two codes. The proton beam phase-spaces were obtained from GEANT4 based simulations [Ago03], which modeled the entire nozzle of our proton therapy facility [Pag04]. Although GEANT4 has been successfully employed for clinical dose calculations at the Francis H. Burr Proton Center [Jia04], the FLUKA MC code [Fas03, Fer05] was preferred to simulate the spatial activity distribution due to the traditional reliability of the FLUKA nuclear models [Pag03] and the good agreement with experimental PET data [Par02, Par05]. Besides activity patterns, dose, i.e., energy deposition per volume divided by the real density, was calculated for comparison with the treatment plan. All simulations were performed using phase spaces of about one million protons, corresponding to 3% (PET) and 5% (dose) statistical uncertainty, as a compromise between the conflicting requirements of sufficient statistics and low computational time. For normalization, an additional FLUKA simulation with the same input phase-space was performed in the water tank used for quality assurance dosimetry. An idivitual normalization factor for each treatment field (n $\approx (1-7)\times 10^3$) is given by the ratio of the prescribed to the simulated dose to water at isocenter.

Expected activity patterns were obtained from the simulation of the spatial distribution of positron emitters produced in tissue as described in [Par07b]. Positron emitter distributions were calculated by combining proton fluency with experimental cross sections. Besides the main (p,pn) channels on ^{12}C and ^{16}O, yielding ^{11}C and ^{15}O [Par02], respectively, further proton interactions with N, O, Ca, and P, resulting in ^{11}C, ^{13}N, ^{38}K, and ^{30}P production, respectively, were included. Shorter-lived emitters were neglected because of the low-production cross-sections and the offline PET imaging approach.

To get a realistic prediction for the measured activity distribution all involved effects, i.e. biological washout, scanner responds and image reconstruction have to be taken into account in the simulation. The spreading of the induced positron emitters due to biological washout processes is taken into account by means of space (i.e., tissue) and time-dependent weighting factors as described in [Par07b]. Previous animal studies on the washout of ^{10}C and ^{11}C implanted ions, or ^{11}C resulting from auto activation of ^{12}C beams, indicated the existence of a fast (biologic half-life $T_{1/2,biof} \approx 2-10s$), medium ($T_{1/2,biom} \approx 100-200s$), and slow ($T_{1/2,bios} \approx 3,000-10,000s$) component of biologic decay in rabbit thigh muscle and brain [Tom03, Miz03]. The fast and medium processes have already decayed in our offline approach at the time of imaging. Following the mathematical formulation of [Miz03], the slow biological effect is introduced as a space-dependent (i.e., tissue) and time-dependent weighting factor of the physical activity:

$$C_{bios}(r,t) = M_S(r)\exp(-\lambda_{bios}(r)t). \tag{3.2}$$

Values of the relative fraction M_S, and biologic decay constant $\lambda_{bios} = log_e 2/T_{1/2,bios}$ are, however, unknown for the various isotopes in human tissues. For the sake of simplicity, tissue is classified into low, intermediate, and normal perfused, and differences between the metabolisms of different isotopes are neglected. Thresholds are set on the planning CT to identify fat (-150 $\leq$ HU $\leq$ -30), soft bone (200 $\leq$ HU $<$ 1000) and compact bone (HU $\geq$ 1,000). For the low-perfusion fat and compact bone, M_S and $T_{1/2,bios}$ are set to 0.9 and 15,000 s, respectively. In soft bone, intermediate values of M_S and $T_{1/2,bios}$ are approximated to 0.6 and 8,000 s. For all remaining tissue, an average value of M_S = 0.55 and $T_{1/2,bios}$ = 3,500 s is used in spine sites, while a value of M_S = 0.35 and $T_{1/2,bios}$ = 10,000 s is used for head sites, based on the results of animal studies in muscle and brain, respectively [Miz03]. While the biological washout processes are not only different for different tissues, they also possibly vary from day to day, or in respect to the time point of PET imaging during the treatment course. Radiation can have a significant influence on the metabolism of tissues as shown in [Kes08], which can for example result in different oxygen levels in tissues at different phases of treatment.

For full-ring tomography, blurring from image formation and reconstruction can be reasonably modeled by a three-dimensional (3D) Gaussian convolution kernel $G(r)$ according to [Par07a, Par07b]. A PET image, averaged on a time frame of duration t_{frame} starting with a time delay Δtt after the end of irradiation can be obtained as follows:

$$G(r) \;\; * \;\; \Bigg(\sum_i n_i \cdot \sum_j [M_S(r) N_{ij}(r) \cdot \frac{[1-\exp(-\lambda_j t_{irr,i})]}{t_{irr,i}} \cdot \exp(-\lambda_{tot,j}(r)\Delta t) \cdot \frac{[1-\exp(-\lambda_{tot,j}(r) t_{frame})]}{\lambda_{tot,j}(r) t_{frame}}] \Bigg) \qquad (3.3)$$

This equation adds up the activity contributions from the calculated amount N_{ij} of isotopes of species j, formed by each delivered field i. n_i is the normalization factor for the considered field, M_S is the slow biologic decay fraction, and λ_j and $\lambda_{tot,j}$ are the isotope-specific physical and total (i.e., physical plus biologic) decay constants, respectively. The slow biological decay during the short irradiation time ($t_{irr,i} \approx 10$ to 100 s) is neglected. Figure 3.4 shows a comparison between a measured and the corresponding MC simulated activity distribution.

Currently, MC simulations of dose and activity distributions are only possible for treatments in the gantry rooms at MGH, since the geometry of the fixed lines is not jet implemented. Problems and uncertainties of the MC approach will be discussed in section 5.4.4.

3.2.2 The filtering approach

A simpler and more direct way to reconstruct the expected PET signal is described in [Par06]. Under reasonable assumptions, the PET image can be described as a convolution of the dose distribution with a filter function. The reaction depending filter functions can be determined analytically using convolutions of Gaussian and power-law functions. The advantage of this filter approach is that the expected activity distribution can be determined locally, in contrast to the MC simulation that requires the consideration of all involved processes along the entire beam path. The filtering approach is thus less sensitive to uncertainty factors like tissue inhomogeneities or artifacts along the beam penetration.

Activation profiles achieved from the filtering approach have been validated against MC calculations and measurements in homogeneous and inhomogeneous phantoms [Par06, Att08]. Good agreement in position in depth as well as in terms of absolute intensity could be achieved. Figure 3.5 shows a preliminary comparison between a measured and the corresponding filtered activity distribution in a patient. In the filtered activity distribution only the contribution of ^{11}C. For in vivo activity predictions the filtering approach faces several

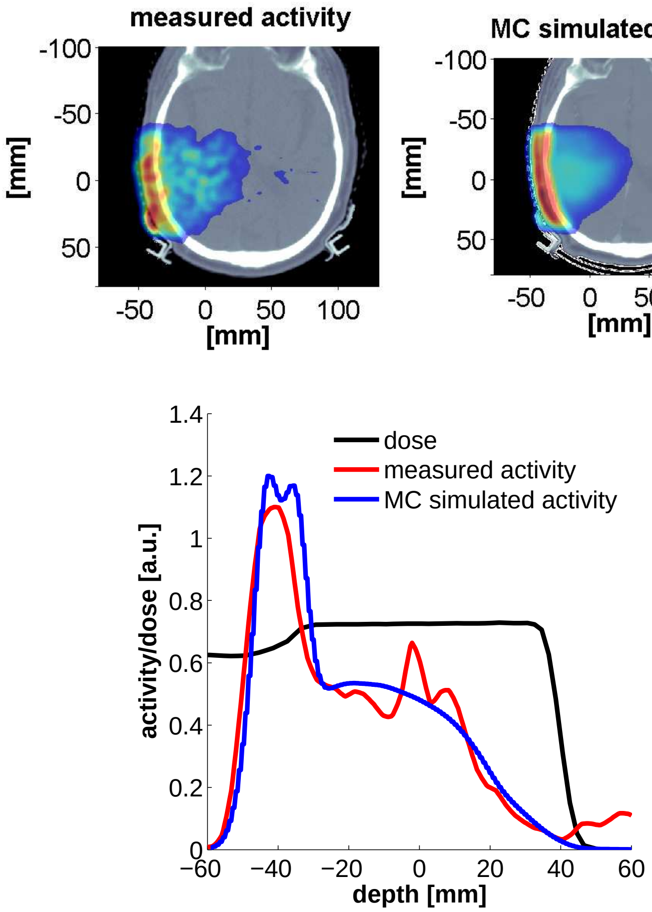

Fig. 3.4: Comparison of a measured (upper left) and the corresponding MC simulated (upper right) activity distribution. The lower figure shows the depth dose distribution at position zero together with the corresponding activity profiles.

challenges, since it for example does not take into account biological effects due to perfusion and washout processes as well as statistical effects. Similar to the MC approach these could be added as additional convolution with a Gaussian kernel and probability weighting factors of the produced activity on the basis of available functional information. However, the filtering model is also limited to one spatial dimension along the direction of beam penetration. In cases of high curvature of the distal surface of the dose distribution, or for very small stereotactic fields, an extension of the model to two or three dimensions will be necessary. Throughout this thesis MC simulated activity distributions are used for validation mainly because this approach is more common and has been studied by several groups [Del97, Psh06, Par07c].

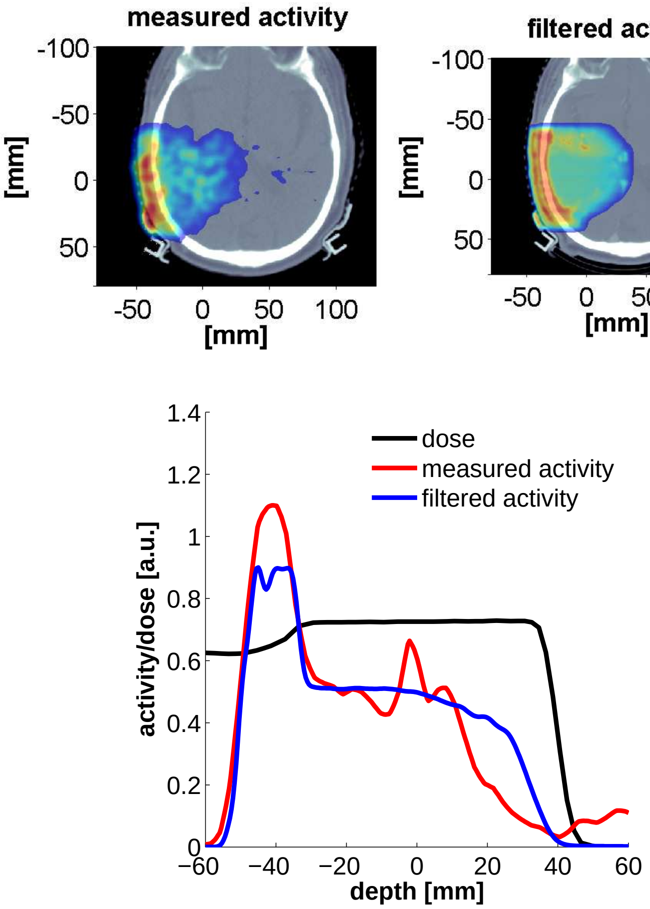

Fig. 3.5: Comparison of a measured (upper left) and the corresponding filtered (upper right) activity distribution. For the filtered activity distribution biological washout processes are not taken into account. The lower figure shows the depth dose distribution at position zero together with the corresponding activity profiles.

An inversion of the filter functions allows direct dose quantification from the measured PET distributions. This approach requires PET data of excellent signal-to-noise ratio and negligible influence of biological processes. Both requirements are somewhat difficult to fulfill with off-line imaging strategies. In section 7.3 an overview about the work in progress concerning the filtering approach is given.

3.3 Clinical implementation

3.3.1 Procedure at MGH

In the procedure currently performed at MGH suitable patients receive the opportunity to participate in the Investigational Review Board approved study of PET/CT treatment verification. The investigational protocol allows for a single or repeated PET/CT scan during the course of fractionated proton radiotherapy. For repeated PET/CT data acquisition scans are performed at two different treatment days during one week. Immediately after completion of one treatment session at the F.H. Burr Proton Therapy Center patients are walked to the next PET/CT scanner, available within 15 min walking distance. During this study two PET scanners were used, a Biograph Sensation 16 and a Biograph 64. The PET detectors have a transaxial field of view (FOV) of 605 mm and an axial FOV of 16.2 mm. The resolution of the PET cameras is about 4.2 mm around the center and 5.5 mm at radiuses as large as 10 cm. PET/CT data is acquired and reconstructed according to a protocol specifically designed for this study. The integral distribution of PET activity is obtained from filtered back projection (FBP) or iterative (ordered subsets expectation maximization, OSEM) reconstruction of all measured activity data. OSEM reconstructed data is preferred for data analysis because of reduced fluctuations, especially in the low-activity region at the edge of the field of interest, allowing for more accurate range verification.

When possible, PET/CT imaging is performed in the same patient position and with the same immobilization as during the treatment. Differences in patient positioning during irradiation and PET/CT imaging are taken into account by rigid co-registration of the planning CT and the PET-CT performed via commercial FOCAL software (Computerized Medical Systems, Inc., St. Louis, MO). Images coregistered allows the comparison of the measured PET distribution with the planned dose and its corresponding PET expectation. The latter can be obtained from CT-based MC calculation as described in section 3.2 or from an analytical model as described in section 3.2.2, both complemented by functional information. The whole process from the data acquisition to the data analysis is schematically outlined in a work flowchart in the appendix.

The clinical pilot study [Par07b] investigated the feasibility of PET/CT treatment verification in a small population of 9 patients with tumors in the cranial base, spine, orbit and eye. Thereafter the patient population was extended to also include abdomino pelvic tumor sites like prostate and sacrum. Table 3.1 gives detailed information on the tumor site, the dose per field, the delay between irradiation and imaging and the number of fields delivered in each patient at the day of the PET/CT scan. Except for two patients (#22, #23) that underwent repeated imaging, all patients participated in a single PET/CT imaging after one treatment session. Irradiation was performed in gantry-equipped treatments rooms except for two patients (#8, #17) who were treated on a fixed horizontal beam line. PET data were acquired in list mode at a Biograph Sensation 16 for the first 11 patients and at a Biograph 64 PET/CT scanner for the remaining patients.

For the phantom measurements the same protocol as for the patients was performed. Details are given in section 4.2.

3.3.2 Offline versus on line PET imaging

In this work all results are based on offline PET/CT data acquisition. The long time interval between irradiation and imaging prevents the acquisition of the contribution from ^{15}O ($T_{1/2}$ = 121.8 s), which might offer the possibility of addressing tumor hypoxia and treatment response. A reduction of the time between irradiation and PET/CT imaging possibly also reduces the influence of biological washout processes. The clinical benefit of on line PET imaging is however still questionable. Practically, it is hard to find a geometrical scanner solution within the treatment room that offers comparable 3D data acquisition as in the offline approach in terms of signal efficiency. Furthermore in room scanners are affected by scattered treatment radiation and limit the treatment flexibility and the patient throughput [Cre06]. Due to the limitation to target fragmentation, proton induced PET activity is especially sensitive to tissue elemental composition. On line data acquisition may be considerably affected by minor target fragmentation reaction channel [Par05]. Since the exact elemental tissue composition in patients is unknown, these activation channels are difficult to model. Validation, which depends on predicted activity patterns, becomes more vague the more activation channels contribute. This source of uncertainty is reduced in the considered offline scenario, due to the small number of production channels yielding long-lived positron emitters. Work in progress concerning on line PET measurements at the F. H. Burr Proton Center is described in chapter 7.1.

Patient #		**1**[*]	**2**[*]	**3**[*]	**4**[*]	**5**[*]	**6**[*]	**7**[*]	**8**[*]	**9**[*]	**10**	**11**	**12**	**13**	**14**
Tumor location	Head		X			X	X			X	X	X			
	Eye								X						
	C-spine							X						X	
	T-spine												X		
	L-spine	X		X											
	Sacrum				X										
	Prostate														X
Dose per field [Gy(RBE)]		2	0.9	0.9	2	0.9	0.9	0.9	10	3	1	2	1.8	1	2
Delay between irrad. and PET/CT imag. [s]				935	984						728	736	993	727	1065
Opposed beam directions													X		
# of fields	1	X			X				X	X		X			X
	2		X	X		X	X	X			X		X	X	

Patient #		**15**	**16**	**17**	**18**	**19**	**20**	**21**	**22**	**22**[§]	**23**	**23**[§]	**total**
Tumor location	Head			X	X	X	X	X			X	X	**12**
	Eye												**1**
	C-spine								X	X			**3**
	T-spine												**1**
	L-spine												**2**
	Sacrum	X											**2**
	Prostate		X										**2**
Dose per field [Gy(RBE)]		1	2	0.9	1	1	0.9	1	2.5	2.5	8	8	**0.9-10**
Delay between irrad. and PET/CT imag. [s]		686	885	912	852	706	1029	1465	873	830	828	735	≈ **890**
Opposed beam directions		X			X								**3**
# of fields	1		X					X	X	X			**9**
	2	X		X	X	X	X						**13**
	3										X	X	**1**

Tab. 3.1: Treatment and imaging parameters for the 23 patients that received a PET/CT verification scan at MGH. (*: Patients were reported in [Par07b], §: Repeated PET/CT data acquisition)

The use of time of flight (TOF) PET scanners could give a technical advance. Activity measurements for proton treatment verification are challenged by the low signal compared to conventional tracer PET images. The poor signal to noise ratio can be substantially improved by the TOF technique. Scan times can be reduced in TOF scanners to achieve images similar to those from non TOF scanners, or improved image quality can be achieved for same scan times [Sur06]. With the time to obtain an image being smaller than the typical irradiation time, direct TOF-PET could allow accurate, artifact-free images to be shown to the oncologist in real-time, during the course of irradiation, as long as a corresponding real-time data acquisition is provided [Cre07].

3.4 Data analysis

3.4.1 Different strategies: 2D

A MATLAB-based (MathWorks, Inc., Natick, MA) code was developed to compare planned and MC-simulated dose distributions, as well as measured and calculated PET/CT images, all superimposed or coregistered to the planning CT [Par07a, Par07b]. The Matlab routine requires a working memory of at least 4 GB and is controlled over the Matlab command window. The data has to be prepared in advance to fulfill the format obligations. In the appendix a list of needed input parameters and a detailed description how to prepare the data for the final analysis is given.

For a first qualitative analysis 2D color-wash distributions of the simulated and measured activity can be visually compared. Within the framework of this thesis the ability to obtain 2D difference plots that give an idea about the absolute agreement of the two distributions was implemented. Furthermore, for a quantitative and simultaneous evaluation of absolute and distance to agreement between measured and simulated activity distribution, the feasibility to perform a gamma index analysis [Low98] was established. Ways to obtain reasonable absolute values and spatial pass-fail criteria for the gamma index analysis are discussed in section 5.3.1.

Throughout this thesis absolute values below a threshold of 8% (5%) of the maximum activity are omitted in the color-wash display (gamma index evaluation) to inhibit the distracting influence of noise in the measured data.

3.4.2 Different strategies 1D

Range verification can be performed by comparing depth profiles at 20% and 50% position of the last activity maximum in the final distal fall-off region as illustrated in Figure 3.6. Method A will refer to comparing depth profiles at the 20% position and method B at the 50% position of the last activity maximum. The proper choice of the range verification position in the fall-off region in clinical practice is controversial and was discussed in [Par07a, Par07b, Kno08c]. The 20% fall-off position is more affected by background noise than the 50% position. Furthermore, the 20% fall-off position in the simulated depth profiles is sensitive to the chosen FWHM in the Gaussian point-spread function that accounts for blurring effects and reconstruction. Therefore, the 50% fall-off position is more reliable.

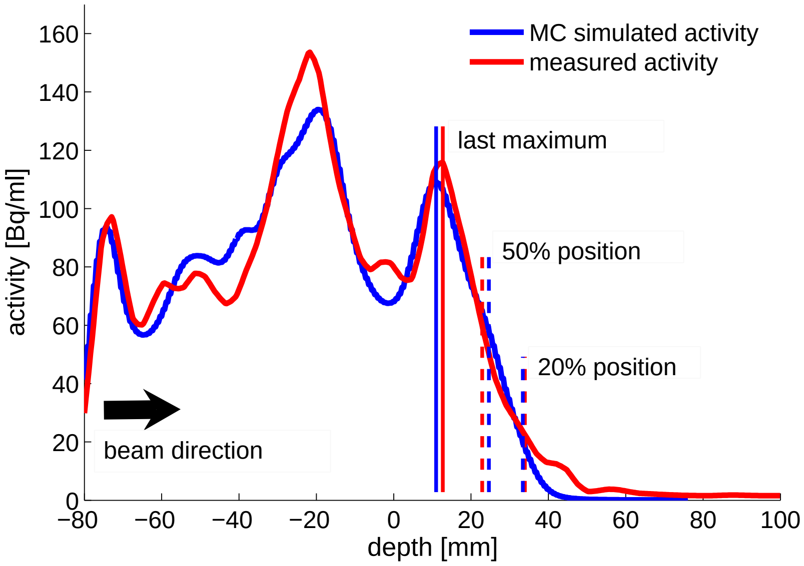

Fig. 3.6: Illustration of point wise range verification at the 20% and the 50% position of the last activity maximum in the final distal fall-off region.

Apart from a range comparison at specific positions in the fall-off region, a range analysis taking the entire fall-off region $A(x)$ into account was established within the framework of this thesis. The range difference R_{diff} between two depth profiles is determined here by shifting their normalized fall-off regions against each other until the minimum of the sum of absolute differences in the activity values $A_{meas} - A_{ref}$ is found:

$$R_{diff} = \arg\min_{\delta} \left(\sum_{i \in M} |A_{meas}(x_i) - A_{ref}(x_i - \delta)| \right) \tag{3.4}$$

δ typically ranged from -20.0 mm to +20.0 mm in steps of $\approx$ 0.5 mm. M is a set of indices with corresponding x_i in the interval $[x_m, x_e]$, were x_m is the position of the last maximum in the activity depth profile and x_e is the end of the activity depth profile. The δ for which the minimum is found corresponds to the range difference between the two depth profiles. The shift method is currently the most robust analyzing strategy. It is insensitive to gradient assumptions for the Gaussian point-spread function and the influence of background noise is negligible. In most cases it gives values between the 20% and 50% fall-off position results. The accuracy of the method rises with the shallowness of the shifted profile regions. We will refer to this shift analyzing strategy as method C in this thesis.

Throughout this thesis positions at which range verification failles because of known reasons, such as CT artifacts or the delivery of opposed fields in the same treatment fraction, are excluded. Large range deviations resulting from an obvious failure of the method of analysis, for example due to a lack of characteristic similarity in the activity profiles, are also excluded.

4. PHYSICAL POTENTIAL OF PET TREATMENT VERIFICATION

4.1 Introduction

PET measurements in patients are challenged by several factors. The measured PET signal is washed out by blood perfusion and can be further blurred by patient motion during the data acquisition. In addition the comparison of simulated and measured PET images is affected by the ambiguous translation of CT numbers into material compositions that introduce uncertainties in the simulated PET image. The rigid image co-registration of the planning CT and the PET CT, which neglects deformations of the complex patient geometry, results in further uncertainties. These challenges in the patient measurements are discussed in detail in the section 5.4.2, 5.4.3, 5.4.4 and 5.4.5. They make it difficult to assess the pure physical potential of in PET/CT range verification.

The present phantom study investigates the physical potential of PET/CT range verification independent of and unaffected by other factors. Emphasis is placed on the qualitative and quantitative investigation of the measured PET signal. The data analysis aims to:

- Test the reproducibility of the measured PET signal. The irradiation and PET scan of the phantom were repeated twice and activation depth profiles at identical geometrical positions within the phantom are compared.

- Test the consistency of the measured PET signal. Activation depth profiles within identical material arrangements, but at different positions within the irradiation field, are compared.

- Investigate the sensitivity of the PET/CT range verification method. Activation depth profiles through air/lung, air/bone and lung/bone interfaces parallel to the beam direction as well as 6° angled are studied to determine whether small range changes due to small tissue inhomogeneities are reflected in the measured PET signal.

Medium	H(%)	C(%)	N(%)	O(%)	Mg(%)	Cl(%)	Si(%)	Ca(%)	δ(g cm^{-3})
PMMA	8.05	59.99		31.96					1.18
bone eq.	3.41	31.41	1.84	36.50		0.04		26.81	1.82
lung eq.	8.46	59.38	1.96	18.14	11.19	0.10	0.78		0.30

Tab. 4.1: Elemental composition (fraction by weight) and density of the plastic and tissue equivalent materials (information provided by the manufacturer Gammex Inc.).

4.2 Methods

4.2.1 Phantom irradiation

The in-house designed phantom consisted of polymethyl methacrylate (PMMA), lung and bone equivalent tissue slabs (cf. Table 4.1), which were arranged to form air/lung, air/bone and lung/bone interfaces. These interfaces were positioned once parallel and once in a 6° angle to the beam direction. A sketch of the phantom can be seen in Figure 4.1C.

The phantom was irradiated with a 15.7 cm diameter circular spread-out Bragg-peak (SOBP) proton field of 15 cm and 10 cm water equivalent range and modulation, respectively, to cover the whole geometry. The beam direction was vertical to the material slabs as shown in Figure 4.1A. It was chosen to deliver a total dose of 8 Gy(RBE) in order to get a high signal to noise ratio despite the approximately 14 min delay between irradiation and the PET/CT scan. Besides the main data analysis on the measured activity over the whole 30 min of imaging, also a low-statistics data analysis of only the first 11 min of imaging was performed. This corresponds to a situation in which only half of the dose would have been delivered. With this low-statistics analysis way we made sure that the derived results are also valid for a typical in vivo measurement, where a patient received one or two treatment fields of $\approx$ 2 Gy(RBE) at the day of PET/CT imaging.

PET data were acquired in list mode at a Siemens Biograph 64 PET/CT scanner according the protocol used for patient measurements. The orientation of the phantom was approximately the same at the PET/CT scanner as during the proton irradiation (Figure 4.1B). Minor differences in the positioning were taken into account by co-registering the planning CT (voxel resolution: 0.648 mm x 0.648 mm x 2.5 mm) with the PET CT (voxel resolution: 0.4883 mm x 0.4883 mm x 3 mm) which was acquired directly prior to the PET imaging. For comparison all data sets were superimposed to the planning CT grid after co-registration.


A) Proton Treatment at the F. H. Burr Proton Therapy Center

B) PET/CT scan at a Siemens Biograph 64 TruePoint PET/CT

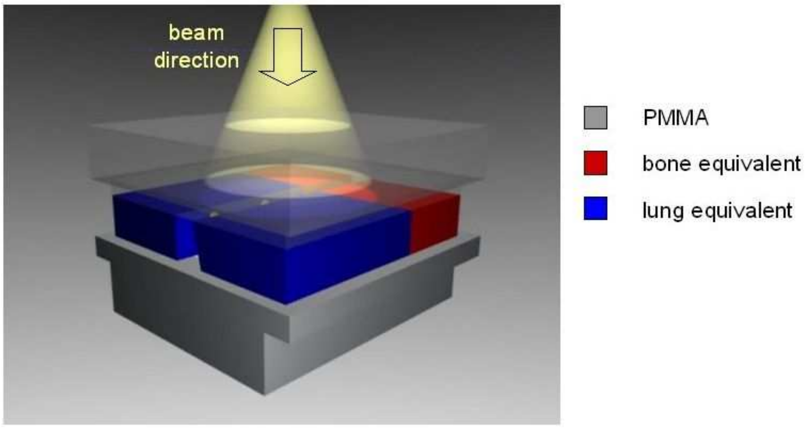

C) sketch of the phantom

Fig. 4.1: A) phantom irradiation, B) phantom PET/CT scan and C) phantom layout.

PET image reconstruction was done at 1.3364 mm x 1.3364 mm x 2.025 mm voxel dimension which, in consideration of the 4 mm crystal size of the PET detector, was found to be a good compromise between high spatial resolution and low statistical noise.

4.2.2 Phantom simulation

Validation was achieved by comparing the measured activity distribution with corresponding MC simulated distributions, that were based on the treatment plan, the planning CT data and the time course of irradiation and imaging as described in section 3.2.1. All simulations were performed using phase spaces of about one million protons (compromise between the conflicting requirements of sufficient statistics and low computational time). The geometric information regarding the phantom was extracted from CT. This was preferred compared to a direct implementation since the phantom geometry contains some irregular shapes. HUs were segmented into air (HU $<$ -900), lung (-900 $\leq$ HU $<$ -500), PMMA (-500 $\leq$ HU $<$ 535) and bone (535 $\leq$ HU $<$ 2000). The exact elemental compositions and densities of the materials were assigned to each HU interval. The sharp segmentation of the HU is sensitive to partial volume effects (PVE). At each interphase, corresponding to at least 3 voxels in our phantom geometry, a voxel consisting e.g. partly of air and partly of PMMA will be identified either entirely as air or PMMA. The PVE is not that relevant in typical patient cases due to the piecewise linearity of the calibration curve and its evaluation at the average HU value between the two materials. In this phantom study measured activity distributions were compared to MC simulated activity distributions only relatively. These comparisons were insensitive to the absolute agreement between measured and simulated activity distributions, and thus to systematic discrepancies of the measurement and the MC simulation.

4.2.3 Testing the reproducibility of the measured PET signal

To test the reproducibility of the measured PET signal, the irradiation and the PET scan of the phantom were performed twice under nearly identical conditions. Proton range values measured in the daily quality assurance protocol at our gantry are consistent within 0.3 mm standard deviation over a time of three months. Slight differences in the time course of irradiation and PET scan between the two measurements are summarized in Table 4.2. The short interruption in the time course of the first data acquisition was due to a short interruption in beam delivery. We verified that the impact on the activity depth profiles due to the small variations in the time course is negligible. For both data acquisitions the same number of monitor units (MU) was given.

ID	$\mathbf{t}_{irr}$**(sec)**	**ΔT(sec)**
1	138±3 (time course: 0 - 35 (199 MU) + 107 - 210 (589 MU))	799±3
2	129±3 (time course: 0 - 129 (788 MU))	756±3

Tab. 4.2: Parameters of the two data acquisitions: ID, irradiation time (time course of irradiation), delay to the beginning of imaging.

Even though a single repetition of the irradiation and PET scan of the phantom cannot statistically ascertain the reproducibility of the method, it gives an indication whether the method is restricted by the physical reproducibility. The two measured datasets were compared at 12 benchmark positions, which can be seen with respect to the beam position in Figure 4.2b.

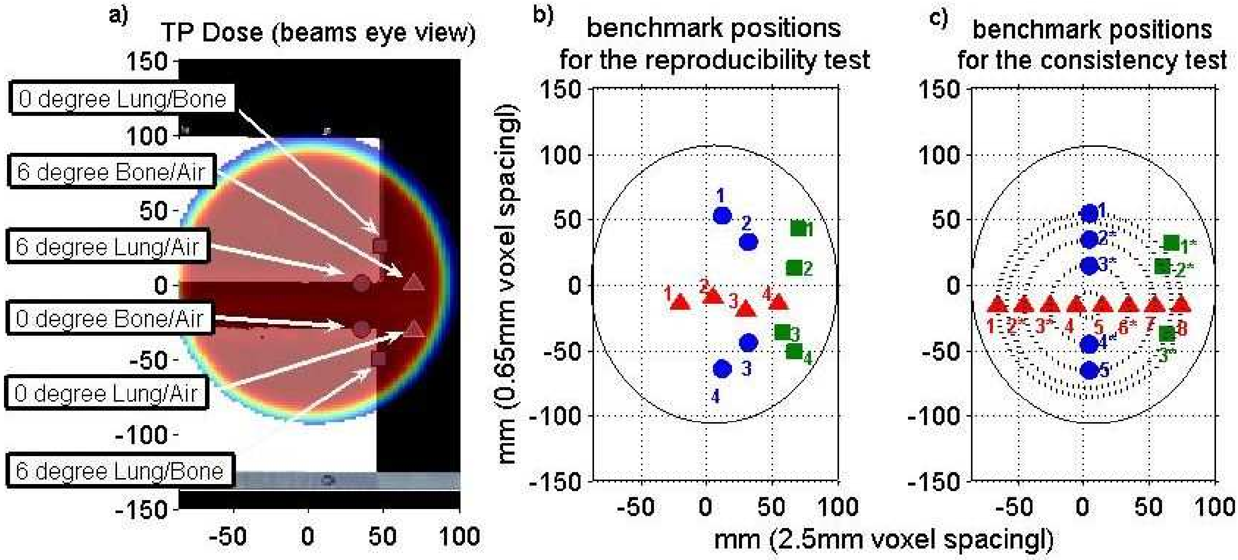

Fig. 4.2: Benchmark positions to test a) the sensitivity b) the reproducibility and c) the consistency of the measured PET signal (red: position in PMMA-air-PMMA, blue: positions in PMMA-bone-PMMA, green: positions in PMMA-lung-PMMA, profiles of positions marked with $*$ are shown in Figure 4.4).

4.2.4 *Testing of the consistency of the measured PET signal*

To test the consistency of the PET signal, we analyzed 16 depth profiles from the first data acquisition. The benchmark positions with respect to the beam position can be seen in Figure 4.2c. To test the PET scanner response dependence on the position within the scan field, we selected pairs of benchmark positions with the same distances to the scanning field origin for each material arrangement (PMMA-air-PMMA: 1|8, 2|7, 3|6, 4|5, PMMA-bone-PMMA: 2|5, 3|4, PMMA-lung-PMMA: 2|3).

In addition to the consistency of the PET signal relative to the position within the scanning field ('global noise'), the consistency with respect to 'local noise' was tested. The comparison of the depth profiles for each material arrangement was done using three different average areas perpendicular to the profile direction along the x- and y-axis: a) 1 voxel in x direction (2.5 mm) / 1 voxel in y direction (0.65 mm), b) 1 voxel in x direction (2.5 mm) / 4 voxels in y direction (2.6 mm) and c) 2 voxels in x direction (5 mm) / 7 voxels in y direction (4.55 mm). For all benchmark positions the measured ranges were compared to the simulated ranges to correct for beam divergence effects. The variations in the differences between measured and simulated ranges reflected the consistency of the PET/CT range verification method.

4.2.5 Sensitivity of the measured PET signal to anatomical changes

Inhomogeneities and tissue interfaces markedly affect the dose distribution of charged particles. While the smooth distal dose fall-off translates in a smooth distal activity fall-off in a homogeneous material, the distal activity fall-off produced by a diluted dose distribution is not smooth anymore. The relation between the dose distribution and the corresponding activity distribution is not straightforward and therefore the ability to accurately monitor the delivered range behind complex material inhomogeneities cannot simply be devolved from the situation in a homogeneous phantom. Dose profiles downstream of air/bone, air/lung and bone/lung interfaces showed that sharp tissue interfaces (0°) result in a degradation of the residual range. For more shallow tissue interfaces (6°) the range degradation smoothed out [Uri86].

To test the sensitivity to detect those range changes, MC calculated activity depth profiles and measured activity depth profiles through material interfaces, once parallel (0°) and once angled (6°) to the beam direction were compared. Interfaces between air-lung, air-bone and lung-bone were considered. The benchmark positions with respect to the beam position for this study can be seen in Figure 4.2a.

4.3 Results

4.3.1 Reproducibility of the measured PET signal

Figure 4.3 shows an exemplary comparison of activity depth profiles obtained at two data acquisitions, and for the benchmark positions shown in Figure 4.2b. The data was corrected for differences in the absolute activity values due to the different irradiation/acquisition times (as shown in Table 4.2). The difference in range between the two measurements was estimated using the three methods A, B and C, as described in section 3.4.2. The results of the three methods are given in Table 4.3.

Method	**Position 1**	**Position 2**	**Position 3**	**Position 4**
	PMMA-air-PMMA			
A (meas1-meas2)	0.55	0.11	-0.26	1.46
B (meas1-meas2)	0.16	-0.51	0.28	0.64
C (meas1-▷meas2)	0	0	0	-1.30
	PMMA-lung-PMMA			
A (meas1-meas2)	-2.57	-0.77	-1.34	-2.10
B (meas1-meas2)	-1.96	-1.17	-0.18	-1.60
C (meas1-▷meas2)	1.94	1.30	0.65	1.94
	PMMA-bone-PMMA			
A (meas1-meas2)	-0.45	1.67	1.41	0.48
B (meas1-meas2)	-0.91	-0.90	-1.29	-0.29
C (meas1-▷meas2)	0.65	-0.65	0	0

Tab. 4.3: Range differences in mm between 2 data acquisitions. Differences were calculated for three material arrangements (air, lung or bone slab enclosed in PMMA slabs), four benchmark positions (Position 1-4), and using three methods (A-C).

For all benchmark positions, we see that the differences between the two measurements at 20% and at 50% of the last activity maximum are similar. Fore some positions the differences at 20% and 50% have the same sign, which implies that the fall-off regions of the depth profiles are shifted against each other. for other positions the differences at 20% and 50% have different signs, which implies that the fall-off regions of the depth profiles have different gradients. This is confirmed by the shift method, which calculates the best agreement of

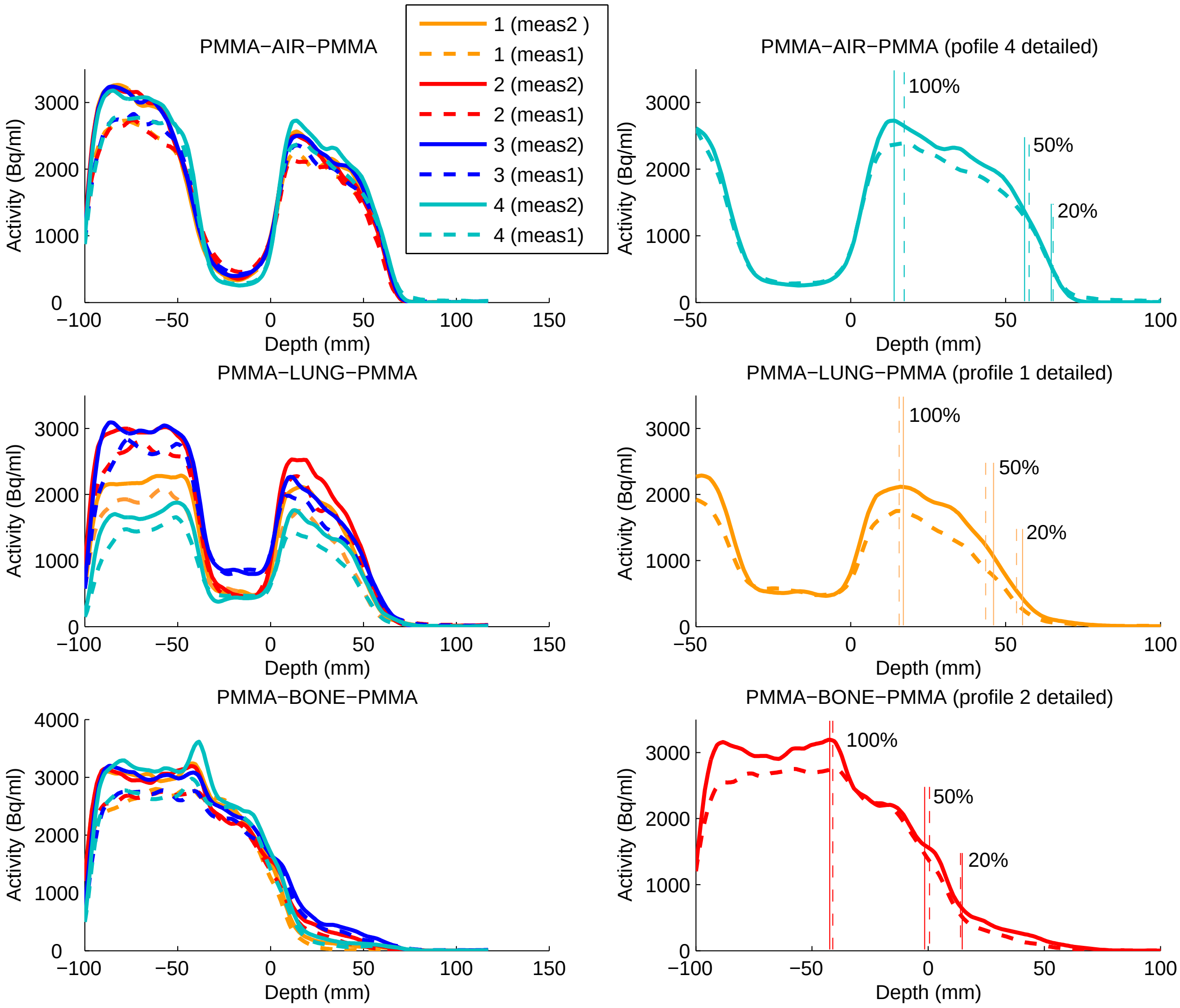

Fig. 4.3: Left: Activation depth profiles for two data acquisitions (solid and dashed line) at 4 positions through a PMMA-air/lung/bone-PMMA layer. Right: Illustration of the analysis of the range differences for each layer.

depth profiles with differently signed 20% and 50% range differences for a zero shift.

The average difference between the two measurements at 50% (20%) is 1.1±0.2 mm (0.8±0.2 mm). Except for two benchmark positions in PMMA-lung-PMMA (1 and 4), which are close to the beam edge, all range differences between the two measurements are smaller than 1.7 mm. On averadge method C calculates the best agreement between the depth profiles for shifts of about 0.7±0.2 mm. In conclusion, we found that the reproducibility of the measured PET range is of the order of 1 mm in standard deviation.

4.3.2 Consistency of the measured PET signal

In order to evaluate the consistency of the PET signal, we compared activity depth profiles within identical material arrangements, but at different positions within the irradiation field. For each position, we used three different areas a), b) and c) over which the signal was averaged. Examples of the measured depth profiles, and the deduced beam ranges thereafter, are shown in Figure 4.4 for three benchmark positions per layer (marked with $*$ in Figure 4.2c). These positions were selected so that two of them would be at the same distance from the scanning field center, while the third would be at a larger distance. Figure 4.4 illustrates the measured range dependence on two factors: radial distance ('global noise') and average area ('local noise'). On the right, extracted ranges at 20% (method A) and 50% (method B) of the last fall-off for each depth profile position and each average area are shown.

The depth profiles for each material arrangement show variations in their absolute values, but are very similar in the fall-off region. For the case of the PMMA-air-PMMA layer, the ranges for all three benchmark positions agree within 1.7 mm for method A, and within 0.9 mm for method B. The ranges of the two benchmark positions at the same distance to the origin show a slightly enhanced similarity as opposed to non-equidistant benchmark positions. This could be an indication for a weak dependence of the measured PET signal on the radial position within the scanning field.

In the case of the PMMA-bone-PMMA layer, the ranges show larger variations than in the previous geometry. For method A as well as for method B, the ranges for all three benchmark positions agree within 2.5 mm. Here only for method B a slightly enhanced agreement in the ranges of equidistant benchmark positions is noticeable.

When the beam traverses the PMMA-lung-PMMA layer, the ranges demonstrate even larger variations than those seen for the other geometries. For method A, the ranges for all three benchmark positions agree within 1.8 mm, whereas they vary by 3.8 mm for method B. Here no enhanced similarity of ranges at benchmark positions located at the same distance

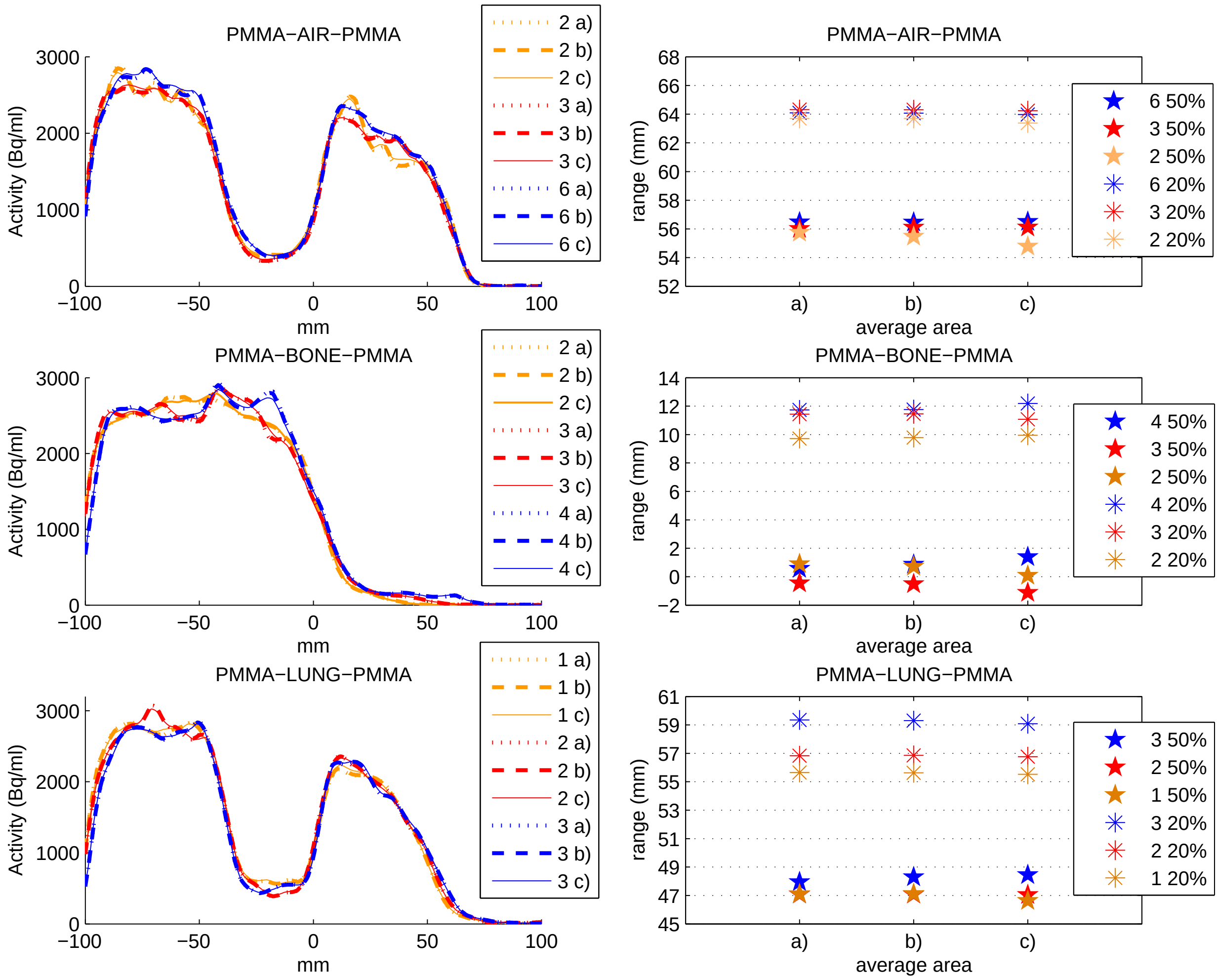

Fig. 4.4: Left: Activation depth profiles at 3 different positions (numbers in the legend refer to positions in Figure 4.2c)) through PMMA-air/bone/lung-PMMA (the red and blue curves correspond to benchmark positions that have the same distance to the scanning field origin, while the yellow curve refers to a position at a larger distance). The signal was averaged over three different areas (dotted a)/dashed b)/solid c)). Right: Ranges at the 20%(dashed stars) and the 50%(filled stars) fall-off position for the three measurement positions and the three different averaging areas.

from the scanning field origin was observed.

Table 4.4 summarizes the results for all benchmark positions shown in Figure 4.2c). By analyzing depth profiles averaged over different areas perpendicular to the profile direction we observed that the measured PET range is relatively insensitive to 'local noise' (<1 mm difference in range). Only a weak correlation of the measured range to the radial position in the scanning field was observed.

The standard deviation of the 20% range (method A) averaged over all benchmark positions is about 1 mm, 1.3 mm and 1.5 mm for the PMMA-air-PMMA, PMMA-bone-PMMA and PMMA-lung-PMMA layers, respectively. The corresponding numbers for the 50% range (method B) are 1.1 mm, 1.1 mm and 0.6 mm, respectively. The largest deviations from the mean range (up to 2.5 mm) occur mainly for benchmark positions at the beam edge and therefore also at the edge of the FOV of the PET scanner, see Figure 4.5. In addition to the position of these depth profiles also beam divergence effects could explain these large variations.

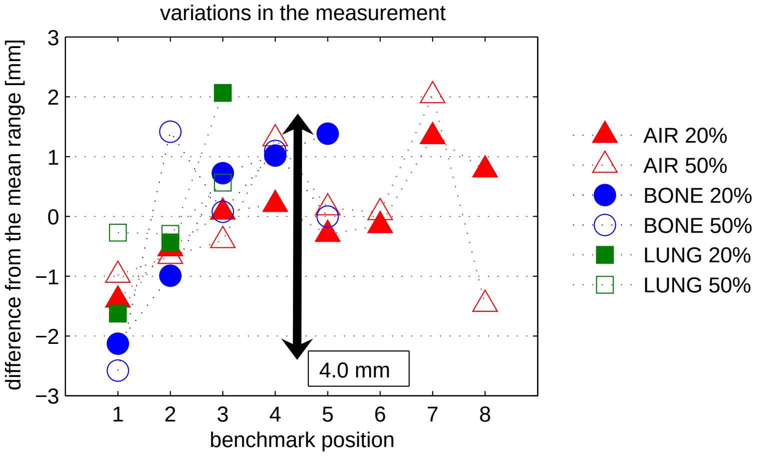

Fig. 4.5: Variations of the measured ranges in each material arrangement for average area a).

Consistency of PET signal as derived from measurement and MC simulations

In the clinical application of PET range verification measured activation profiles are compared with MC simulated activation profiles. Thus not the variations of the measured ranges but the variation in the differences between measured and simulated ranges are a norm for the consistency of the PET/CT range verification method. Also variations of the measured

	50% range (method A) [mm]			**20% range (method B) [mm]**		
Position	a)	b)	c)	a)	b)	c)
			PMMA-air-PMMA			
1	55.42	54.57*	46.18*	62.85	62.8	61.46
2	55.74	55.47	54.78	63.7	63.7	63.38
3	56.01	56.1	56.11	64.32	64.31	64.24
4	57.71	57.64	57.65	64.45	64.44	64.49
5	56.55	56.41	56.74	63.94	63.91	64.01
6	56.47	56.46	56.51	64.09	64.07	63.97
7	58.43	58.42	58.22	65.57	65.55	65.34
8	54.94	55.14	56.4	65.02	65.06	65.11
Mean ± SD	*56.4±1.1*	*56.5±1.1*	*56.7±1.0*	*64.2±0.8*	*64.2±0.8*	*64.0±1.1*
			PMMA-lung-PMMA			
1	-3.1	-3.01	-2.6	8.58	8.59	8.69
2	0.89	0.72	0.08	9.72	9.79	9.95
3	-0.45	-0.51	-1.12	11.43	11.46	11.08
4	0.57	0.85	1.39	11.73	11.76	12.18
5	-0.53	-0.51	-0.66	12.1	12.03	11.61
Mean ± SD	*-0.5±1.2*	*-0.5±1.1*	*-0.6±1.0*	*10.6±1.4*	*10.7±1.3*	*10.7±1.3*
			PMMA-bone-PMMA			
1	47.1	47.12	46.63	55.65	55.63	55.53
2	47.07	47.08	47.05	56.84	56.86	56.76
3	47.93	48.3	48.39	59.34	59.3	59.06
Mean ± SD	*47.4±0.4*	*47.5±0.6*	*47.4±0.8*	*57.3±1.5*	*57.3±1.5*	*57.1±1.5*

Tab. 4.4: 20% and 50% fall-off ranges at all benchmark positions in Figure 4.2c) for three different averaging areas a), b) and c). The average range (and one standard deviation) over all positions in a layer is also given. (Data denoted by an asterisk were excluded from the analysis due to the depth profile position close to the irradiation field margin.)

ranges due to divergence effects should be corrected by subtracting the corresponding MC simulated PET ranges. However, variations due to benchmark positions close to the FOV in the PET scanner will remain.

Figure 4.6 shows the variations of the differences between measured and simulated PET range, normalized to the mean difference for method A and B (left) and method C (right).

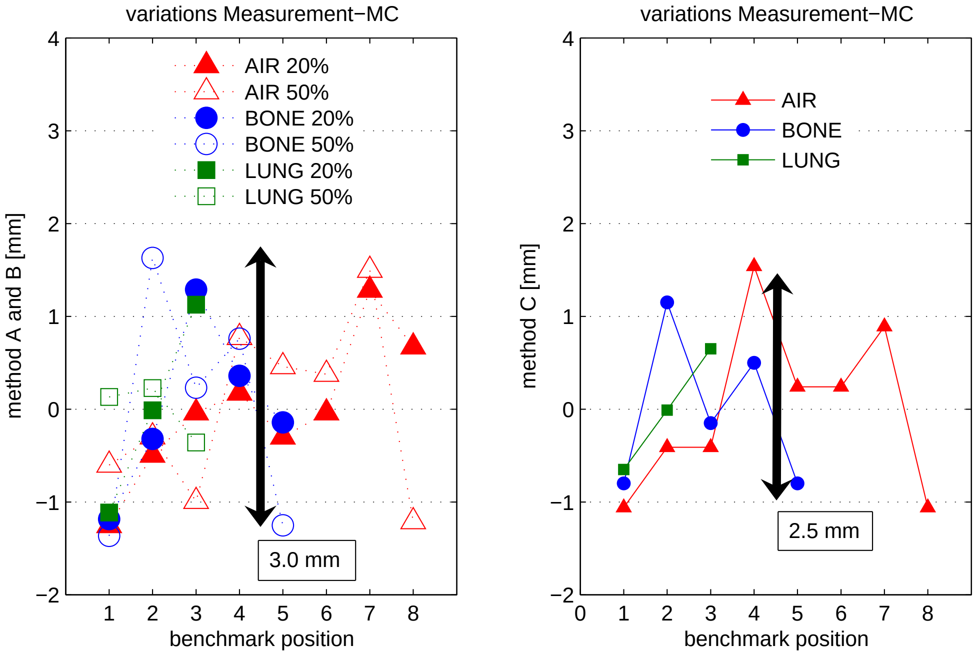

Fig. 4.6: Left: Differences at the 20% and 50% fall off position between measured and simulated PET range normalized to the mean difference for the 16 benchmark positions shown in Figure 4.2c). Right: Normalized difference between measured and simulated PET range analyzed with the shift method.

Table 4.5 shows the standard deviation of the differences between simulated and measured range for all three methods. The shift analysis gives standard deviations of 0.9 mm, 0.6 mm and 0.5 mm for PMMA-air-PMMA, PMMA-bone-PMMA and PMMA-lung-PMMA, respectively.

We conclude that the consistency of the PET/CT range verification method is of the order of 1 mm in standard deviation, i.e. of the same order as the reproducibility of the range measurement.

Standard deviation of the differences between MC and Measurement [mm]		
50% range (method A)	20% range (method B)	Shift (method C)
PMMA-air-PMMA		
0.9	0.7	0.9
PMMA-lung-PMMA		
1.2	0.6	0.6
PMMA-bone-PMMA		
0.3	0.7	0.5

Tab. 4.5: Standard deviations of the differences between simulated and measured ranges at all benchmark positions in Figure 4.2c) and for all range verification methods (A-C).

4.3.3 Sensitivity of the measured PET signal to tissue inhomogeneities

We compared measured and MC simulated activity depth profiles through tissue interfaces with different angles to the beam direction (blue: 6°, red: 0°). The irradiated geometries are shown schematically in Figure 4.7.

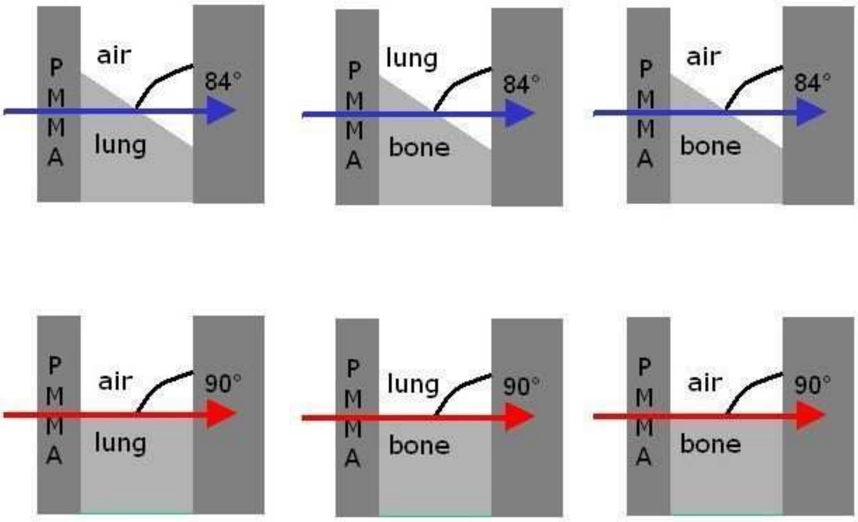

Fig. 4.7: Tissue interfaces placed at 6° (blue) or 0° (red) with respect to the beam direction.

We calculated the range difference for the two interface angles as

$$\Delta R_{meas} = R_{meas}(0°) - R_{meas}(6°) \tag{4.1}$$

$$\Delta R_{MC} = R_{MC}(0°) - R_{MC}(6°) \tag{4.2}$$

for the measured and simulated depth profiles, respectively, where R(0° and R(6° are the ranges for the 0° and 6° interfaces, as shown in Figure 4.7. The range calculation was done using methods A, B and C, as described above. Figure 4.8 shows the measured (left) and simulated (right) activity depth profiles. Table 4.6 summarizes the measured and MC predicted range differences at the 20% and 50% fall-off position and as calculated by the shift method.

	20% range (method A)	50% range (method B)	shift (method C)
	lung/air interface		
ΔR_{meas}[mm]	0.47	0.22	0.65
ΔR_{MC}[mm]	-1.20	-1.31	-1.30
$\Delta R_{meas} - \Delta R_{MC}$[mm]	1.67	1.53	1.95
	bone/air interface		
ΔR_{meas}[mm]	-2.82	-3.48	-3.24
ΔR_{MC}[mm]	-7.94	-2.64	-2.59
$\Delta R_{meas} - \Delta R_{MC}$[mm]	5.12	0.84	0.65
	bone/lung interface		
ΔR_{meas}[mm]	-5.74	-0.03	-3.89
ΔR_{MC}[mm]	-6.56	-0.92	-2.59
$\Delta R_{meas} - \Delta R_{MC}$[mm]	0.82	0.89	1.30

Tab. 4.6: Measured and simulated range differences for depth profiles through tissue interfaces placed at 6° or 0° with respect to the beam direction. In addition the differences of the measured and simulated differences are given.

Since air and lung tissue exhibit relatively small density differences, we did not expect to observe a significant range difference for a beam traveling though a 6° or a 0° air/lung

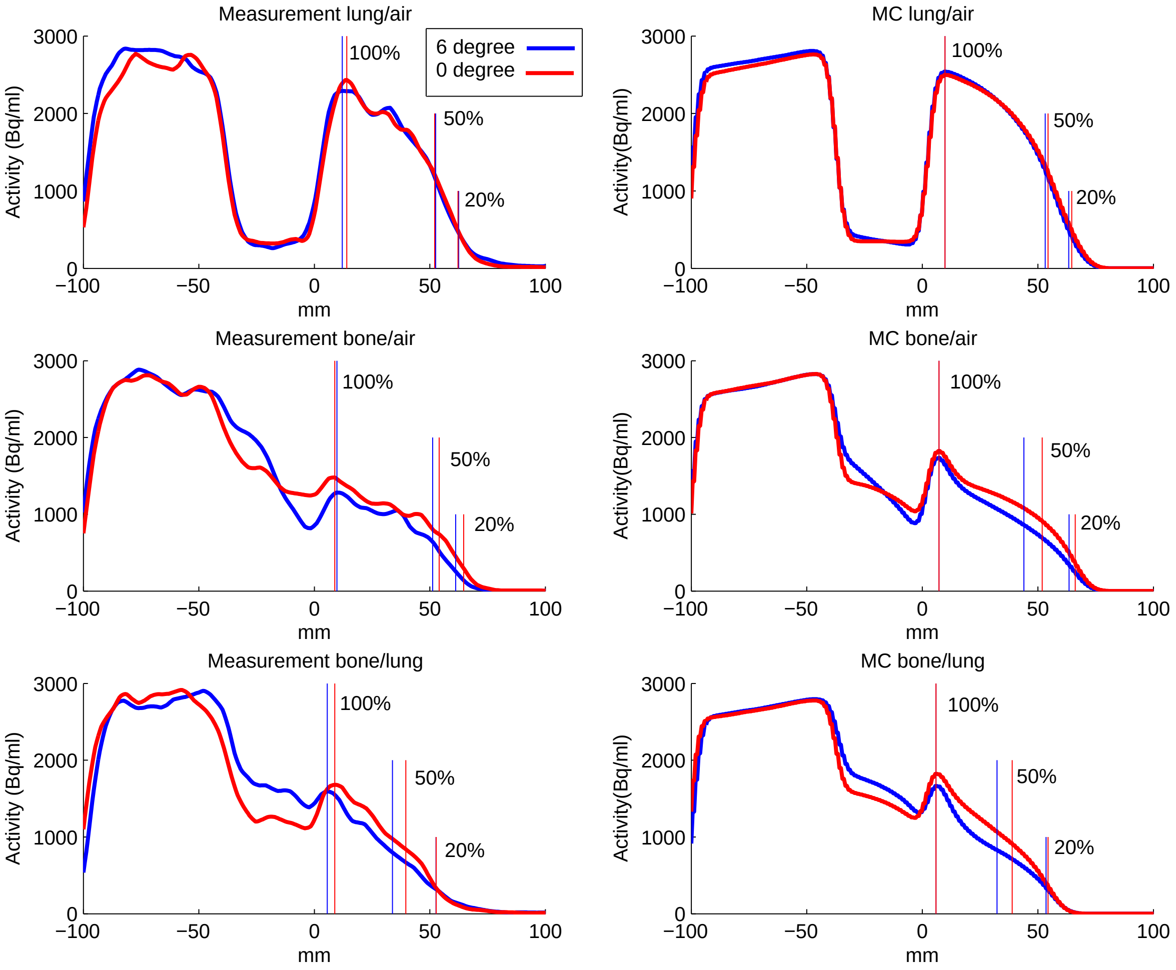

Fig. 4.8: Measured (left) and simulated (right) activity depth profiles through tissue interfaces placed at 6° (blue) or 0° (red) with respect to the beam direction. The interfaces are lung/air (top), bone/air (middle) and bone/lung (bottom).

interface. The measured and simulated range differences are up to 1.3 mm (Table 4.6) and agree within 1.7 mm for the 50% fall-off position (method A), within 1.5 mm for the 20% fall of position (method B) and within 2 mm for the shift analysis (method C).

We found significantly larger range differences (up to 7.9 mm) for the bone/air interface. This is due to the density difference of air and bone tissue. Measurement and simulation agree within 5.1 mm at the 50% fall-off position, within 0.8 mm at the 20% fall-off position and within 0.7 mm for the shift analysis.

The results for the bone/lung interface are similar to the bone/air results. This is due to the relative small differences in density between air and lung compared to bone. Measurement and MC prediction agree within 0.8 mm for method A, within 0.9 mm for method B and within 1.3 mm for method C.

For all three tissue interfaces, the agreement between measured and MC predicted range differences from the shift analysis is within 2 mm. MC simulated dose distributions are considered as the most precise calculation of the delivered dose [And91] and hence the most precise prediction of the resulting PET activation compared to for example the filtering approach described in [Par06]. However, in this phantom study comparisons of MC simulated depth profiles through different angled interfaces are especially sensitive to the PVE. As mentioned above, the PEV is less pronounced in patient calculations and thus the already very satisfying agreement between measured and MC predicted range differences in our phantom study is a demonstration of the high sensitivity of the PET/CT range verification method. This phantom study indicates the feasibility of PET/CT treatment verification to detect small range variations in the presence of complex tissue inhomogeneities.

4.4 Discussion

This phantom study concentrates on the physical potential of PET/CT range verification for proton treatments. The standard deviation of 1.0 mm of range differences between two independent measurements and the standard deviation of 1.0 mm of range variations within one measurement show the good reproducibility and the consistency of the measured PET activation signal. However, range differences up to 2.6 mm between two measurements, as well as global range variations up to 2.6 mm within one measurement can occur in a phantom measurement. Those large deviations only occur at the beam edge or at positions on the edges of the FOV in the PET scanner and therefore should be of minor importance in a typical patient case. Range verification in the center of a typical patient field that usually does not exceed a diameter of 10 cm and is well positioned in the center of the FOV of the scanner, should have a physical accuracy of 1 mm.

Results of the low-statistics analysis were found to be in the same order of magnitude as the presented results for the reproducibility, the consistency and the sensitivity. Typical dose per day for a patient treatment are 1-3 Gy(RBE). Results concerning the physical potential of the method achieved in this phantom study are applicable for the patient routine performed at our facility and the more in clinical practice at facilities where reduced delay times between treatment and PET/CT scan are feasible.

This phantom study indicates the physical potential for millimeter accuracy in PET range verification of the dose delivered in proton irradiation by commercially available PET/CT scanners like the Biograph 64 PET/CT scanner.

5. CLINICAL POTENTIAL OF PET TREATMENT VERIFICATION

5.1 Introduction

The clinical pilot study [Par07b] investigated the feasibility of PET/CT treatment verification in a small population of 9 patients for tumor sites including head-and-neck (4), paraspinal (3), orbit (1) and eye (1). It was shown that the beam range could be verified within an accuracy of 1-2 mm in low perfused bony structures of head and neck patients for which an accurate co-registration of predominate bony anatomy (skull) was possible. At other positions and for other tumor sites, however, millimeter-accurate range verification failed. The most likely reason was attributed to limitations due to washout and rigid co-registration as well as motion uncertainties in the prolonged scan time of 30 min.

To employ PET/CT range verification clinically, it is crucial to know whether disagreements between measured and calculated activity reflect errors in the treatment planning / delivery or whether they are caused by inherent limitations of the method. Therefore, the present study emphasizes the qualitative and quantitative specification of inherent challenges of offline PET/CT imaging for a larger population of patients and tumor sites. The aim is to identify possible technological and methodological improvements, to allow for a wider applicability of PET/CT range verification. A systematic data analysis was performed on a large set of patients having a variety of tumor locations including head, spine and abdomino pelvic. The following aspects are addressed:

- Restrictions on the accuracy of the offline PET/CT range verification method due to biological washout processes: Range verification ability is compared at positions where the proton beam ranged out in bone and at positions where the beam ranged out in well-perfused tissue.

- Effects on the accuracy of the offline PET/CT verification method due to patient motion: Lateral agreement between measured and simulated activity distributions for tumors in the thorax and abdomen are compared to the lateral conformity in head and neck tumor cases.

- Uncertainties in the MC-simulated activity distributions due to the restricted correlation in the mapping of HU to elemental compositions and washout characteristics: HU domains for different organs in the abdomen and pelvis are determined to investigate whether the HU mapping is sufficiently correlative to assign organ specific elemental compositions and washout characteristics in the MC simulations. To test the influence of uncertainties, MC simulations for different HU mappings are performed and compared.

- PET/CT range verification ability with respect to the tumor location: Patients were grouped and average absolute range deviations for different tumor locations were calculated. Site-specific challenges in addition to the three factors listed above are evaluated and an importance factor, indicating the degree of limitation on the PET/CT range verification method at this tumor location, is introduced for each aspect.

5.2 Methods

For 23 patients (9 patient data sets were acquired before [Par07b], 14 within the framework of this work) with tumors in the cranial base, spine, sacrum, prostrate and orbit an offline PET/CT scan after proton radiotherapy was performed at MGH. Table 3.1 gives detailed information on the tumor site, the dose per field, the delay between irradiation and imaging and the number of fields delivered in each patient at the day of the PET/CT scan. Table 5.1 gives an overview of the patient subgroups used for data analysis in the following sections. The clinical protocol used is described in section 3.3.1.

Validation of the delivered treatment was achieved by comparing the measured activity distribution with corresponding MC-simulated distributions, that were based on the treatment plan, the planning CT data and the time course of irradiation and imaging, as described in section 3.2.1. Data analysis was performed with methods described in section 3.4.

# patient	**1**	**2**	**3**	**4**	**5**	**6**	**7**	**8**	**9**	**10**	**11**	**12**	**13**	**14**	**15**	**16**	**17**	**18**	**19**	**20**	**21**	**22**	**$22^{\S}$**	**23**	**$23^{\S}$**	**total**
clinical pilot study [Par07b]	X	X	X	X	X	X	X	X	X																	**9**
5.3.1 First glance 2D			X	X						X	X	X	X	X	X	X		X	X	X	X	X				**14**
5.3.2 First glance 1D			X	X						X	X		X	X		X		X		X	X	X				**11**
5.4.1 Reproducibility																						X	X			**1**
5.4.2 Biological washout processes										X	X							X	X	X	X					**6**
5.4.3 Motion			X	X					X	X	X	X	X	X	X	X		X	X	X	X					**14**
5.4.4 Simulation uncertainties									X				X													**2**
5.4.5 Tumor site specific challenges							X					X		X	X	X		X								**6**
5.4.6 Particular beneficial tumor sites										X	X		X				X	X	X	X	X	X	X	X	X	**10**

Tab. 5.1: Overview about patient subgroups used for data analysis in the following sections (§: Repeated PET/CT data acquisition)

5.3 Results I: Qualitative analysis of the feasibility of offline in vivo PET/CT range verification

5.3.1 2D - Gamma index analysis

Comparison of 2D color-wash images of measured and MC-simulated activity distributions shows impressive qualitative similarity in most cases. However, a quantitative judgment of the agreement of the two distributions based on color-wash images is difficult. More precise information about the agreement in the absolute values of the distribution can be obtained from difference plots. Since the main interest of PET/CT imaging lies in a spatial verification of the delivered dose distribution, a gamma index analysis gives more valuable information. It allows to simultaneously evaluate the absolute and the spatial agreement of the MC-simulated and measured activity distributions.

To perform a meaningful gamma index analysis reasonable absolute values and spatial pass-fail criteria have to be established. Histograms for the coronal, transversal and sagittal slice through the isocenter were calculated for 14 patients. In these histograms the absolute difference in activation at each position as well as the distance to the nearest point with the same activation (Figure 5.1) were evaluated.

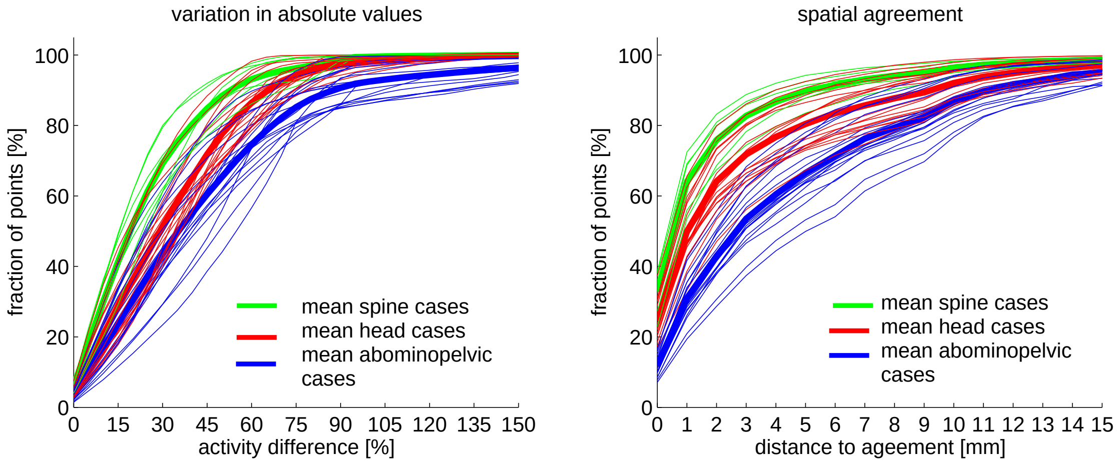

Fig. 5.1: Evaluation of variations in the absolute values (left) and spatial agreement (right) in the coronal, transversal and sagittal cut through the isocenter for 14 patients (2 spine (thin green), 6 head (thin red) and 6 abdominal pelvic (thin blue) tumor sites. Thick lines give mean values for each of the three tumor site groups).

The left graph in Figure 5.1 illustrates that approximately 75% of the MC-simulated and measured activity distribution show less than 45% variation in their absolute value. Likewise, 75% of the distribution shows a 100% absolute agreement within 3 mm periphery (right graph of Figure 5.1). The average agreement of the MC-simulated and measured activity distribution is thus within 45% of the absolute values of activation and within 3 mm spatially. Hence 45% and 3 mm are reasonable cutoff values for a meaningful gamma index analysis of activity distributions.

The diversification into different tumor sites (head, spine, abdomino pelvic) in Figure 5.1 illustrates that the mean variation in the absolute values and the mean distances to agreement are different, for different tumor locations. In the following sections, challenges of offline PET/CT range verification will be analyzed with respect to different tumor locations. In section 5.4.5, site-specific weighting factors will be assigned to summarize which patient groups can benefit most from the approach.

Besides the dependency of the absolute and the distance to agreement on the tumor site, also the dependency on (i) the number of given treatment fields and (ii) the total dose on the day of imaging, (iii) the delay between irradiation and imaging and (iv) the imaging planes was evaluated. For the six head patients analyzed before, Figure 5.2 shows the evaluation of variations in the absolute values and the spatial agreement with respect to the possible dependencies.

Figure 5.2 indicates a marginal dependency of the absolute and spatial agreement on the number of given treatment fields as well as on the imaging plane. The agreement between measured and simulated activity distributions seems to be slightly improved for patients that received two treatment fields at the day of imaging. An improved agreement is also recognizable in transversal and frontal imaging planes. On the contrary, no dependency on the total dose on the day of imaging or the delay between irradiation and imaging is apparent. However, an analysis on a population of only six patients is not statistically sufficient to rule out such dependencies.

5.3.2 1D - analysis

To explore the range verification ability of PET/CT imaging, simulated and measured activity depth profiles at a number of positions in each patient and for each treatment field were evaluated with method A, B and C (as described in section 3.4.2). Profile positions were chosen through the isocenter as well as in a raster of 1.5 cm (and 2 cm, 3 cm, 4.5 cm and 6 cm depending on the field size) in the orthogonal planes through the isocenter as illustrated in Figure 5.3.

Figure 5.3 shows a percental occurrence of absolute range deviation between MC simulation and measurement. For an analysis at approximately 87 random positions mean

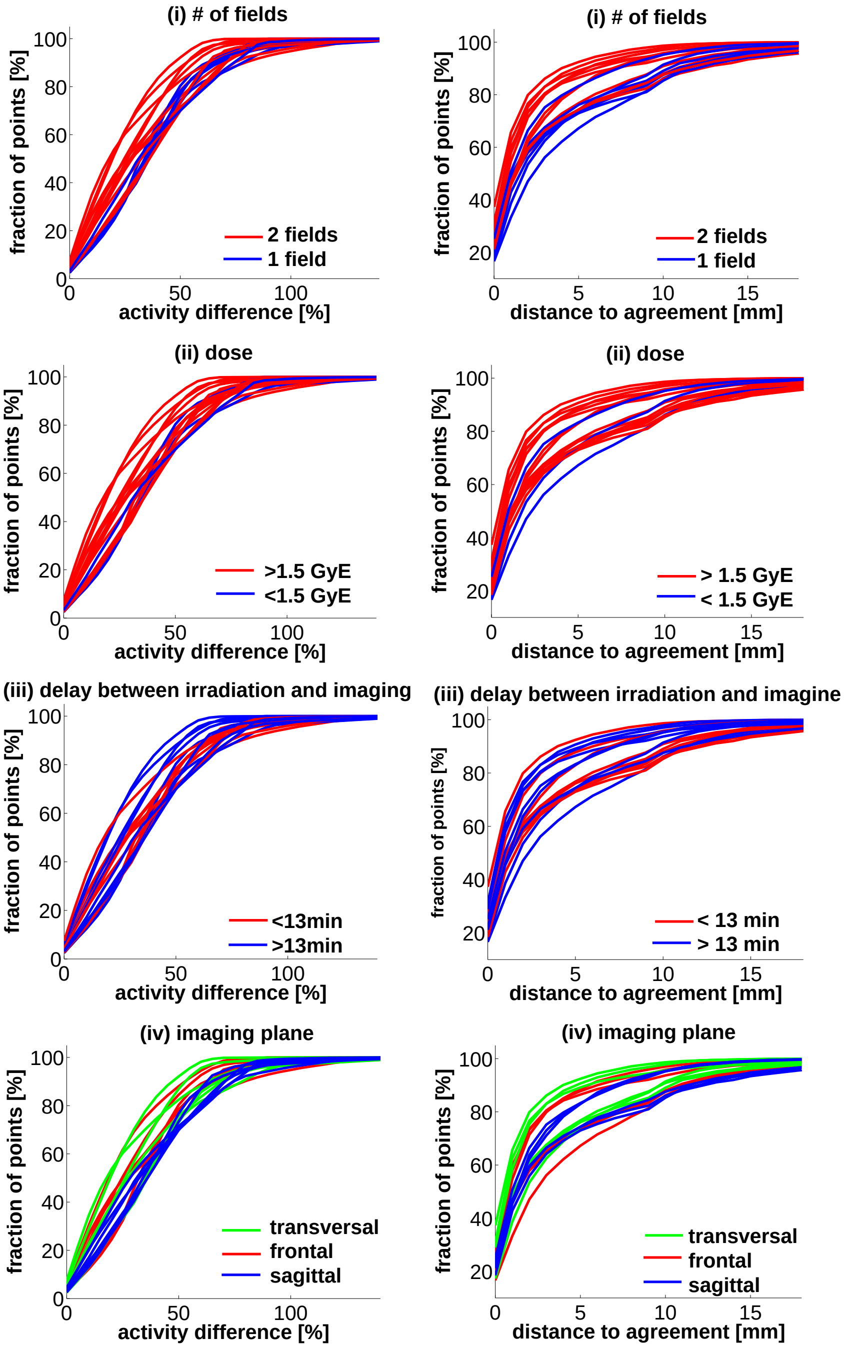

Fig. 5.2: Absolute (left) and spatial (right) agreement of measured and simulated activity distribution in patients with tumors in the head with respect to (i) the number of given treatment field and (ii) the total dose on the day of imaging, (iii) the delay between irradiation and imaging and (iv) the imaging planes.

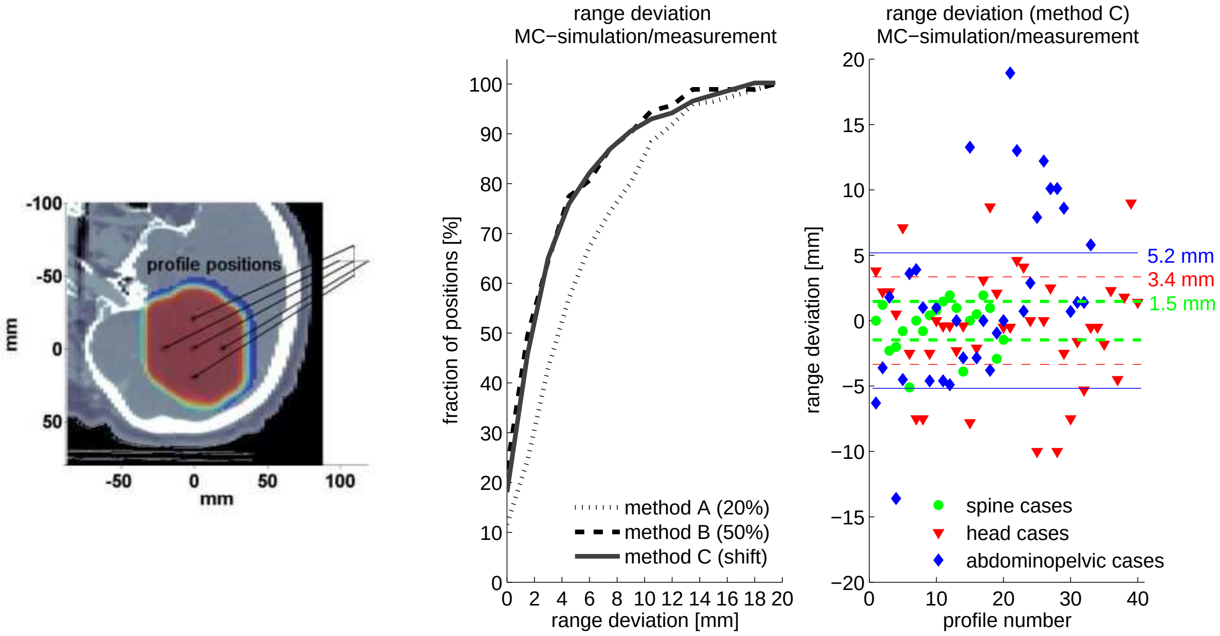

Fig. 5.3: Left: Illustration of the chosen profile positions grid in an exemplary head patient, Middle: %-occurrence of absolute range deviations between simulated and measured activity profiles in a population of 11 patients for method A, B and C. Right: Range deviations calculated by the shift method shown for different tumor locations (spine: 20, head: 40, abdominopelvic: 33 positions). Mean absolute deviation for spine, head and abdominopelvic patients are given in green, red and blue, respectively.

variations are 5.6 mm, 4.0 mm and 3.6 mm for method A, B and C, respectively. The worse outcome for method A is explainable by the influence of statistical noise and modeling uncertainties, as discussed in section 3.4.2.

Range deviations, separately calculated by the shift method for different tumor locations, show absolute mean values of 1.5 mm, 3.4 mm and 5.2 mm for tumors in the spine, head and abdomino pelvic region, respectively. As in the 2D analysis, this illustrates that the agreement between simulation and measurement is best for tumor locations in the spine, and worse for tumor locations in the abdomino pelvic. For the observed range deviations a systematic analysis of the underlying causes is presented in the next section. There, we try to distinguish, whether these range deviations reflect errors during the treatment planning/delivery or whether they were caused by inherent challenges of the method. After discussing each involved effect individually, we will summarize the results in section 5.4.5 and draw conclusions about the dependency of the agreement between the simulated and measured activity distribution on the tumor location.

5.4 Results II: Quantification of offline in vivo PET/CT range verification ability under different perspectives

5.4.1 Reproducibility

Before going into a systematic analysis of different challenging factors of the method, its technical limitations are evaluated. Phantom studies, as well as the first clinical pilot study [Par07a, Par07b], have demonstrated the feasibility of post-radiation PET/CT for in vivo treatment verification. In the previous section 4.3.1 PET images from two independent measurements were compared. The reproducibility of the measured PET range in a phantom geometry was found to be within 1 mm standard deviation. However, in vivo patient PET measurements are additionally challenged by blood perfusion, variations in the tissue composition, motion, and co-registration uncertainties.

To reveal technical limitations, such as the reproducibility for in vivo measurements, activity distributions from two independent data acquisitions of the same treatment fraction given at two different days, separated by one week, were compared in one patient (#22). Images of the first repeated patient scan done so far are shown in Figure 5.4. The patient received one right-anterior treatment field of 2.5 Gy(RBE) to a tumor location in the C-spine at both days of PET/CT imaging. The comparison of the upper and lower row in Figure 5.4 demonstrates the excellent reproducibility of the characteristics in the measured PET distribution.

The differences in the absolute values of the two PET measurements are up to 30%. These differences are not due to differences in the time course of the two measurements. MC simulations show that the effect of different time courses at most 3%. The differences seen in the measured activity distributions rather reflect statistical errors, variations in the elemental composition and the biological washout processes at different treatment days.

Range deviations between the two PET/CT scans were evaluated at 18 positions selected

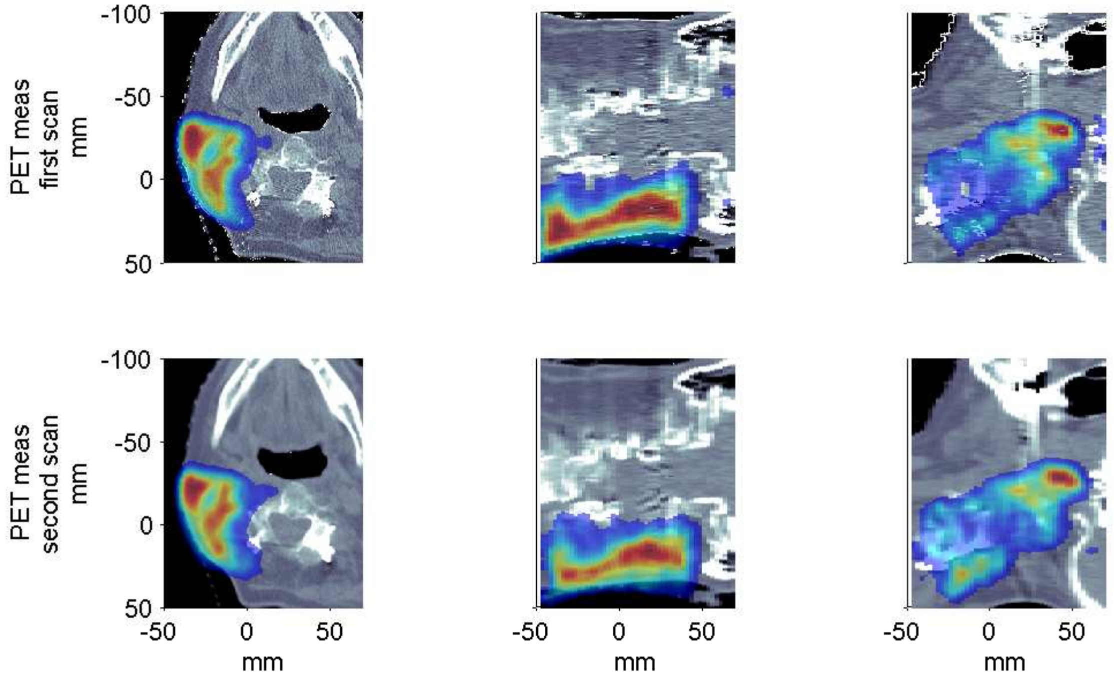

Fig. 5.4: Transversal, coronal and sagittal slice through the isocenter of the measured activity distribution. The first row shows images from the first scan. In the second row corresponding images from the second data acquisition can be seen.

within the treatment field as illustrated in the left of Figure 5.5. The middle graph in Figure 5.5 shows that at 95% of the positions the activity ranges agree within 3 mm for metod C. According to the right graph in Figure 5.5 the reproducibility of in vivo measured PET ranges is of the order of 1 mm in standard deviation. Since a single repetition of the irradiation and PET scan in only one patient cannot statistically ascertain the reproducibility, a study about repeated PET/CT scans in a larger patient population is under way. However, these data confirm the technical feasibility of in vivo range verification with commercially available PET/CT scanners for proton irradiation therapy.

5.4.2 Biological washout processes

For 6 patients ranges were verified at positions where the proton beam ended in bone (case i) as well as at positions where the beam stopped in well-perfused tissue to investigate the influence of the biological washout on the accuracy of the method. For well-perfused tissue

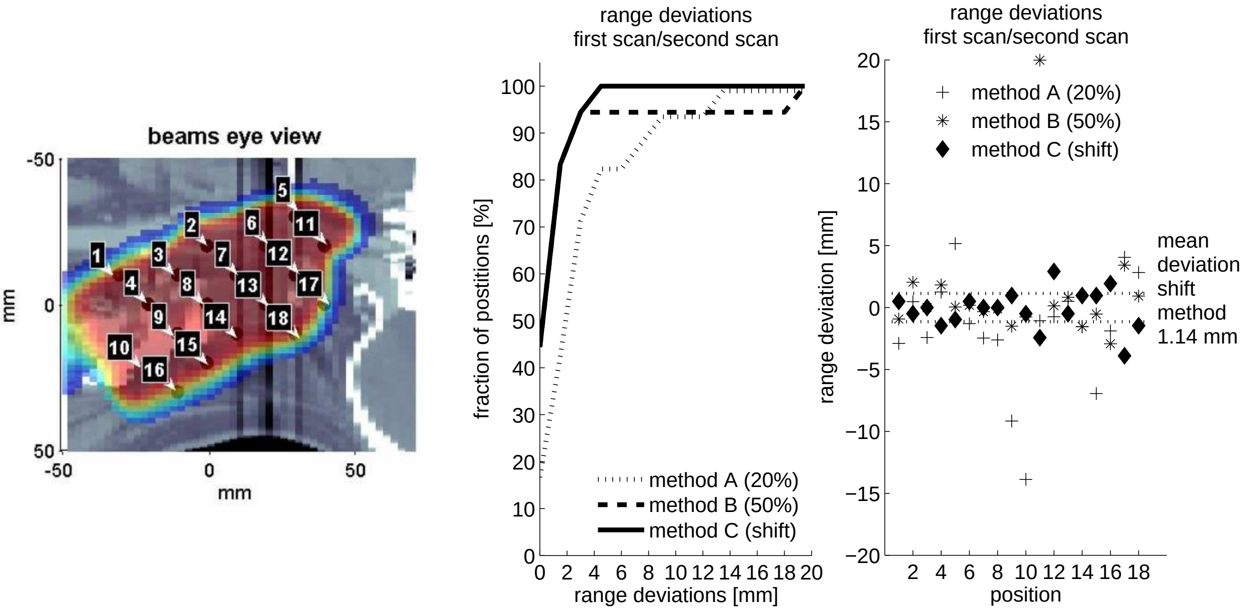

Fig. 5.5: Left: Profile positions. Middle: %-occurrence of absolute range deviations between two PET/CT scans. Right: Range deviations at each position. The mean absolute range deviation evaluated with the shift method was 1.14 mm.

it was distinguished whether the last maximum of the activity distribution was located in bone (case ii) or in soft tissue (case iii). Examples for all three cases are shown in Figure 5.6. The analysis was exclusively done for patients with tumors in the head and neck region that enable a very good immobilization during the 30 min of PET scan. Head and Neck tumor locations also provide a relatively rigid target geometry. Hence the influence of limiting factors such as patient motion (discussed in section 5.4.3) and image co-registration (discussed in section 5.4.5) were minimized.

Absolute mean deviation between measured and simulated activity range for all three cases (i, ii and iii) at the 50% (20%) position in the last fall-off region (method A (B)) as well as evaluated by the shift method (method C) are given in Table 5.2. For case (i) all three methods show a mean agreement of ranges within 2.5 mm. For case (ii) the shift method calculates a mean agreement within 2.2 mm, while a pointwise mm-accurate range verification seems to fail. For case (iii) all methods of analysis give relatively large absolute mean deviation between MC-simulated and measured activity ranges. This confirms that offline PET/CT scans permit mm-accurate range verification only at limited positions within the

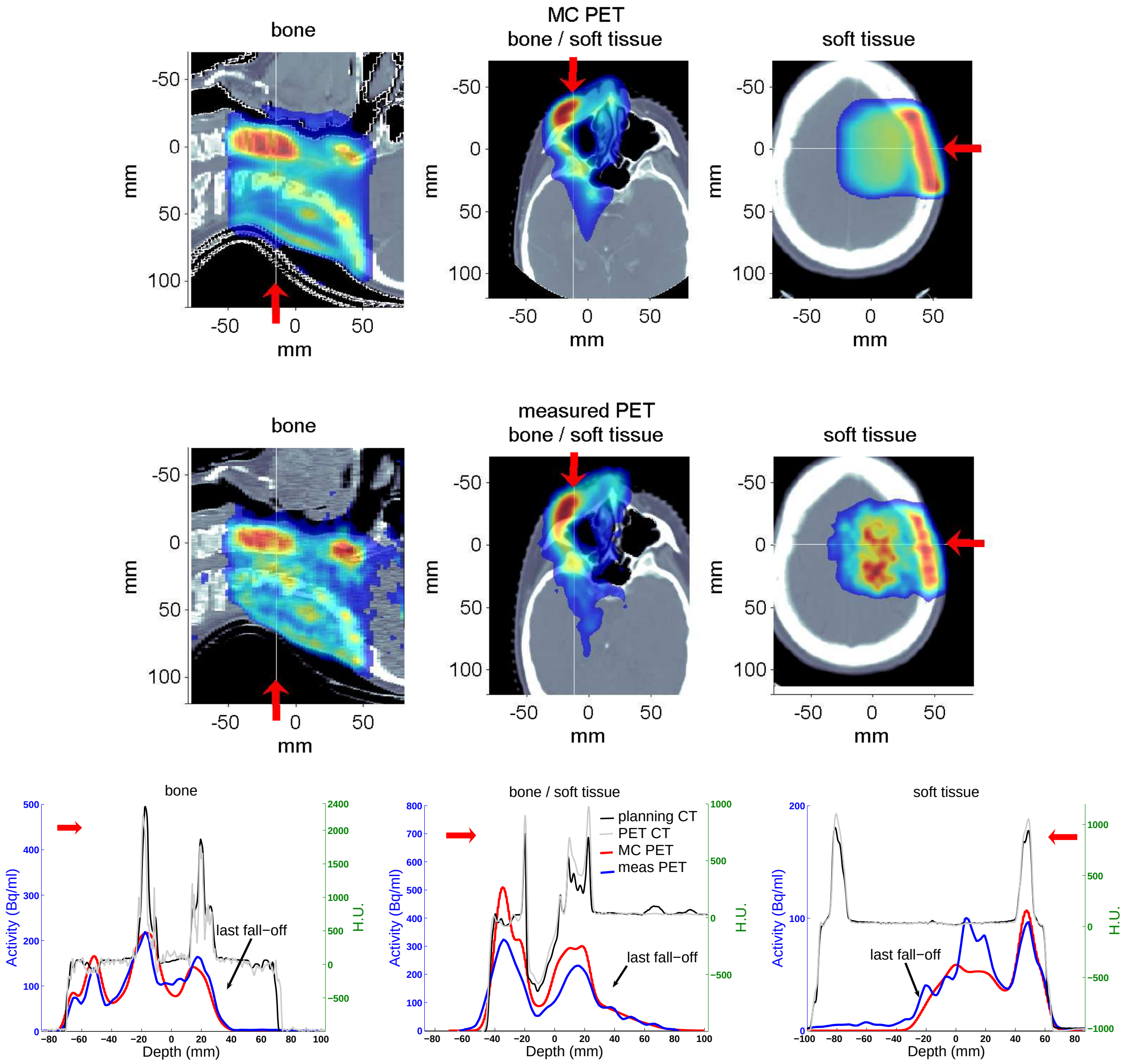

Fig. 5.6: Simulated (first row) and measured (second row) PET distributions demonstrating the following three cases: i) The distal activity fall-off is placed in bone (first column), ii) The distal activity fall-off is placed in soft tissue with the last maximum in bone (second column) and iii) The distal activity fall-off as well as the last maximum are placed in soft tissue (third column). The third row shows profiles at positions marked by white the lines above. The red arrows denote the beam direction.

treatment field, mainly in well-coregistered bony structures [Par07b].

	number of profiles	**Mean agreement between measured and simulated range [mm]**		
		pointwise verification		shift verification
		50%	20%	
bone **(i)**	25	2.5	1.2	2.4
bone/soft tissue **(ii)**	25	3.2	8.1	2.2
soft tissue **(iii)**	30	6.8	3.9	4.3

Tab. 5.2: Mean agreement between simulated and measured activity range for case i-iii. The range verification was done point wise at the 50% and 20% position in the last fall-off region as well as with the shift method.

Despite the good mean agreement between measured and simulated activity distribution in bone (case (i)), discrepancies up to 6.6 mm (3.6 mm) can occur at the 50% (20%) fall-off position. For some positions in bone the shift method even showed deviations larger than 5 mm. However, at most of the positions in bone, where the shift method gave deviations larger than the mean deviation, a failure of delivering the planned range could not be proven. Variations in the absolute values of measured and simulated activity distribution, degradations in the measured activity distribution due to activity fractions from different overlapping treatment fields, or a coarse voxel dimension in profile direction were found to be responsible for these discrepancies. These examples show that a ‘blind’ range verification by PET/CT measurements is questionable. Positions where discrepancies between planned and delivered range are detected have to be carefully investigated further to rule out other explanations for the deviation.

In soft tissue point wise range verification turned out to impractical due to the degradation of the measured activity distribution by blood perfusion. Point wise range verification via PET/CT measurements relies on a good landmark as well as absolute agreement between measured and simulated activity distribution. The shift range verification is more robust for spatial variations in the activity distribution and relies on an overall agreement of the characteristic of two distributions. The shift method showed the potential of range verification within 4.3 mm in soft tissue (case (iii)) and even within 2.2 mm if the last maximum of the activity distribution lay in bone (case (ii)). However, for 27% (33%) of the positions in soft tissue for case (ii) (case (iii)) the shift method gave deviations larger than ±5 mm. In soft tissue it is even more complex to distinguish reasons for these deviations. Therefore, reliable range verification within 1-5 mm in soft tissue (case (iii)) by offline PET/CT scans was found to be infeasible.

Biological washout effects limit the area per treatment field where range verification is possible. To overcome this problem, better models of the washout processes and more robust analyzing tools are needed. Also shorter delay times between irradiation and PET imaging would minimize the washout of the produced β^+-emitters by blood perfusion [Par08]. A detailed discussion of the work in progress concerning these possible enhancements of the PET/CT range verification approach are given in section 7.1 and 7.2.

5.4.3 Motion

Patient motion during the 30 minutes of data acquisition at the PET/CT results in a blurring of the measured activity distribution. To investigate the magnitude of blurring, lateral conformity between measured and simulated activity was analyzed in 14 patients. Examples of 6 patients can be seen in Figure 5.7. The extent of blurring can be especially well determined if the lateral fall-off takes place in bone tissue (see positions marked by a red arrows in Figure 5.7), because washout of the activity due to blood perfusion will be minimized there.

Lateral blurring in abdomino pelvic tumor sites ranges up to 30 mm, compared to conformity for head and neck tumor sites ranging up to 5 mm. Lateral blurring is dominant in the anterior-posterior direction, reflecting the breathing motion during the 30min of PET scan.

The breathing motion prevents range verification especially for anterior and/or posterior treatment fields in the abdomino pelvic region, as illustrated in the left of Figure 5.8. For superior/inferior treatment fields, anterior-posterior breathing motion disables spatially dissolved range verification by PET/CT imaging. However, a range verification would be possible, in case of a uniform range per field. This situation is illustrated in the middle two pictures in Figure 5.8. Since the range varies within most treatment beams to match the distal edge of the tumor, anterior-posterior patient motion also affects the range verification ability for any beam direction, as seen in the right of Figure 5.8. Thus unavoidable patient motion during the PET data acquisition excludes most tumor sites in the thoracic cavity from mm-accurate range verification via the current 3D PET/CT imaging strategy.

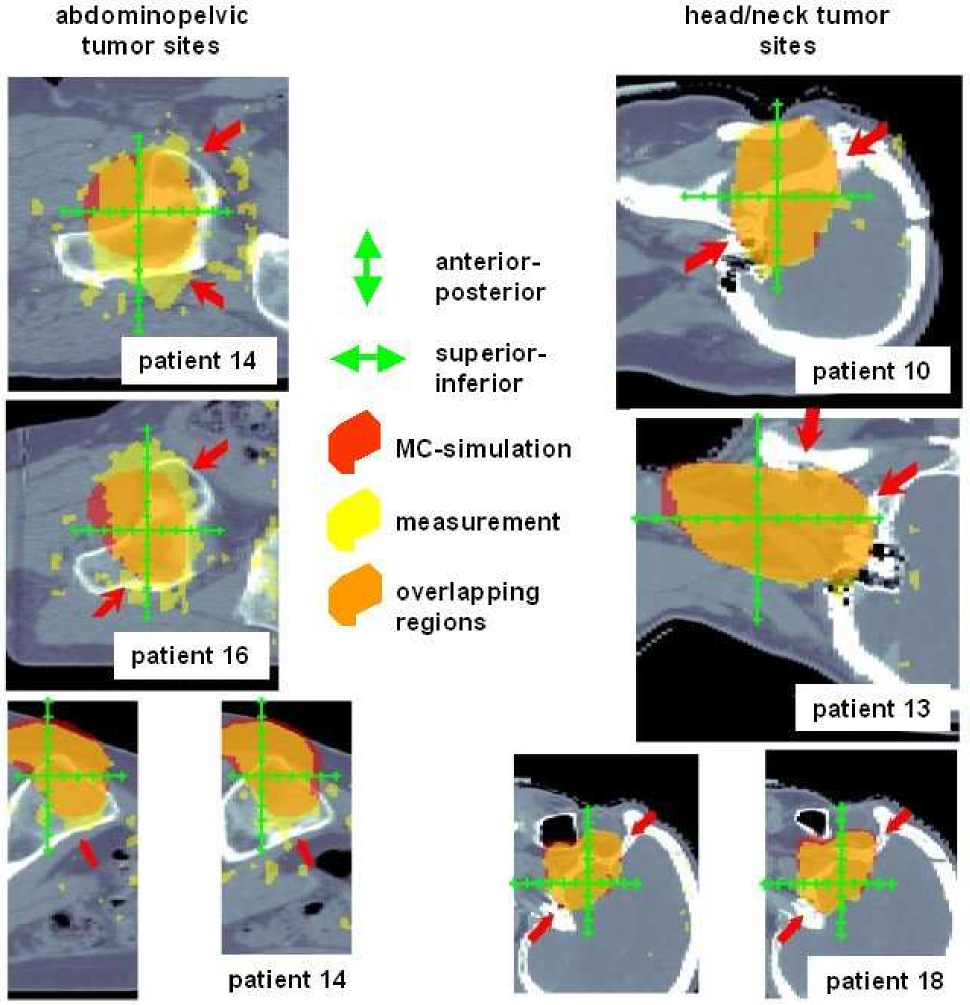

Fig. 5.7: Lateral conformity between MC-simulated and measured activity distribution for three exemplary abdomino pelvic (three images on the left) and three exemplary head (three images on the right) patient cases (Green scale with ticks in 1 cm intervals, red arrows point to positions where the lateral fall of occurs in bone).

5.4.4 Simulation uncertainties

Treatment verification is achieved by comparing measured with MC simulated activity distributions. The accuracy of the MC simulated activity distribution depends mainly on the precise knowledge of the elemental composition and the washout characteristics of the underlying tissues. Tissue characteristics are assigned by means of HU from the patient planning CT. The main challenges of this approach are discussed in the following subsections:

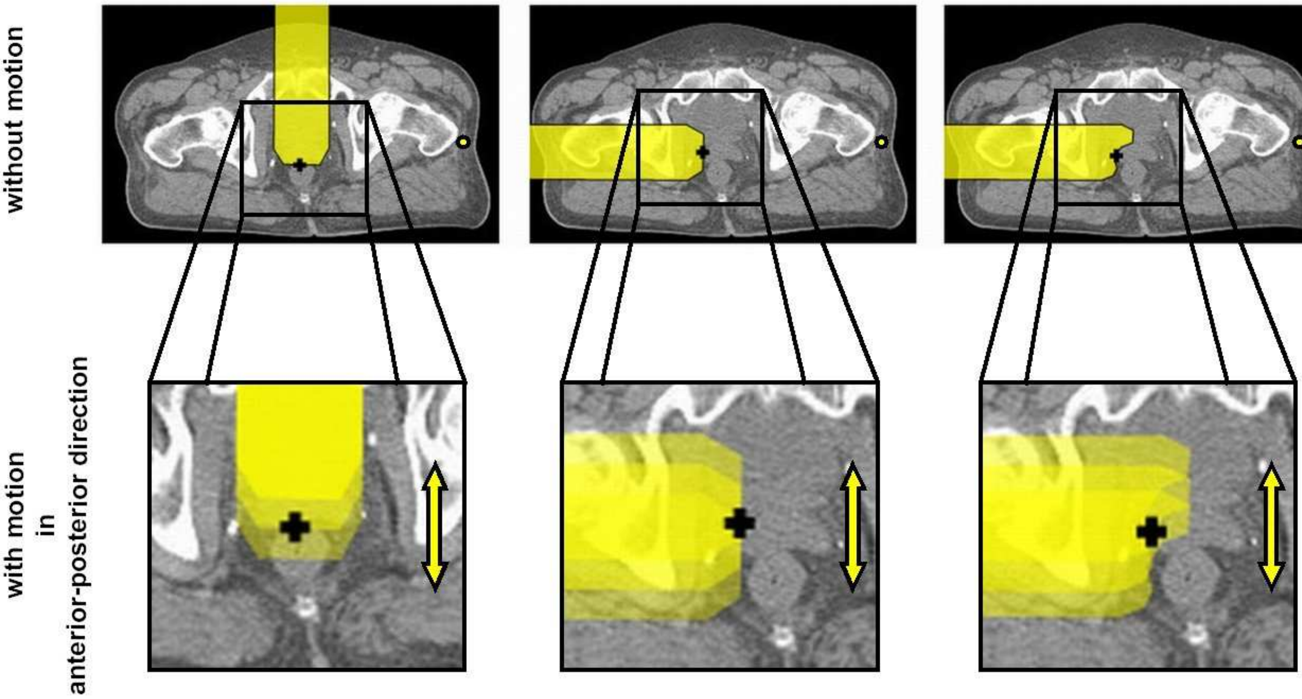

Fig. 5.8: Influence of anterior-posterior breathing motion on the range verification ability of anterior treatment fields (left), superior treatment beams with uniform range (middle) and superior treatment fields with varying range (right).

- To investigate the ability of tissue identification by means of CT data, HU values for different organs were evaluated. This way it was investigate whether a HU mapping is sufficiently correlative to assign organ specific elemental compositions and washout characteristics.

- To investigate the sensitivity of the MC simulation on the HU mapping, activity distributions calculated with different HU maps were compared. Furthermore, MC simulations using different washout models were compared.

Correlativity of HU mapping

The difficulty of tissue identification increases with an increasing variety of tissues present in the tumor proximity. The more different tissues are present the less correlative is the conversion from HU into specific tissues. The HU analysis for a head patient, displayed on the left of Figure 5.9, shows clearly separated HU domains for fat, brain and bone tissue. The HU analysis for an abdomino pelvic patient, displayed on the right of Figure 5.9, however, shows overlapping HU domains. HU for bone marrow (red framed region) are between -20 and 110, which is in the same HU domain assigned to soft tissue (blue framed region).

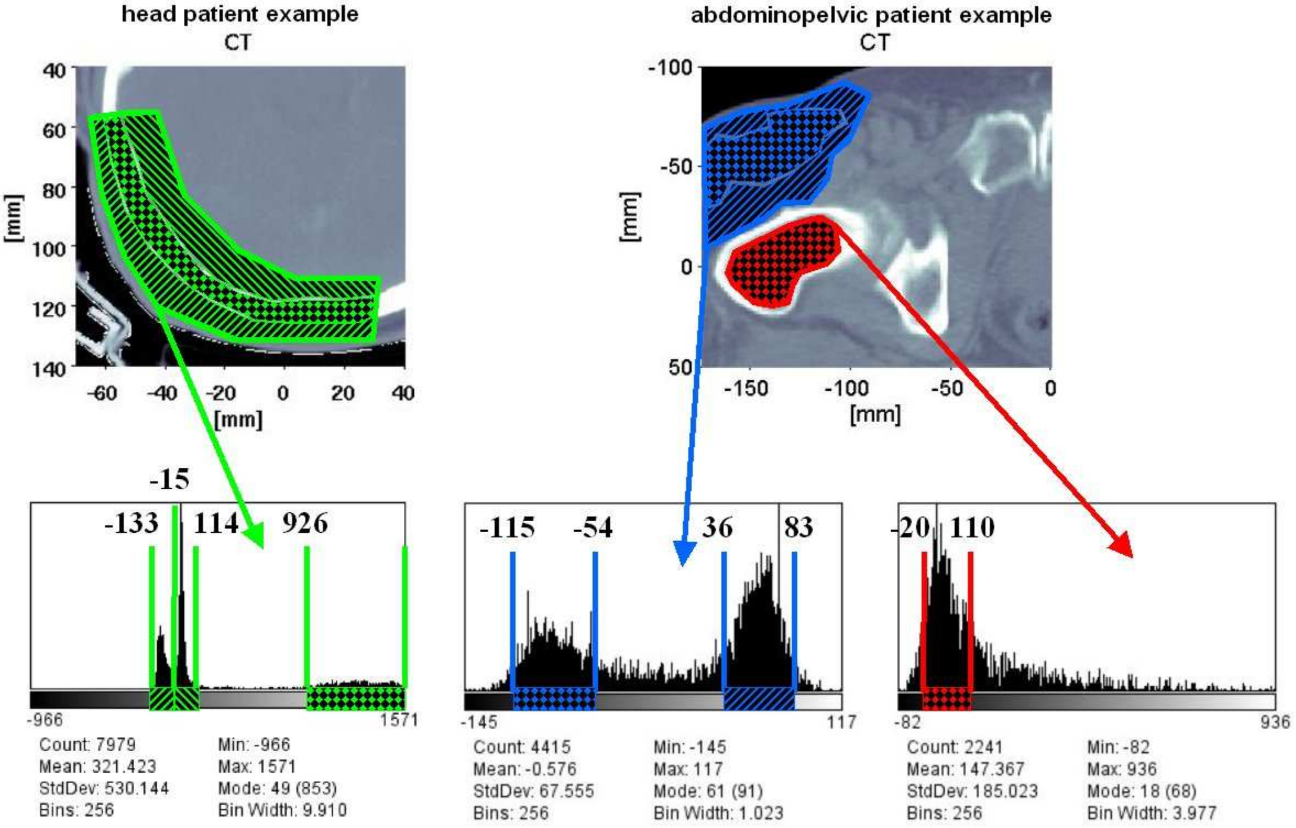

Fig. 5.9: HU analysis for an exemplary head patient (left) and an exemplary abdomino pelvic patient (right).

Conversion of HU into mass density and elemental composition is currently based on a segmentation of the CT scan into 26 materials sharing the same composition and a nominal mean density for -1000 $\leq$ HU $<$ 3060 [Par02, Par07a, Schn00]. For HU $\geq$ 3060 Titanium is assigned [Par07a]. HU values between -20 and 120 are assigned to four materials with elemental compositions given in Table 5.3. These materials accurately reflect soft tissues, but differ from the elemental composition of bone marrow, which is given in the last row of Table 5.3.

HU	**H(%)**	**C(%)**	**N(%)**	**O(%)**	**Na(%)**	**P(%)**	**S(%)**	**Cl(%)**	**K(%)**
-22 - 7	10.8	35.6	2.2	50.9		0.1	0.2	0.2	
8 - 18	10.6	28.4	2.6	57.8		0.1	0.2	0.2	0.1
19 - 80	10.6	28.4	2.6	57.8		0.1	0.2	0.2	0.1
80-120	9.4	20.7	6.2	62.2	0.6		0.6	0.3	
bone marrow	11.0	52.9	2.1	33.5		0.1			

Tab. 5.3: Conversion of HU between -22 1nd 120 to elemental weights based on [Schn00]. The elemental composition of bone marrow is given in the last row.

The abdomino pelvic patient example shows that the HU mapping is not sufficiently correlative to assign organ specific elemental compositions and washout characteristics in the MC simulations. A possible method to overcome the problem of overlapping HU domains would be an assignment of elemental compositions and washout characteristics based on manually delineated organ contours as proposed in [Par07b].

Sensitivity of the MC simulation on the HU mapping

The influence of different HU to elemental composition conversions and different washout models on the range verification ability of the offline PET/CT approach is investigated in the abdomino pelvic patient example, studied in the previous section. Figure 5.10 shows a comparison between MC simulated and measured activity in this patient. The MC simulation was performed using the Schneider HU conversion and the washout modeling described in section 3.2.1, which will be referred to as the 'original' parameters throughout this section.

It is noticeable that the measured activity distribution on the left is much more blurred than the simulated one on the right. This is due to washout effects, motion and the need of prostate patients to void their bladder between irradiation and imaging. These effects can only roughly be taken into account in the simulation. Furthermore, one can clearly see an underestimation of activity in bone marrow by the MC simulation. The low activation in bone marrow in the simulated activity can be explained by the fractions of carbon assigned to HU values between -20 and 110 by the Schneider conversion. While these fractions resam-

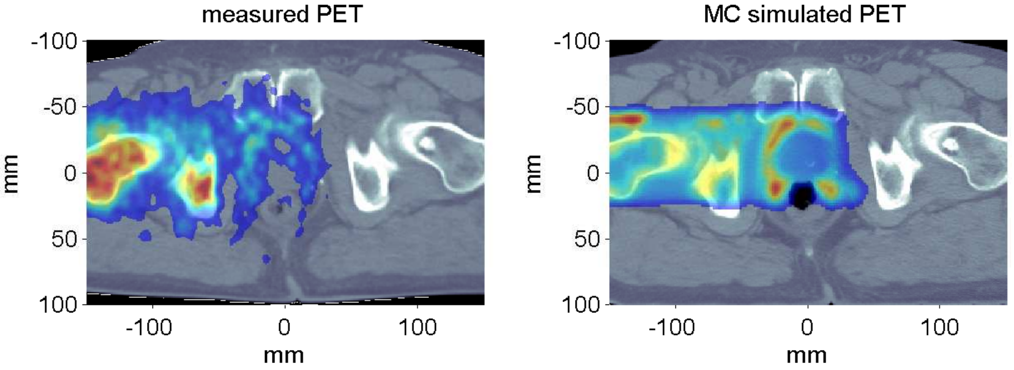

Fig. 5.10: Comparison of a measured and MC simulated activity distribution in an abdomino pelvic tumor site.

ple the composition of soft tissue, the fraction of carbon in bone marrow is underestimated by almost 50%, as seen in Table 5.3. Since the main part of activation is produced through the (p, pn) channel on ^{12}C, the Schneider HU conversion results in an underestimation of activity in bone marrow. Furthermore, HU between -22 and 110 are assigned to highly perfused tissue in the original washout model, which further increases the underestimation of activation in bone marrow by the MC simulation.

Figure 5.11 shows a MC simulated activity distribution using (i) the original parameters described in section 3.2.1(upper row), (ii) a different HU conversion (second row left) and (iii) a different washout model (second row right). In the last row difference plots of the original MC simulation and the two adjusted simulations can be seen, respectively. The adjustments in the HU conversion and the washout model were done with the goal of improving the similarity between measured and simulated activity distribution, and in particular to reduce the differences in bone marrow areas. The HU to elemental composition conversion was adjusted in a way that assured the same range in the dose distribution for a simulation with and without adjustment. For HU domains between -22 and 120 the assigned elemental composition was changed to the elemental composition of bone marrow, seen in the last row of Table 5.3. To compensate the few mm range change in the dose distribution caused by this new assignment, density correction factors were introduced. The original washout model and the adjustments can be seen in table 5.4. A low perfusion domain was added for HU between -22 and 120, associated with bone marrow.

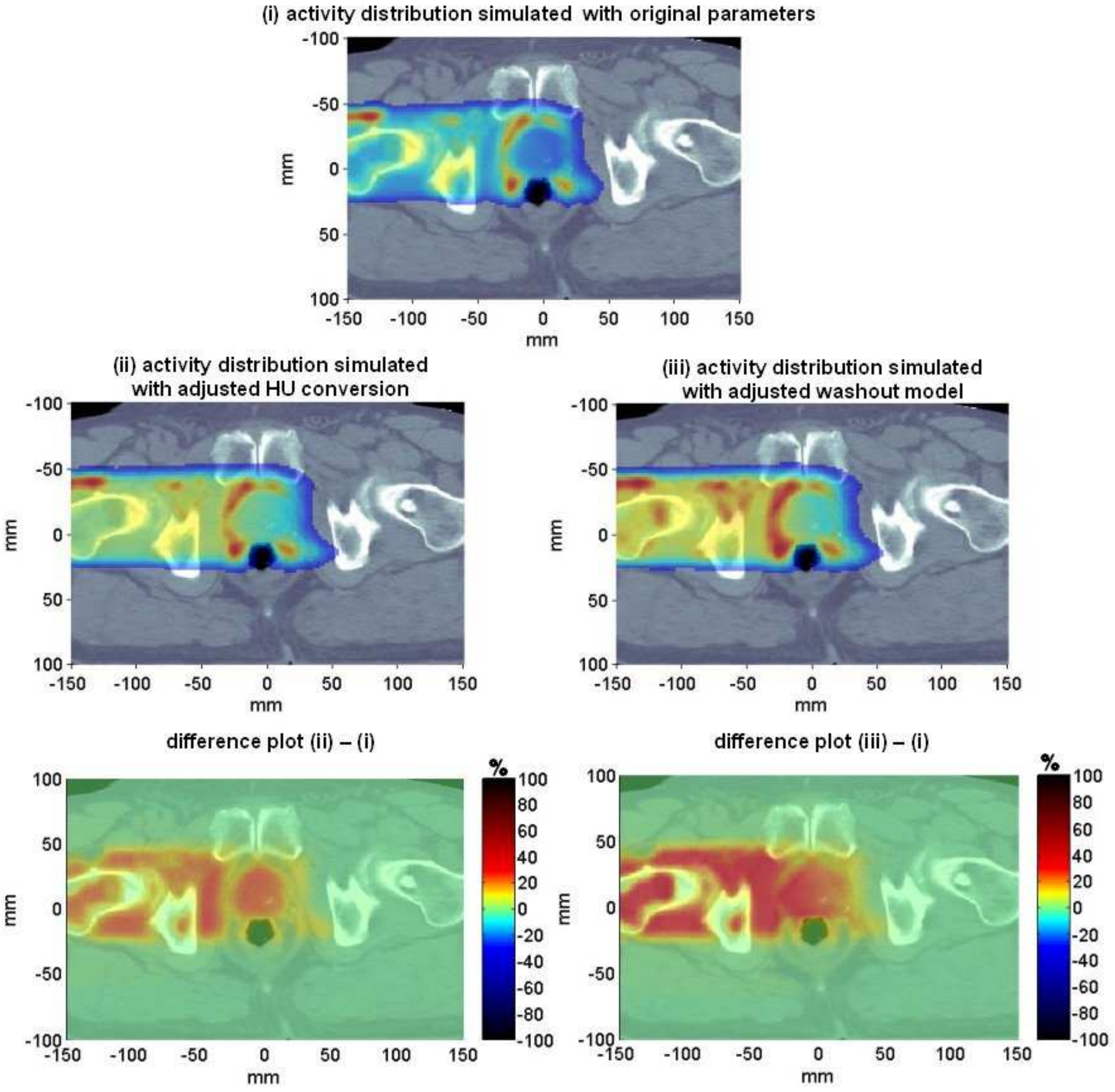

Fig. 5.11: MC simulated activity distribution using (i) the 'original' parameters described in section 3.2.1 (first row), (ii) an adjusted HU conversion (second row left) and (iii) an adjusted washout model (second row right). In the last row, different plots of the respective distributions can be seen.

The difference plots in figure 5.11 show that the absolute values in the MC simulated β^+-activity are very sensitive on the HU conversion and the washout model. Deviations of up to 27% appear in MC simulated activity distribustions, using once the orginal and once

	$HU<-150$	**fat** **$-150\leq HU\leq -30$**	**soft tissue** **$-30<HU<200$**	**soft bone** **$200\leq HU<1000$**	**compact bone** **$HU\geq 1000$**
$\mathbf{T}_{1/2,bios}[s]$	3500	15000	3500	8000	15000
$\mathbf{M}_S$	0.55	0.9	0.55	0.6	0.9

	$HU<-150$	**fat** **$-150\leq HU\leq -21$**	**bone marrow** **$-22\leq HU\leq 120$**	**soft tissue** **$120<HU<200$**	**soft bone** **$200\leq HU<1000$**	**compact bone** **$HU\geq 1000$**
$\mathbf{T}_{1/2,bios}[s]$	3500	15000	15000	3500	8000	15000
$\mathbf{M}_S$	0.55	0.9	0.9	0.55	0.6	0.9

Tab. 5.4: Original and adjusted parameters for the washout model used in the MC simulation (i) and (iii).

the adjusted HU conversion. Deviations of up to 36% appear when using different washout models. Thus, the deviation between measured and simulated activity of about 45% seen in section 5.3.1 can be explained in large parts by the rough estimate of parameters in the MC simulation.

The overall similarity between the measured and simulated activity distribution in this patient example does not improve much, despite the adjustments in the HU conversion and the washout modeling. One explanation is that the adjustment does not only affect specific tissues, but entire HU domains associated with different tissues. While differences between measured and simulated activity decrease in bone marrow, they increase for soft tissue. Beyond this problem, that will be apparent for all parameter assignments based on HU, it is also noticeable that even with adjustments there are big differences in the absolute activity values between measurement and simulation in bone marrow. This shows that the parameters established for bone marrow are imprecise, and that parameters for activity simulation in abdomino pelvic tumor sites need to be further investigated and adjusted.

Adjustments in the HU conversion or the washout modeling can also affect the range verification. Figure 5.12 shows depth profiles of the planing CT, the simulated dose, and the measured/simulated activity distributions through the isocenter. Profiles of the simulated distributions are displayed using the original, as well as the adjusted parameters. One can nicely see that the dose profiles almost perfectly overlay each other, no matter which HU conversion was used in the MC simulation. On the contrary, major variations are noticeable in the activity profiles. Table 5.5 shows range deviations in the activity profiles for the use of different parameters in the MC simulation. Adjustment of the parameters can cause range differences in the simulated activity distribution of about 1.8 mm.

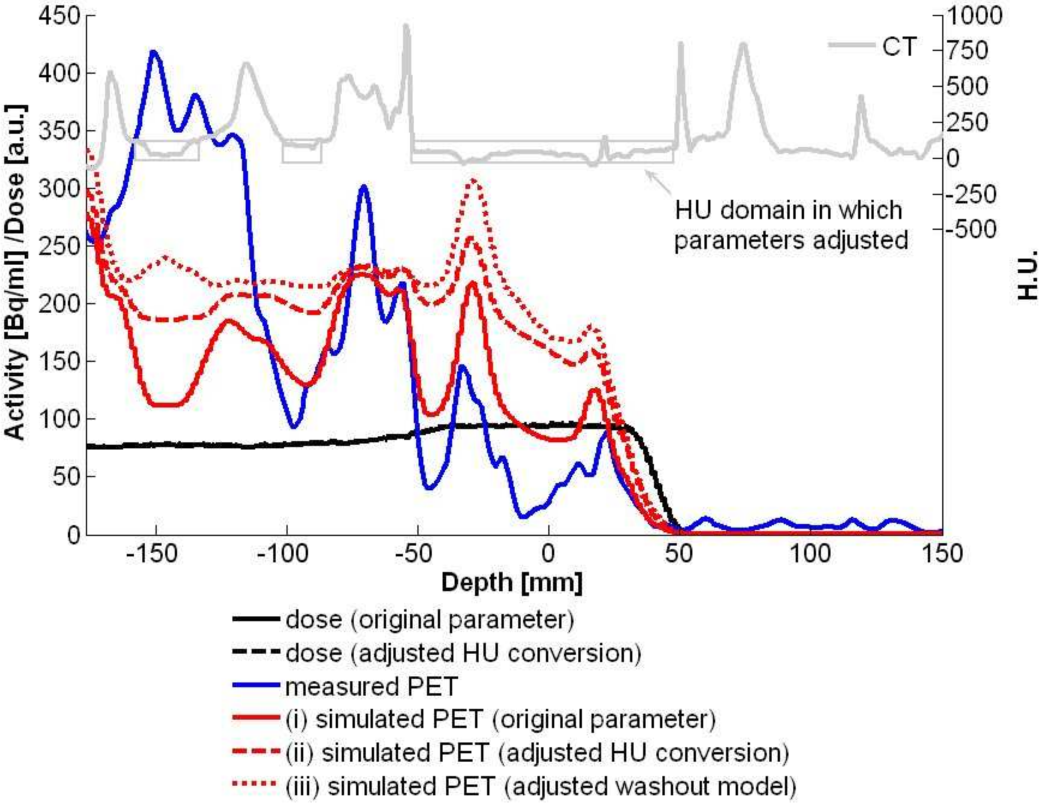

Fig. 5.12: Profiles of the planing CT, the simulated dose and the measured/simulated activity distributions: Profiles of the simulated distributions are displayed using the original as well as the adjusted parameters. Simulated dose profiles using different parameter sets almost perfectly overlay each other.

	20% range (method A)	**50% range** (method B)	**shift** (method C)
$R_{orig.param.} - R_{adj.HUconv.}$[mm]	1.80	2.41	1.81
$R_{orig.param.} - R_{adj.washoutmodel}$[mm]	1.70	2.28	1.81

Tab. 5.5: Activity range differences caused by parameter changes in the MC simulation.

The previous analysis indicates that activity simulations are very sensitive to the HU conversion and the washout models, contrary to dose simulations. Different parameters do not only affect the absolute values of the simulated activity, but also the activity range. The HU conversion and washout model described in section 3.2.1 were established for head/neck and paraspnal tumor sites. For abdomino pelvic tumor sites careful adjustments have to be made. Rough modeling of parameters can easily result in 30% uncertainty in the absolut activity values, and 2 mm uncertainty in the activity range.

5.4.5 Tumor site specific challenges

In the previous sections, biological washout, motion, and uncertainties in the MC simulations were discussed. They are the main challenging factors for the in vivo offline PET/CT approach and affect more or less all tumor sites. In addition to these three factors, there exist conditions that compromise the PET/CT range verification approach only for a selection of tumor sites:

Beam directions: Range verification via post treatment offline PET/CT imaging is only feasible for single beams, or for beams delivered nearly perpendicular to each other in a single fraction. For opposed beams or for beams with small angles the distal edge in the activity distribution is a result of protons from multiple beam directions. In these beam configurations it is therefore difficult to achieve range verification separately for each treatment field. Opposed beam directions are more likely in abdomino pelvic treatment areas (sacrum, prostate) than in head and neck tumor patients. Patients #12, #15, #18 (see table 3.1) are examples, in which PET/CT range verification failed due to the beam arrangement.

CT fusion: Differences in the positioning of the patient during treatment and during PET imaging are taken into account by fusing the planning CT and the PET CT. For patients with tumors in the eye, a CT of only a very small area around the target is obtained for treatment planning. This does not allow fusion with the PET CT [Par07b]. Patient #7 (see table 3.1) is an example in which CT fusion was not feasible. In this case correct alignment of the measured and simulated activity distribution was based on the matching of fiducial markers. This procedure is expected to introduce lager uncertainties than the usual fusion of CT images. The accuracy of the CT fusion depends on the rigidity of the patient geometry. Head and neck tumors provide a higher degree of rigidness than abdomino pelvic tumor sites. Here the position of the legs for example can influence the whole geometry of the tumor area.

Organ position: For prostate tumors, a site-specific limitation is the need of the patients to void their bladder between treatment and imaging. This changes the geometry for the PET/CT imaging, as compared to the situation during treatment. The change in geometry appears in a way that cannot be taken into account by the rigid CT fusion, and only with difficulty by means of non-rigid registration. In the scope of this study, two patients with tumors in the prostate (patient #14 and #16) have been imaged. Also for patients that cannot be immobilized in the same way during PET/CT imaging and treatment, such as eye patients (patient #7), organ motion is a challenge.

Table 5.6 summarizes all previous results by assigning tumor site-specific weighting factors to all the different challenges of PET/CT range verification. A value of 1/green means ‘this site is only slightly influenced by this factor’, 2/orange means ‘this site is influenced by this factor, but there are ways to minimize the influence’ and 3/red means ‘this site is highly influenced by this factor and also improvements of the method would not resolve this influence’. Note that the assigned factors partly based on very limited patient cases. Table 5.6 is intended as a guideline to estimate the benefit of offline PET/CT range verification for different patient groups.

The cumulative weighting factors in the last row of table 5.6 reflect the result of mean range deviations between measured and MC simulated activity distributions, broken down for different tumor locations (Figure 5.3 right). The current offline PET/CT range verification approach is a promising tool for head and neck patients, while it currently faces insuperable limitations for abdomino pelvic tumor sites.

challenge **tumor location**	biological washout	motion	MC uncertainties	beam direction	CT fusion	organ position	**cumulative weighting factor**
Spine	1	1	1	1	2	1	**7**
Head	2	1	1	2	1	1	**8**
Thorax	2	3	2	1	2	2	**12**
Eye	2	2	2	1	3	2	**12**
Abdomen	3	3	3	2	3	2	**16**
Prostate	3	3	3	3	3	3	**18**

Tab. 5.6: Tumor site-specific weighting factors for the different challenges of the PET/CT range verification method.

5.4.6 Particularly promising patient groups for PET/CT range verification

Patients with tumors in the head and neck region

Current experience clearly emphasizes that patients with tumors in the head and neck region can benefit most from offline PET/CT range verification. The main limiting factor for head tumor sites are biological washout processes. Efforts to develop better models for washout processes are currently under way and are discussed in section 7.2. In section 7.1 the performance of the PET/CT approach for shorter delay times is investigated. There the influence of washout effects is compared for offline and in-room PET measurement. In in-room data acquisition there is almost no delay between irradiation and imaging and thus the influence of washout processes is expected to be minimal.

Head and neck patients often combine very inhomogeneous tissue arrangements in the beam path with tumor locations very close to critical structures. The good performance of the PET/CT approach makes urgently needed range verification feasible for routinely use in the near future.

Patients with arteriovenous malformations (AVMs)

Patients with AVMs represent a special class within the group of head and neck patients. AVM is a tangle of dilated blood vessels that disrupts normal blood flow in the brain. Prior to radiotherapy treatment the patients obtain embolization - a deliberate obstruction of a blood vessel with a specially designed glue. The 'emboli' formed by this agent plugs the vessels of the AVM, reducing the size of the nidus and thereby creating a smaller target for irradiation. However, the induced material causes major artifacts on the CT due to its portion of tantalum. For treatment planing specific density measurements of the glue used are done. The target area is delineated manually based on MRI images to assure an irradiation, as precise as possible. However, the irradiation of AVM patients implies more uncertainties than treatments of other head tumor sites. PET/CT measurements could be used as an additional quality assurance tool. Since most of the AVM patient treatments follow a hyperfractionated schedule, PET/CT measurement are especially promising. The high dose per fraction (typically 8-16 Gy(RBE)) translates into enhanced image quality in the PET scan. Delineation or density uncertainties can result in under or overshooting. Offline PET/CT measurements could be used to monitor these errors in dose in the first treatment fraction, so that the second fractions could then be corrected accordingly.

Figure 5.13 shows images of an AVM patient receiving three treatment fields of a total dose of 8 Gy(RBE). A right-posterior field was followed by a right-superior field and a left-posterior field. The same treatment fraction was irradiated and imaged twice within one week.

Artifacts caused by the tantalum portion of the inserted glue are apparent in the CT in Figure 5.13. As in section 5.4.1, images from the repeated PET/CT data acquisition show impressive similarity. After the first irradiation and PET data acquisition it was found that the range of the right-superior field had been slightly underestimated. Therefore, it was extended by 3 mm in the second irradiation and PET data acquisition. Figure 5.14 shows activity range differences between the two data acquisitions for the right-superior treatment beam.

Despite the 3 mm range adjustment in the second irradiation, the mean range difference in the activity distributions of the right-superior treatment beam is 0.13 mm between the two data acquisitions. There are various explanations, for why the range adjustment is not

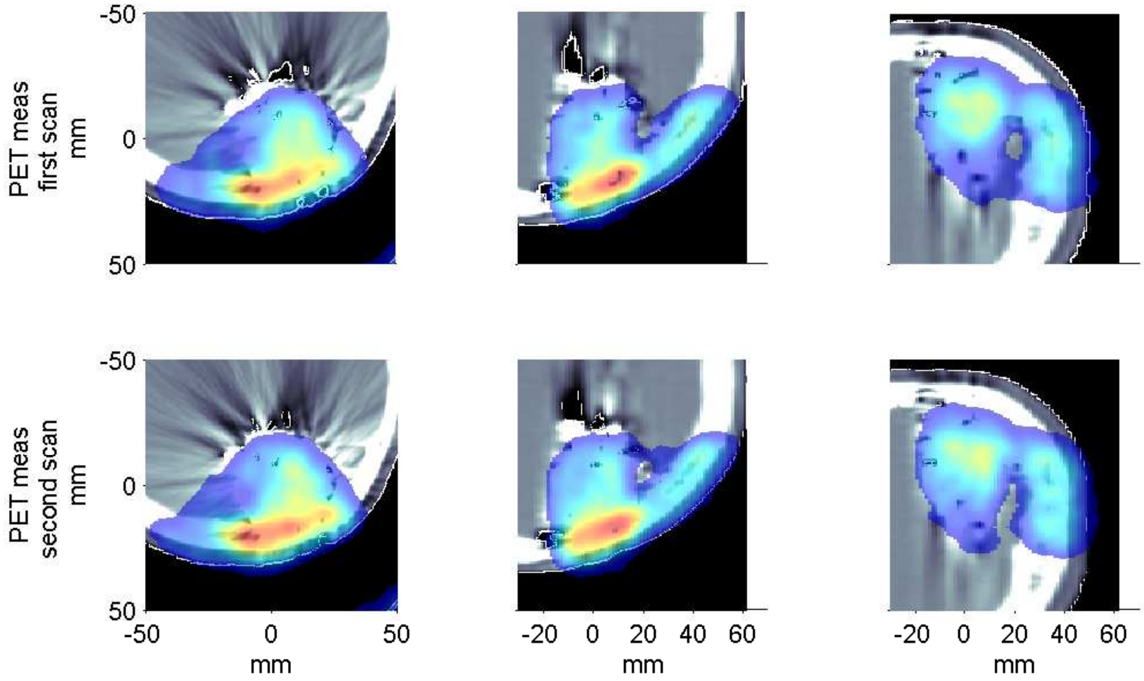

Fig. 5.13: Transversal, sagittal and coronal slice through the isocenter of the measured activity distribution. The first row shows images from the first scan. In the second row the corresponding images from the second data acquisition can be seen.

reflected in the activity measurements. First of all, the intended 3 mm adjustment could not really have been delivered. A check of the error in the actually delivered ranges was done in a water tank. Intended beam ranges of 10 cm and 10.3 cm were measured to be 10.06 cm and 10.22 cm when delivered. This gives an error of about ±0.8 mm in the delivery. Thus the intended range adjustment of 3 mm could have shrunk to 1.2 mm when delivered. Furthermore, the PET scanner measures the accumulated activity of all the treatment fields delivered in one fraction. Thus the distal fall-off of the right-superior field is overlaid with the lateral fall-off's of the two posterior fields. Even so the beam range was changed in the right-superior field, it could be that the corresponding edge in the activity distribution remains the same because it is mainly determined by the two posterior fields. Finally, the influence of washout effects could have blurred the activity distribution, so that the activity range difference is not noticeable anymore.

PET/CT range verification is particular desired and promising in AVM patients. How-

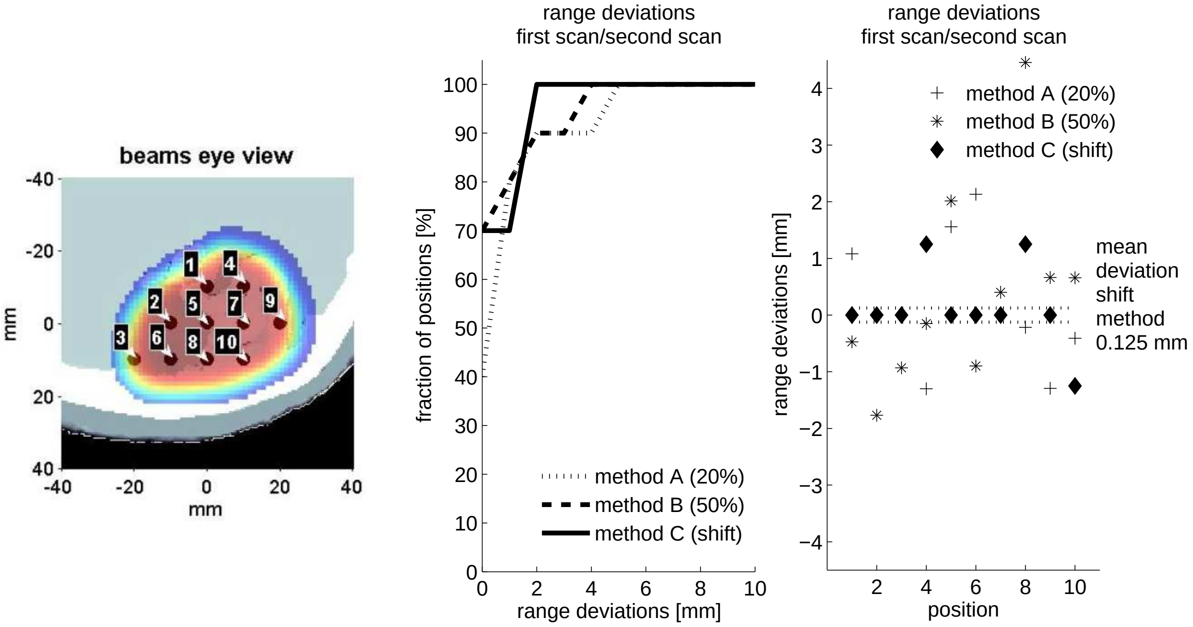

Fig. 5.14: Left: Profile positions. Middle: %-occurrence of absolute range deviations between two PET/CT scans. Right: Range deviations at each position. The mean absolute range deviation evaluated with the shift method was 0.125 mm.

ever, the previous discussion also shows particular challenges. On the one hand, the hyper fractionated treatment schedule offers high doses per fraction and thus a good signal to noise ratio. On the other hand, it creates the necessity to deliver multiple fields per fraction. Since offline PET scans only measure the accumulated activity, range verification for each field is difficult to resolve.

Patients with metal implants

Dose calculation and treatment planning for patients with metal implants is challenging for two reasons: First, pencil-beam algorithms have difficulty handling geometries including metal regions. Secondly, CT artifacts impede accurate dose planning. Artifacts in the planning CT either cause dose undershoots or dose overshoots. The effects of artifacts are very case dependent as addressed in [Jäk07]. Figure 5.15 shows a comparison between calculated and measured activity distribution in a patient with metal implants. The PET measurement confirmed that the overshoot in the simulated activity distribution had not actually been delivered.

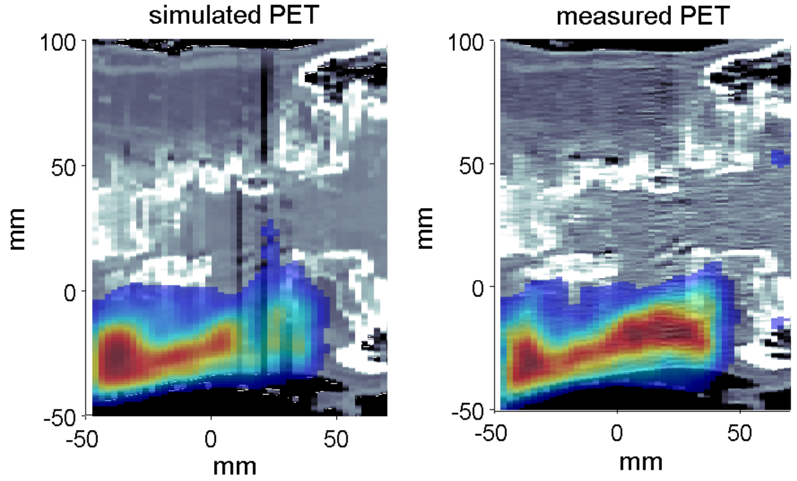

Fig. 5.15: Comparison between calculated (left) and measured (right) activity distribution in a patient with metal implants.

As seen in the example above, PET/CT measurements are capable of validating correct treatment delivery in the case of metal implants. Predicted over or undershoots can be excluded by imaging the first treatment fraction. This way, PET/CT imaging can be employed as a quality assurance tool for the successive treatment fractions. However mm-accurate range verification fails in the presence of metal implants due to the attenuation correction of the PET images, which is also affected by artifacts.

5.5 Discussion

Deviations of about 45% between the measured and MC simulated activity absolute values could be seen in the qualitative analysis of section 5.3. Repeated PET/CT data acquisition, as investigated in section 5.4.1, showed that measured activity values could only be reproduced within a 30% uncertainty. In section 5.4.4 it could be seen that different HU maps and washout models can affect MC simulated activities up to 36%. These uncertainties in the quantification of activity values show that the current PET/CT approach is not feasible to verify absolute dose information. Improvements in the HU mapping based on a better understanding of tissue compositions are needed. Furthermore, washout models have to be expanded. Precise space (i.e., tissue) and time-dependent weighting factors, especially for tumor locations other than head and neck, have to be established. If at all, a verification of absolute dose values is only possible for an assignment of elemental compositions and washout characteristics based on manually delineated organ contours, as proposed in [Par07b].

However, PET/CT imaging is a promising tool for range verification. Previous evaluation of data coming from a well-balanced patient population allows a distinction between limitations and conquerable challenges of the PET/CT range verification approach for each considered tumor site. For head and neck tumor sites range verification within an accuracy of 1-2 mm is feasible. The main limitation here is biological washout in soft tissues, which degrades the measured activity distribution. In abdomino pelvic tumor sites, mm-accurate offline PET/CT range verification is currently not feasible. This is primarily due to patient motion and complex tissue heterogeneities that introduce uncertainties in the MC simulation. However, in this tumor location PET/CT imaging is usable for quality assurance. Despite the uncertainties, wrong dose calculation due to CT artifacts can be falsified by PET imaging. In abdomino pelvic patient cases that involve a lot of uncertainties, PET range verification with an accuracy of currently 5-6 mm might be valuable.

6. SUMMARY

Radiotherapy treatment with protons enjoys rising interest and importance with an increasing number of clinical proton therapy facilities worldwide. In particular, for inoperable tumors growing in close proximity to critical organs the high selectivity of protons has an enormous potential benefit. Protons of a certain energy exhibit a specific range which determines the position of the maximum dose delivery in the target. To make full use of this superior characteristic, techniques are required that allow a millimeter precise monitoring of the proton trajectory and especially the proton range. At present, PET imaging represents the only feasible method for in vivo and noninvasive proton range verification.

In this thesis we mainly studied offline PET/CT range verification. The measured activity signal is correlated but not directly proportional to the spatial pattern of the delivered dose. Therapy control is achieved by comparing the measured activity distribution with a prediction based on the treatment plan and the specific time course of the particular irradiation. To employ offline PET/CT range verification clinically, it is crucial to know whether disagreements between measured and predicted activity maps reflect errors in the treatment planning, calculation or delivery, or whether they are caused by inherent limitations of the method.

It was found that the physical properties are provided to perform mm-accurate range verification by offline PET/CT imaging, but that the approach faces several challenges in clinical applications. Biological washout processes impede a range verification in well perfused tissues, motion prevents mm-accurate results in abdominopelvic tumor sites, and limitations in the MC simulation compromise the feasibility of the method for tumor regions with many different tissues in close proximity. Furthermore, tumor site specific conditions like certain beam direction configurations or destined patient positions limit the applicability of the method. Thus the current approach allows 1-2 mm accurate range verification only at specific positions and for a limited patient subgroup.

However, most of the challenges can be overcome or at least constricted. The problem of biological washout, for example, could be tackled by on line PET imaging. CTP imaging could help to develop better models to account for those perfusion processes in the MC simulation. 4D-PET (gated PET) could help to solve the problem of motion. Detailed contouring of structures in the CT and corresponding assignment of tissue parameters could help to overcome limitations in the MC simulation.

This thesis has contributed to the achievement of PET/CT imaging as a promising clinical monitoring technique. Data of a well-balanced patient population were evaluated to identify possible technological and methodological improvements in order to allow for a wide applicability of PET/CT range verification. PET/CT imaging is currently the only feasible in vivo and noninvasive way to verify the actual delivered range in three dimensions after proton treatments. Advanced image guided radiation therapy (IGRT) techniques may allow to recognize possible sources of range uncertainties, but they can not measure their actual impact. MC simulation can predict dose distribution with very high precision, but they are limited in regards to the underlying CT information. Post treatment PET imaging is the only technique that takes into account all possible source of errors and allows treatment monitoring in a direct way. The work of this thesis will be continued to provide the benefit of PET treatment verification to as many patients as possible in clinical routine.

7. FUTURE PERSPECTIVES AND WORK IN PROGRESS

7.1 Investigation of on line PET measurements

In this thesis activity distributions solely from offline PET measurements were studied. The delay between the end of treatment and the beginning of PET data acquisition was in average 15 min. This delay and the fact that patients needed to walk to another building for the PET scan introduces various uncertainties. The repositioning of the patient at the PET scanner, for example, causes a slightly different geometry between irradiation and PET imaging. Furthermore, over time, biological washout processes degrade the induced activity pattern. To minimize the influence of those uncertainty factors on line PET data acquisition was proposed [Par08].

In collaboration with the radiology department at MGH we currently testing a movable NeuroPET scanner (PhotoDetection Systems, Inc [PDS08]) for proton treatment verification. This scanner is positioned on wheels and can be moved into the treatment room. The patient can remain on the treatment couch for the PET scan, merely the position of the couch has to be rotated and/or shifted (see Figure 7.1). By using the NeuroPET scanner, the time gap between treatment and imaging can be reduced to one minute. The NeuroPET scanner has a 305 mm aperture, 270 mm transverse FOV diameter and 240 mm axial FOV. The relatively small opening allows to image the head or extremities with high precision. The scanner's intended use is the diagnosis of brain diseases. Brain tumors, strokes, and neuron-damaging diseases causing dementia (such as Alzheimer's disease) change the brain metabolism. These changes can be detected in PET scans. Because the NeuroPET components are compact and require no specialized infrastructure, NeuroPET scanners enable neurological imaging at lower cost than whole body scanners.

Compared to the PET/CT scanner used throughout this thesis, the NeuroPET scanner is missing the additional option to take a CT scan for image coregistration. However, since the patient can remain in the same position during treatment and imaging, the geometry

variations are expected to be smaller than the uncertainties in the fusion of the planning and the PET CT. The NeuroPET scanner has a sensitivity of 15 kcps/MBq and a spatial resolution of 4.3 mm, which is both higher than for the conventional PET/CT scanners.
registration. However, since the patient can remain in the same position during treatment and imaging, the geometry variations are expected to be smaller than the uncertainties in the fusion of the planning and the PET CT. The NeuroPET scanner has a sensitivity of 15 kcps/MBq and a spatial resolution of 4.3 mm, which is both higher than for the conventional PET/CT scanners.

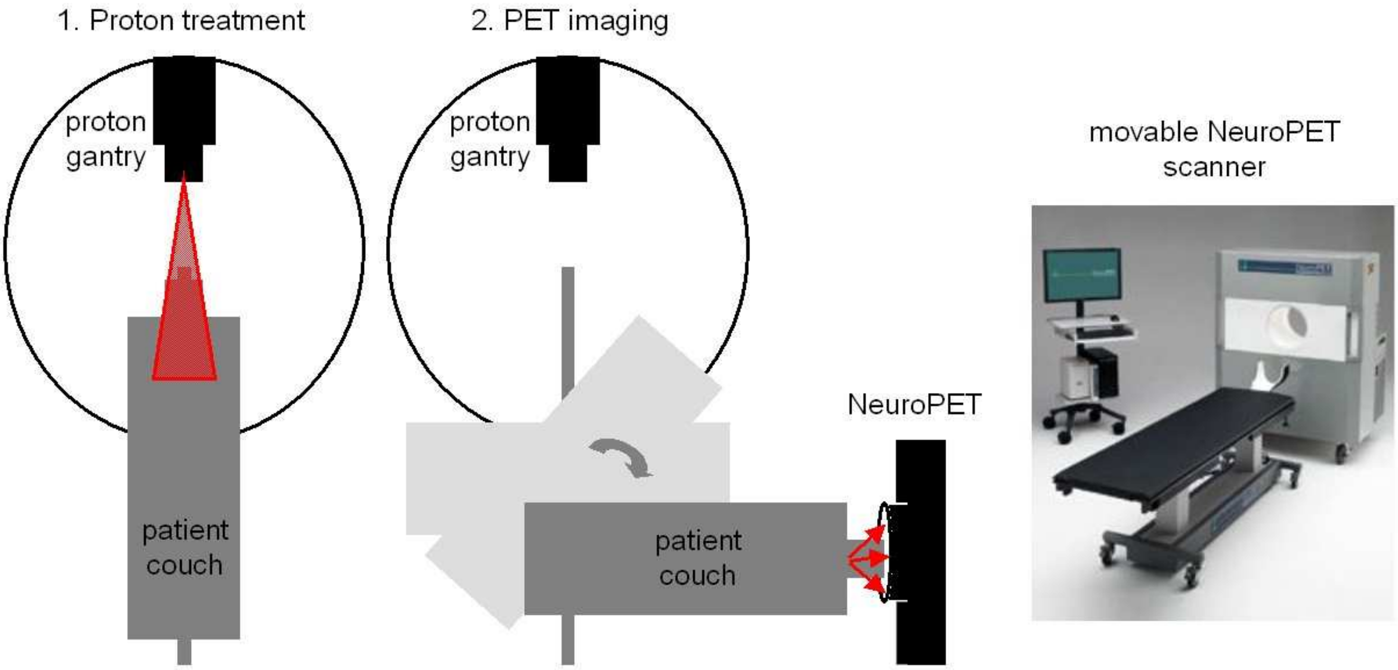

Fig. 7.1: Treatment and PET imaging set up for the use of a NeuroPET scanner shown in the picture on the right.

The applicability of the NeuroPET scanner for proton treatment verification was recently tested in a rectangular phantom (9 x 9 x 20 cm, PMMA plastic). The phantom was irradiated with a proton beam of 5 cm diameter, 16 cm water equivalent range and 10 cm modulation. A total dose of 8 Gy(RBE) was given. Following irradiation, the phantom was scanned for 30 minutes in the NeuroPET scanner starting 9.5 minutes post exposure. This experiment was repeated under exactly the same conditions using the conventional PET/CT scanner. Even though a shorter delay between irradiation and imaging would have been possible for the NeuroPET scan, it was chosen to follow the same schedule for both data acquisitions in order to have comparable results. Figure 7.2 shows the phantom setup at the NeuroPET as well as at the PET/CT scanner. For image coregistration markers that are recognizable in the CT as well as in the PET, were used. This is illustrated in the lower row of Figure 7.2.

Phantom setup:

Makers used for image coregistration:

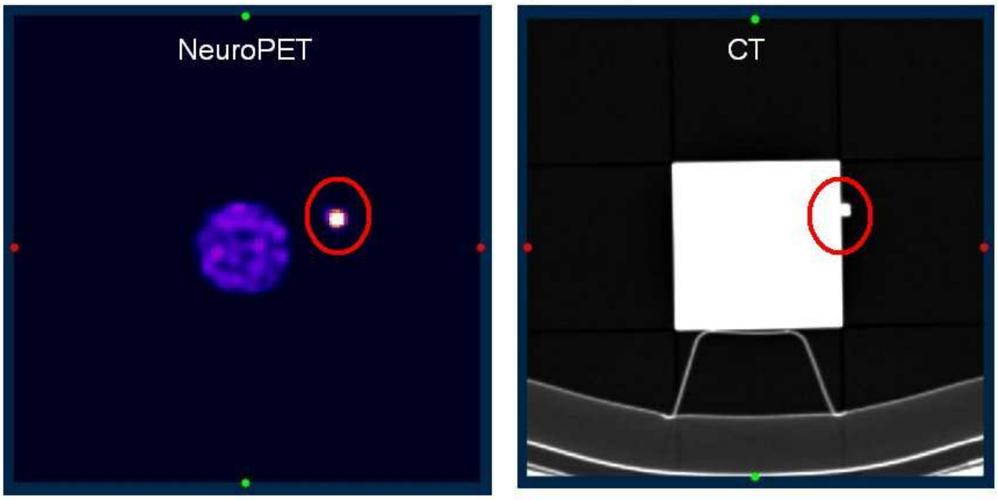

Fig. 7.2: Pictures in the upper row show the phantom setup during the NeuroPET and the PET/CT scan. In the activity pattern on the left as well as in the CT image on the right in the lower row one of six markers used for image coregistration can be seen in the red circles.

Figure 7.3 shows a comparison of activity patterns acquired with the NeuroPET (upper row) and with the conventional PET/CT scanner (lower row). In the graph on the left, one can see activity depth profiles at position zero for both scanners. The activity ranges agree within 2.5 mm at the 50% fall off position.

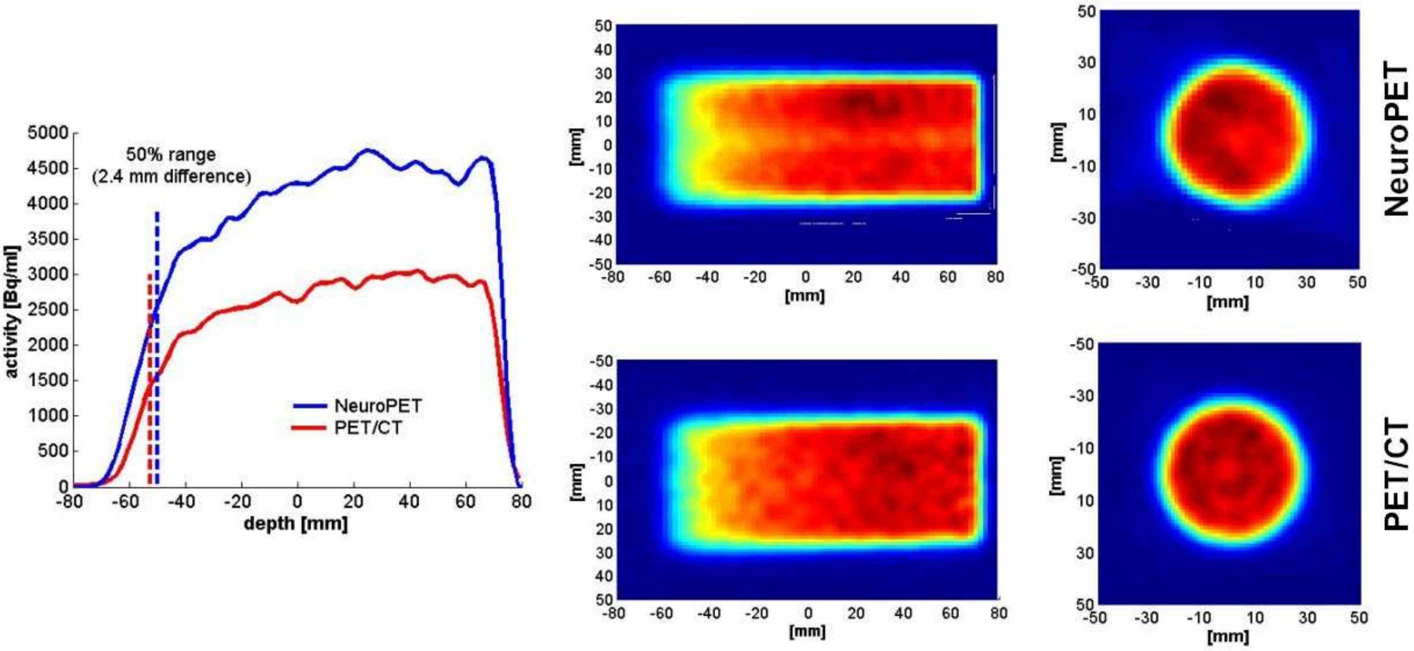

Fig. 7.3: Comparison of activity patterns acquired with the NeuroPET (upper row) and with the conventional PET/CT scanner (lower row). The graph on the left shows activity depth profiles at position zero for both scanners.

In the 2D-color wash images one can recognize that the activity patterns from the conventional PET/CT scanner look more symmetric and homogeneous than the ones from the NeuroPET scanner. This could be the result of the different attenuation correction approaches of the two scanners. While the PET/CT scanner provides a CT image directly prior the PET data acquisition, the NeuroPET scanner relies on an independently acquired CT image for attenuation correction. In our phantom experiment, the CT from the PET/CT scanner was used for attenuation correction of activity patterns of both scanners. While the phantom was positioned on a card frame at the NeuroPET, it was placed on the patient couch for imaging at the PET/CT scanner, as seen in Figure 7.2. The CT of the PET/CT scanner therefore contains the couch contours that were not present in the FOV of the NeuroPET scanner. The attenuation correction based on the CT with the couch contours therefore introduces unsymmetries and inhomogeneities in the reconstructed NeuroPET images. To avoid this source of uncertainties in the future, CT images used for attenuation correction of the NeuroPET images either have to be corrected for structures that are not present in the FOV, or exactly the same setup has to be used during CT and NeuroPET imaging.

Figure 7.4 shows an analysis of the count rate of the two scanners over time. In the left graph count rates at the isocenter in time frames of 1-2 min up to 1-20 min after the begin of data acquisition can be seen. In the right graph activity depth profiles over the corresponding time frames can be seen for both scanners. The NeuroPET scanner shows approximately 1.7 times more counts over the scanning period of 30 minutes than the conventional PET/CT scanner, reflecting its higher sensitivity. The availability of high count rates from several chemical species, each with a characteristic life time, could enable to separate the contributions of each isotope in the reconstructed activity. This way PET imaging could be used to the rank of a multi-parametric imaging tool.

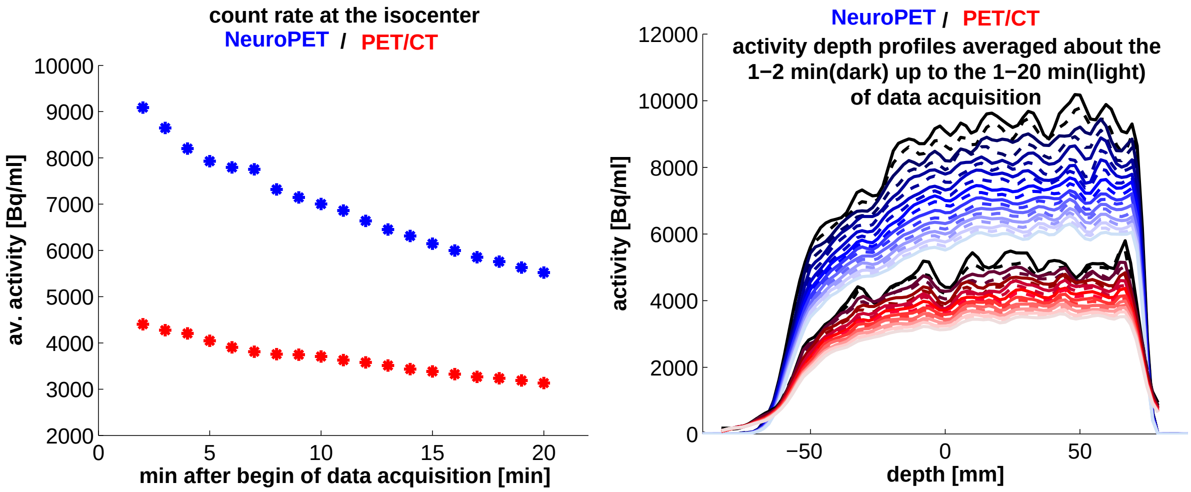

Fig. 7.4: Left: Average count rate at the isocenter for the 1-2 minute of data acquisition up to the 1-20 minute of data acquisition for the NeuroPET (blue) and the PET/CT (red) scanner. Right: Activity depth profiles for the same time frames (1-2 minutes dark colors up to 1-20 minutes light colors).

The promising results of the phantom study encourage first in room patient PET scans following proton treatment. The use of the movable NeuroPET scanner promises to enable high precision PET treatment verification. Head and neck proton patients could be scanned routinely, without image degradation due to washout effects or geometrical uncertainties due to repositioning.

7.2 Improvement of the biological modeling

For treatment validation the measured PET signal is compared to MC simulated predictions of the activity pattern. To simulate realistic activity pattern biological washout processes have to be taken into account. Currently this is done by means of space (i.e., tissue) and time-dependent weighting factors as described in section 3.2.1.

In collaboration with the Department of Radiation Oncology of the Maastricht University we try to improve our biological washout models. The idea is to use perfusion CT (CTP) images to obtain characteristic perfusion parameters for different tissues. Perfusion CT techniques typically require a baseline image acquisition without contrast enhancement followed by a series of images acquired over time after an intravenous bolus of conventional iodinated contrast material. The resulting temporal changes in contrast enhancement, often displayed as timeattenuation curves, are subsequently analyzed to quantify a range of parameters that reflect the functional status of the vascular system. Pixel-by-pixel analysis can produce quantitative parametric images with high spatial resolution. CT imaging perfusion parameters can be generated by using a number of approaches, which can be grouped into two major methods: compartmental analysis and deconvolution-based methods. Detailed mathematical and physical principles behind these methods of calculation are available for review in the literature [Mil03, Cre06, Mil03a, Win01, Cen02, Aks00].

7.3 Expansion of the filtering approach

By filtering the dose distribution along the main beam direction, the approach described in chapter 3.2.2 allows the calculation of three-dimensional PET distributions induced by proton beam irradiation. The method has been tested to calculate activity distribution resulting from carbon isotopes in homogeneous phantoms and in simple inhomogeneous phantoms [Par06]. Furthermore preliminary activity distributions for two patient cases were calculated, which were however restricted to the carbon activity channels and no biological washout or scanner responds effects were taken into account. On the strength of the promising results obtained, it would be desirable to extend the approach to more complex inhomogeneous phantoms. The ultimate goal is to calculate realistic activity distribution with the filtering method for patient cases taking into account all involved processes.

The possibility to perform activity measurement shortly after the proton treatment by means of the NeuroPET scanner as described in chapter 7.1 requires to extend the application of the filtering approach to short-lived isotopes (mainly ^{15}O and ^{13}N). In collaboration with the Department of Physics, University of Pisa and INFN Sezione di Pisa and the Heidelberg Ionenstrahl-Therapie (HIT) Center we currently determine filters for short-lived isotopes. It is planed to validate the activity distributions resulting from different isotopes and calculated with these new filter functions with MC simulated as well as with measured distributions. For the comparison with measured data the idea is to obtain activity distributions for different isotopes from NeuroPET measurements. Due to its high sensitivity, the NeuroPET scanner provides relatively high count rates. From the accumulated measured activity distribution it might be possible to separate count rates profiles from several chemical species due to their characteristic life time.

It is planed to establish a similar Matlab routine for the comparison of the measured activity distributions with filtered distributions, as used at the moment for the comparison with MC simulated distributions. This routine would be able to read in activity distributions from different isotopes calculated by the filtering method and weight and sum them according to the time line of the corresponding measurement. In addition it would take into account scanner responds effects and biological washout processes as described in chapter 3.2.1. Calculated activity distributions obtained from the filtering method could then be used as an alternative to the MC simulated activity distribution to validate the measurements.

In collaboration with the Department of Radiation Oncology, University Medical Center Mannheim we also work to improve the results from the inverse filtering approach. An inversion of the filter functions allows direct dose quantification from the measured PET distributions. However, this approach requires PET data of excellent signal-to-noise ratio. We work on different deblurring algorithms and regulators to obtain stable dose distributions from the measured activity distributions.

Since deblurring is noise sensitive it is necessary to consider the underlying noise distribution. PET is a low-photon imaging technique and thus the activity signals suffer from Poisson noise. A Richardson-Lucy approach [Ric72, Luc74] is perfectly suited for Poisson noise and is widely used for astronomy and fluorescence microscopy images containing Poisson noise. Furthermore, it is required to add a regularization technique to cope with the ill-posed nature of the deblurring problem. A popular choice is a total variation regularization (TV) [Neu98] being able to suppress noise amplifications and artifacts while at the same time preserving edges. A main issue of the analysis of the dose distribution is an accurate reconstruction of the distal fall-off region being a sharp edge. The edge preserving TV regularization is therefore well suited. In addition, using an anisotropic extension to the regularization favoring sharp edges is very promising to further improve the deblurring result.

APPENDIX

A. WORK FLOW

Figure A.1 shows an outline of the PET/CT range verification approach.

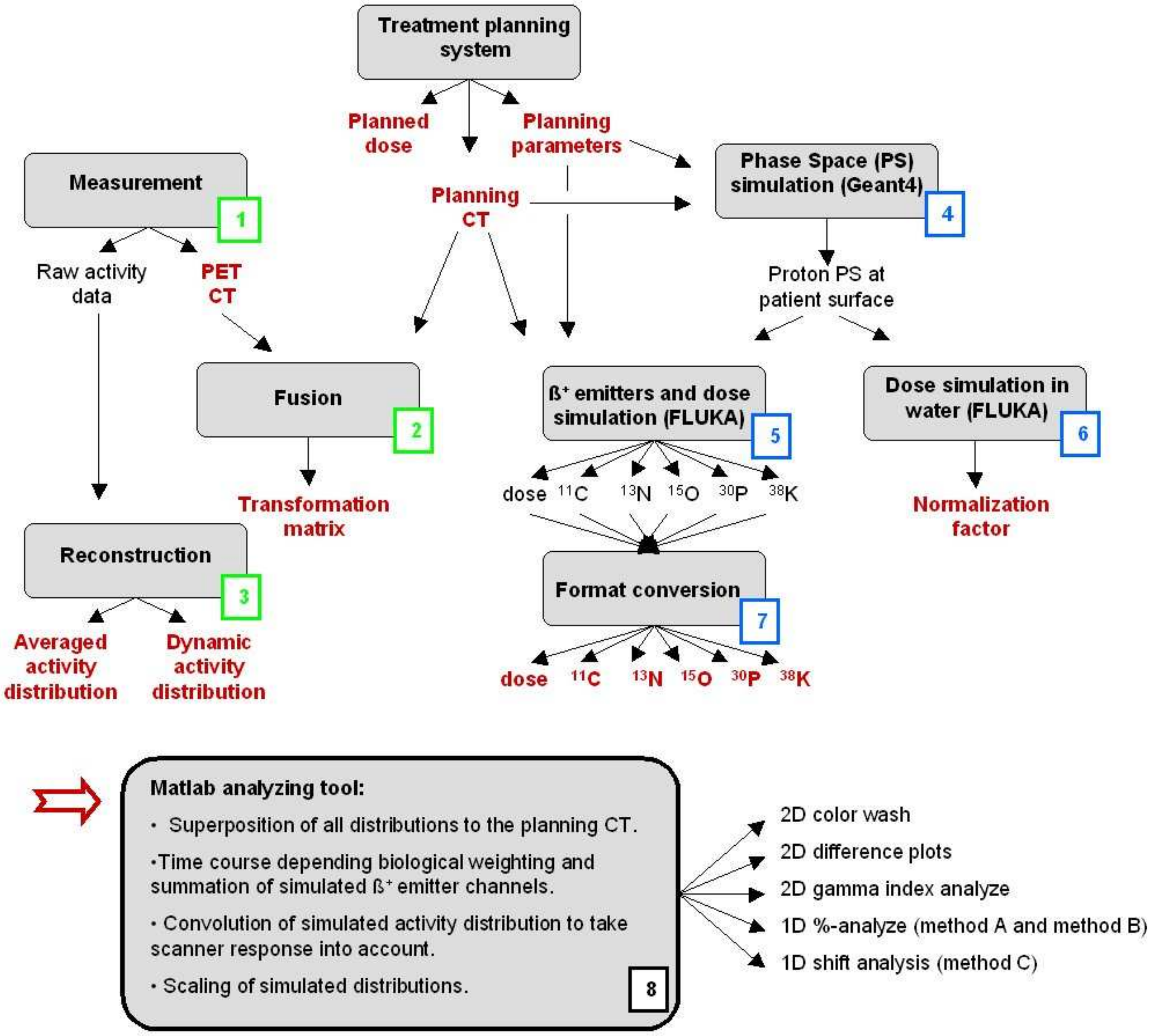

Fig. A.1: Outline of the steps involved in the PET/CT range verification approach. Green numbers denote processes associated with the data acquisition, blue numbers processes associated with data simulation. Red parameters act as input into the final Matlab analyzing tool.

The process of PET/CT range verification consists of many intermediate steps and many of the involved routines have been developed prior to this work. The framework of the Geant4 MC simulations is described in [Pag03, Pag04, Pag08] and details of the framework of the FLUKA simulations can be found in [Par07a, Par07b, Par07c]. In the scope of this thesis mainly the final analysis routine was expanded. The capability to evaluate difference plots and to perform a gamma analysis was introduced. For the one dimensional analysis the shift method described in chapter 3.4.2 was implemented. In the following parts marked by a number in Figure A.1 are described in detail.

1. Measurement

Prior to patient treatment and imaging, one has to make sure that the treatment position and fixation is feasible for PET/CT scanning. A printout of the dose fraction helps to speed up the patient positioning at the PET/CT scanner and to find the optimal bed position that covers the whole area of interest. At the day of data acquisition, the exact time schedule of the treatment and PET imaging should be noted to allow for a realistic MC simulation of the process later. Other parameters that should be recorded are the treatment room and the number of MU given in each field. At the PET scanner the data should be acquired in list mode for 31 minutes.

2. Reconstruction

After data acquisition, the PET images should be reconstructed with filtered backprojection (FBP) and ordered-subset expectation maximization (OSEM) algorithms. For later analysis, the images should be stored with and without attenuation correction. To study changes in activation over time, the data has to be reconstructed dynamically. In this study 20 time frames of 60 seconds and 5 time frames of 120 second were use for the dynamic reconstruction.

3. Fusion

The fusion matrix of the planning CT and the PET CT gives information about variations in the setup during treatment and PET imaging. For the fusion, the PET CT has to be transfered from the radiology to the proton center via the Picture Archive and Communication System (PACS), and has to be imported in the FOCAL treatment planning software

(Computerized Medical Systems, Inc., St. Louis, MO) used at our facility. The FOCAL software provides a package for rigid image fusion that writes out a fusion matrix.

4. Phase space simulation

As input for the dose as well as for the β^+ emitter simulations, ten phase spaces of 1.5 million protons should be simulated with Geant4, as illustrated in Figure A.2. The patient information from the FOCAL treatment planning software can be preprocessed by a routine called *MC_setup*. Besides a text file that contains all patient specific parameters, an aperture file, a compensator file, and the CT data in binary format are produced by this routine. All these files act as input for the MC phase space simulation. The input file for the MC phase space simulation can be produced by a script called *nozzle_in* that edits the information of the text file. The MC phase space simulation is executed by a script called *MC_PSD*. The resulting phase spaces should be summed up to one file of about one million particles, which can then be used as input for the dose and β^+ emitter simulations.

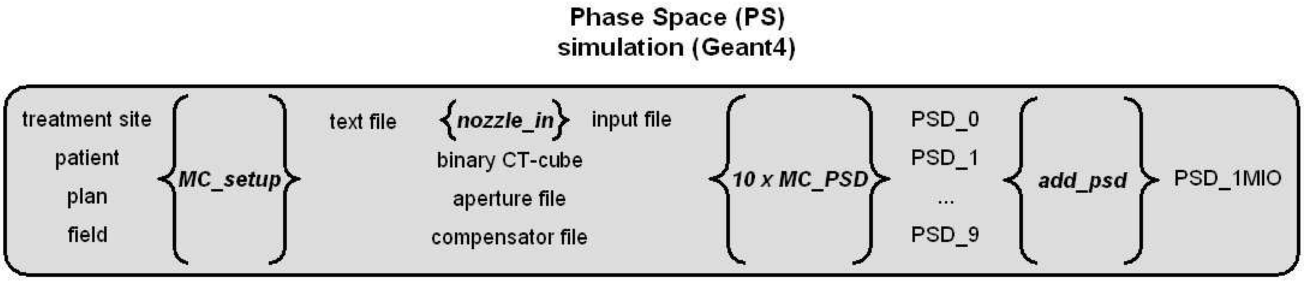

Fig. A.2: Flow diagram of in-/output parameters and scripts that need to be run to obtain a phase space file for the dose and β^+ emitter simulation.

5. Dose and β^+ emitter simulation

The dose and the activity distribution are simulated with FLUKA MC code following the steps illustrated in Figure A.3. Prior to the actual simulation, a script called *link_run_golem* has to be run. This script needs an input file called *writegolem* that contains the binary CT cube with a constant slice thickness and further information about the CT, like the number of voxels, the voxel dimensions, the position of the isocenter etc... One has to pay attention to correctly convert these parameters from the CT coordinate system to the FLUKA coordinate system. The *link_run_golem* script gives three geometry parameters and a *vxl file* that have to be included in a geometry input file for the actual FLUKA dose and activity simulation. Furthermore, it gives an *assigma file* that needs to be included in a second input file together with the phase space file and the setup information like the gantry position or the couch angle. It is advisable to run the FLUKA dose and activity executable *FLUKA_2008* ten times in parallel to gain enough statistic and to compensate for eventual failings of some runs.

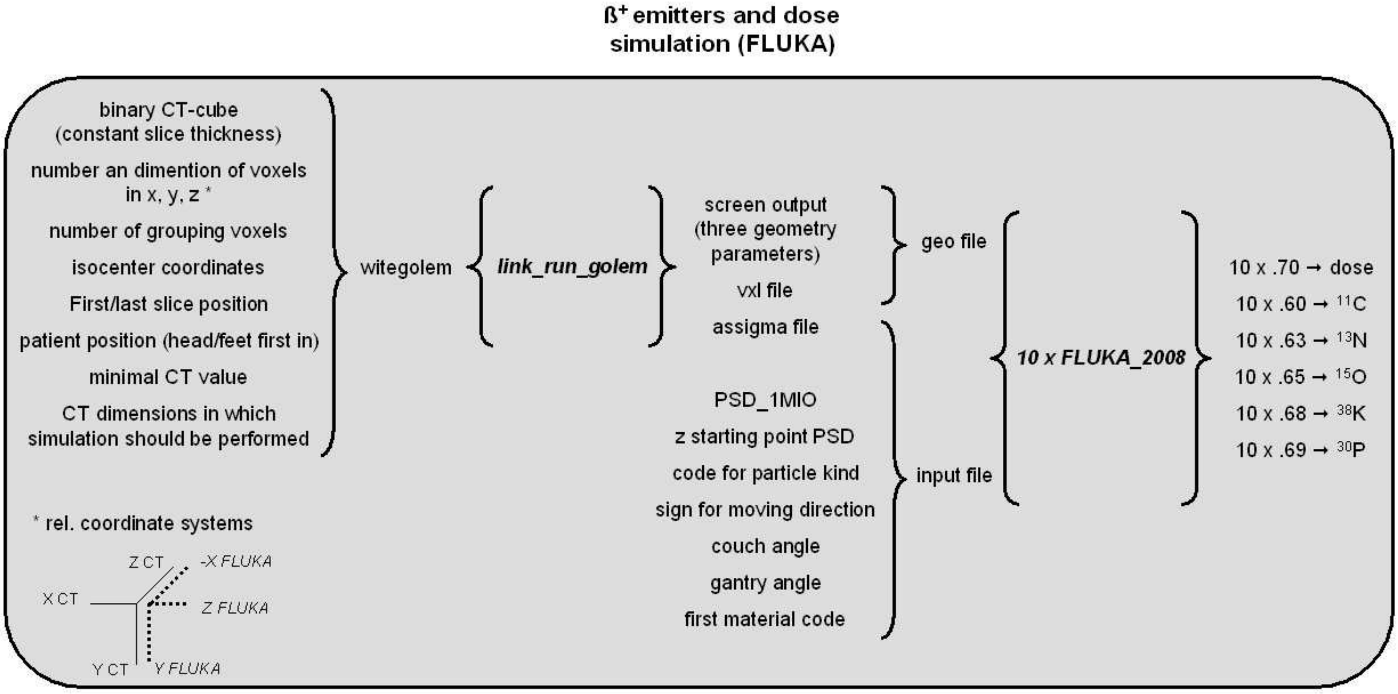

Fig. A.3: Flow diagram of in-/output parameters and scripts that need to be run to obtain dose and β^+ emitter distributions.

6. Absolute dose simulation

To scale the simulated dose and activity distribution correctly, one dose simulation of the phase space file in a water tank should be performed. The ratio between the simulated dose in water and the planned dose at the isocenter then gives the correct scaling factor.

7. Format conversion

To convert the simulated dose and activity distributions to the right format for the final analysis, a Matlab routine called *dose_flux* should be run. This routine also allows to sum simulated distributions from different runs.

8. Final analysis

The final analysis is performed by a Matlab routine called *PET_patient_StudyMGH*, which reverts to several subroutines. This routine is capable of comparing the measured and simulated activity distributions as well as the planned and simulated dose distributions as illustrated in Figure A.4.

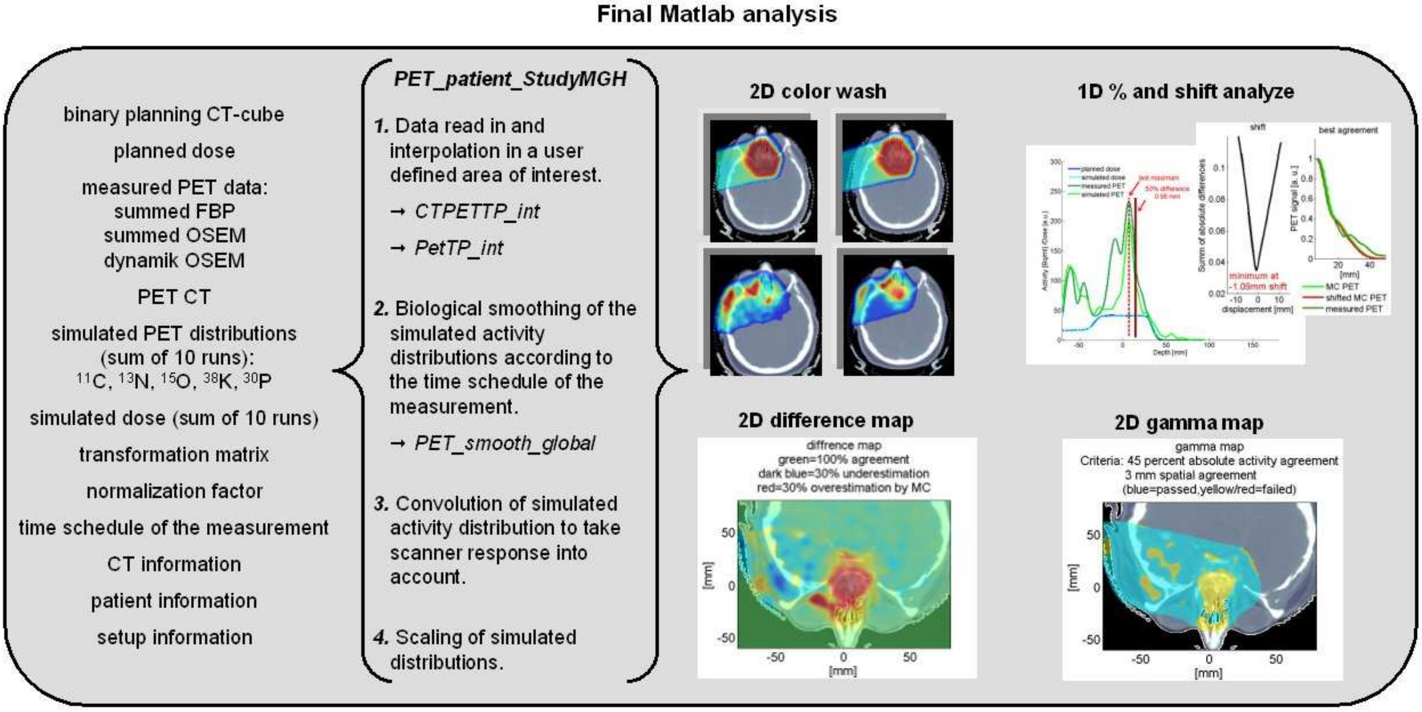

Fig. A.4: In- and output of the final Matlab analyzing script. In the brackets the different steps performed by the script are listed.

At first it reads in all collected Dicom data and interpolates all the data sets for a section that can be defined by the user. The routine will save the fused data in files called *CTPETTP_int* and *PetTP_int*, and will automatically call these saved files in later runs. This way the time and resource expensive data handling has to be performed only once. In the next step, the biological smoothing of the simulated activity distributions according to the time schedule of the measurement is performed. The smoothed distribution is stored in a file called *PET_smooth_global* for further use. Finally, the simulated activity distribution undergoes a convolution to account for scanner response effects and is scaled to the correct absolute values. The user can then choose between different two-dimensional or one-dimensional analyzing options.

BIBLIOGRAPHY

[Acs07] American Cancer Society (2007): Report sees 7.6 million global 2007 cancer deaths. Reuters. Retrieved on 2008-08-07.

[Ago03] Agostinelli S et al (2003): GEANT4 - a simulation toolkit. Nucl. Instrum. Methods A 506; 250-303.

[Aks00] Aksoy FG, Lev MH (200): Dynamic contrast-enhanced brain perfusion imaging: technique and clinical applications. Semin Ultrasound CT MR 21; 462477.

[Al08] Albertini F, Bolsi A, Lomax AJ, Rutz HP, Timmerman B and Goitein G (2008): Sensitivity of intensity modulated proton therapy plans to changes in patient weight. Radiother Oncol. 86(2); 187-94.

[Alb62] Albouy G, Cohen J P, Gusakow M, Poffe N, Sergolle H and Valentin L (1962): Spallation de L'Oxygene par des Protons de 20 A 150 MeV. Physics Letters 2; 306.

[And91] Andreo P (1991): Monte Carlo techniques in medical radiation physics. Phys. Med. Biol. 36:861-920.

[Att08] Attanasi F, Belcari N, Camarda M, Del Guerra A, Moehrs S, Rosso V, Vecchio S, Lanconelli N, Cirrone G A P, Di Rosa F and Russo G (2008): Experimental validation of the filtering approach for dosemonitoring in proton therapy at low energy. Phys Med. 24(2); 102-6.

[Bel07] Belhout A, Kiener J, Coc A, Duprat J, Engrand C, Fitoussi C, Gounelle M, Lefebvre-Schuhl A, Chabot M Hammache F and Benhabiles-Mezhoud H (2007): γ-ray production by proton and γ-particle induced reactions on ^{12}C, ^{16}O, ^{24}Mg, and Fe. Physical review. C 76; 034607.

[Ben75] Bennett G W, Goldberg A C, Levine G S, Guthy J, Balsamo J and Archambeau J O (1975): Beam localization via ^{15}O activation in proton-radiation therapy. Nuc. Instr. Meth. 125; 333.

[Ben78] Bennett G W, Archambeau J O, Archambeau B E, Meltzer J I and Wingate C L (1978): Visualization and transport of positron emission from proton activation in vivo. ascience 200; 1151.

[Ben98] Bendriem B and Townsend D W (eds) (1998): The theory and practice of 3D PET. Kluwer Academic Publishers, Dordrecht - Boston - London.

[Bet30] Bethe H A (1930): Zur THeorie des Durchgangs schneller Korpuskularstrahlung durch Materie. Ann. Phys. 5; 325.

[Blo33] Bloch F (1933): Zur Bremsung rasch bewegter Teilchen beim Durchgang durch die Materie. Ann. Phy. 16; 285.

[Bra04] Bragg W H and Leeman R (1904): On the ionisation curves of radium. Phil. Mag. 8; 726.

[Car97] Carlsson A K, Andreo P and Brahme A (1997): Monte Carlo and analytical calculation of proton pencil beams for computerized treatment plan optimization. Phys. Med. Biol. 42; 103353.

[Cen99] Cenic A, Nabavi DG, Craen RA, Gelb AW, Lee TY (1999): Dynamic CT measurement of cerebral blood flow: a validation study. AJNR Am J Neuroradiol 20;6373.

[Cen02] Cenic A, Nabavi DG, Craen RA, Gelb AW, Lee TY (2002): A CT method to measure hemodynamics in brain tumors: validation and application of cerebral blood flow maps. AJNR Am J Neuroradiol 21; 462470.

[Cre06] Crespo P, Shakirin G and Enghardt W (2006): On the detector arrangement for in-beam PET for hadron therapy monitoring. Phys. Med. biol. 51; 2143-2163.

[Cre07] Crespo P, Shakirin G, Fiedler Fine and Enghardt W (2007): Direct time-of-flight for quantitative, rael-time in-beam PET: a concept and feasibility study. Phys. Med. Biol. 52; 6795-6811.

[Del94] Del Guerra A, Domenico G Di, Gambaccini M and Marziani M (1994): A Monte Carlo simulation of the possible use of positron emission tomography in proton radiotherapy. Nucl. Instr.. Meth. A 345; 379.

[Del97] Del Guerra A, Di Domenico G, Mukhopadhayay D(1997): PET dosimetry in proton radiotherapy: a Monte Carlo Study. Appl Radiat Isot. 48(10-12); 1617-24.

[En99] Enghardt W, Debus J, Haberer T, Hasch B G, Hinz R, Jäkle O, Krämer M, Lauckner K, Pawelke J and Pönsch (1999): Positron emission tomography for quality assurance of cancer therapy with light ion beams. Nucl. Phys. A 654; 1047c-50c.

[Eng05] Engelsman M and Kooy H M (2005): Target volume dose considerations in proton beam treatment planning for lung tumors. Med. Phys. 32(12); 3549-57.

[Fas03] Fasso A et al (2003): The physics model of FLUKA: status and recent developments. Proc. Computing in High Energy and Nuclear Physics 2003 Conf.

[Fer05] Ferrari A, Sala P R, Fasso A and Ranft J (2005): FLUKA: a multi-particle transport code. Cern Yellow Report CERN 2005-10.

[Gau62] Gauvin H, Lefort M, Tarrago X (1962): Emission of alpha particles from the spallation reactions. Nuclear Physics 39; 447.

[Jäk07] Jäkel O, Reiss P (2007). The influence of metal artefacts on the range of ion beams. Phys Med Biol. 52(3);635-44.

[Jia04] Jiang H and Paganetti H (2004): Adaptation of GEANT4 to Monte Carlo dose calculations based on CT data. Med. Phys. 31; 2811-8

[Jia07] Jiang H, Seco J and Paganetti H (2007): Effects of Hounsfield number conversions on patient CT based Monte Carlo proton dose calculation. Med. Phys. 34; 1439- 1449.

[Kes08] Kesner A L, Lau V K, Speiser M, Hsueh W-A, Agazaryan N, DeMarco J J, Czernin J and Silverman D HS (2008): Time-course of effect of external beam radiation on [^{18}F]FDG uptake in healty tissue and bone marrow. Journasl of applied clinical medical physics 9; 147-156.

[Kie89] Kiener J, Berheide M, Achouri N L, Boughrara A, Coc A, Lefebvre A, Oliveira Santos F de and Vieu Ch (1089):γ-ray production by inelastic proton scattering on ^{16}O and 612C; Phusical Review C 58(4); 2175-2179.

[Kno07] Knopf A, Parodi K, Paganetti H, Cascio E, Bonab A, Bortfeld T (2007): Quantitative assessment of the accuracy of proton beam range verification with PET/CT. Abstract, 49th AAPM Meeting Minneapolis.

[Kno08a] Knopf A (2008): In-vivo Imaging in Particle Therapy. Invited talk 47th PTCOG Meeting Jacksonville.

[Kno08b] Knopf A, Parodi K, Paganetti H, Shih H, Bortfeld T (2008): Quantification of Clinical Limitations of Proton Beam Range Verification Using Offline PET/CT Due to Biological Washout Effects. Abstract, 50th AAPM Meeting Houston.

[Kno08c] Knopf A, Parodi K, Paganetti H, Cascio E, Bonab A and Bortfeld T (2008): Quantitative assessment of the physical-potential of proton beam range verification with PET/CT. Phys Med Biol 53; 4137-4151.

[Kno08d] Knopf A, Parodi K, Paganetti H, Cascio E, Bonab A, Bortfeld T (2008): Quantitative assessment of the reproducibility and the consistency of proton beam range verification with PET/CT. Abstract, 27th ESTRO Meeting Goeteborg.

[Kno09] Knopf A, Shih H A, Liebsch N, Parodi K, Paganetti H, Bortfeld T : Proton beam range verification with offline PET/CT scans - Clinical performances, challenges and limitations. to be submitted.

[Koe68] Koeher A (1968): Proton radiography. Science 160; 3034.

[Kra99] Kraft G (1999). RBE and its interpretation. Strahlenther. Onkol. 175; 44.

[Li08] Li G, Citrin D, Camphausen K, Mueller B, Burman C, Mychalczak B, Miller RW and Song Y (2008). Advances in 4D medical imaging and 4D radiation therapy. Technol Cancer Res Treat.7(1); 67-81.

[Lit93] Litzenberg D W, Bajema J F, Becchetti F D, Brown J A, Raymond R S, Roberts D A, Caraher J, Hutchins G, Ronningen R, Smith R, and Abbott M (1993): On-line monitoring ans P.E.T. imaging of proton radiotherapy beams. IEEE Trans. Nucl. Sci. 40; 954.

[Lit99] Litzenberg D W, Roberts D A, Lee M Y, Pham K, Vander Molen A M, Ronningen R and Bechetti D (1999): On-line monitoring of radiotherapy beams: experimental results with proton beams. Med. Phys. 26; 992.

[Low98] Low D, Harms W, Mutic S and Purdy J A (1998): A technique for the quatitative evaluation of dose distributions. Med. Phys. 25(5).

[Lu08] Lu HM (2008). A potential method for in vivo range verification in proton therapy treatment. Phys Med Biol. 53(5); 1413-24.

[Luc74] Lucy, L. B. (1974): An iterative technique for the rectification of observed distributions. Astronomical Journal 79 (6); 745754.

[Ma00] Ma C-M, Pawlicki T, Jiang S B, Li J S, Deng J, Mok E, Kapur A, Xing L, Ma L and Boyer A L (2000): Monte Carlo verification of IMRT dose distributions from a commercial treatment planning optimization system. Phys. Med. Biol. 45; 248395.

[Mil03] Miles KA, Griffiths MR (2003): Perfusion CT: a worthwhile enhancement? Br J Radiol 76; 220231.

[Mil03a] Miles KA (2003): Perfusion CT for the assessment of tumour vascularity: which protocol [Suppl]? Br J Radiol 76; S36S42.

[Min06] Min C H, Kim C H (2006). Prompt gamma measurements for locating the dose falloff region in the proton therapy. Applied physics letters 89(18); 183517.

[Miz03] Mizuno H, Tomitami T and Kanazawa M (2003): Washout measurements of radioisotope implanted by radioactive beams in the rabbit. Phys Med Biol 48; 22692281.

[Mor08] Mori S and Chen GT(2008). Quantification and visualization of charged particle range variations. Int. J. Radiation Oncology Biol. Phys. 72(1); 268277.

[Neu98] Neumaier A (1998): Solving ill-conditioned and singular linear systems: A tutorial on regularization. SIAM Review 40; 636-666.

[Nil01] Nill S (2001) : Development and application of a multi-modality inverse treatment planning system. Dissertation, Heidelberg.

[Nuc00] Nuclear Reaction Data Center network which is coordinated by the IAEA Nuclear Data Section 2000, webpage http://www.nndc.bnl.gov/exfor/exfor00.htm.

[Oel96] Oelfke U, Lam G K Y, and Atkins M S (1996): Proton dose monitoring with PET: quantitative studies in lucite. Phys. Med. Biol. 41; 177.

[Oel02] Oelfke U (2002): Physikalische Wechselwirkungen ionisierender Strahlung mit Materie. In Schlegel W, Bille J: Medizinische Physik, Band 2. Berlin / Heidelberg / New York, 33-64.

[Paa93] Paans A M J and Schippers J M (1993): Proton therapy in combination with PET as monitor: a feasibility study. IEEE Trans. Nucl. Sci. 40; 1041.

[Pag02] Paganetti H (2002): Nuclear interactions in proton therapy: dose and relative biological effect distributions originating from primary and secondary particles. Phys. Med. Biol. 47; 747.

[Pag03] Paganetti H and Gottschalk B (2003): Test of GEANT3 and GEANT4 nuclear models for 160 MeV protons stopping in CH2.Med. Phys. 30; 1926-31.

[Pag04] Paganetti H, Jiang H, Lee S-Y et al (2004): Accurate Monte Carlo simulations for nozzle design, commissioning and quality assurance in proton radiation therapy. Med. Phys. 31; 2107-2118.

[Pag08] Paganetti H, Jiang H, Parodi K, Slopsema R, Engelsman M (2008). Clinical implementation of full Monte Carlo dose calculation in proton beam therapy. Phys Med Biol.53(17); 4825-53.

[Par00] Parodi K and Enghardt W (2000): Potential application of PET in quality assurance of proton therapy. Phys Med 45(11); N151-6.

[Par02] Parodi K, Enghardt W and Haberer T (2002): In-beam PET measurement of β^+-radiioactivity induced by proton beams. Phys. Med. Biol. 47;21-36.

[Par04] Parodi K (2004): On the feasibility of dose quantification with in-beam PET data in radiotherapy with 12C and proton beams. Wissenschaftlich-Technische Berichte FZR415.

[Par05] Parodi K, Pönisch and Enghardt W (2005): Experimental study on the feasibility of in-beam PET for accurate monitoring of proton therapy. IEEE Trans. Nucl. Sci. 52; 778-86.

[Par06] Parodi K and Bortfeld T (2006): A filtering approach based on Gaussian-powerlaw convolutions for local PET verification of proton therapy. Phys Med Biol.51(8); 1991-2009.

[Par07a] Parodi K, Paganetti H, Cascio E, Flanz J B, Bonab A, Alpert N M, Lohmann K and Bortfeld T (2007): PET/CT imaging for treatment verification after proton therapy- a study with plastic phantoms and metallic implants. Med. Phys. 34; 319-435.

[Par07b] Parodi K, Paganetti H, Shih H, Michaud S, Loeffler J S, DeLaney F T, Liebsch N J, Munzenrider J E, Fishman A J, Knopf A and Bortfeld T (2007): Patient study on in-vivo verification of beam delivery and range using PET/CT imaging after proton therapy. Int. Journal of Radiation Oncology, Biology, Physics 68(3); 920-934.

[Par07c] Parodi K, Ferrari A, Sommerer F, Paganetti H (2007): Clinical CT-based calculations of dose and positron emitter distributions in proton therapy using the FLUKA Monte Carlo code. Phys Med Biol. 52(12); 3369-87.

[Par08] Parodi K, Bortfeld T, Haberer T (2008): Comparison between in-beam and offline positron emission tomography imaging of proton and carbon ion therapeutic irradiation at synchrotron- and cyclotron-based facilities. Int J Radiat Oncol Biol Phys. 71(3); 945-56.

[PDS08] http://www.photodetection.com.

[Psh06] Pshenichnov I, Mishustin I, Greiner W (2006): Distributions of positron-emitting nuclei in proton and carbon-ion therapy studied with GEANT4. Phys Med Biol. 51(23); 6099-112.

[Poe04] Pönisch F, Parodi K, Hasch B G, and Enghardt W (2004): The description of positron emitter production and PET imaging during carbon ion therapy. Phys. Med. Biol. 49; 5217-32.

[Ric72] Richardson, William Hadley (1972): Bayesian-Based Iterative Method of Image Restoration. JOSA 62 (1); 5559.

[Ryu08] Ryu H, Song E, Lee J and Kim J (2008): Density and spatial resolutions of proton radiography using a range modulation technique. Phys Med Biol. 53(19); 5461-8.

[Saj85] Sajjad M, Lambrecht R M and Wolf A P (1985): Cyclotron Isotopes and Radiopharmaceuticals. XXXVI. Investigation of Some Excitation Functions for the Preparation of 15O,13N and 11C. Radiochimica Acta 38; 57.

[Sch98] Schaffner B and Pedroni E (1998): The precision of proton range calculation in proton radiotherapy treatment planning: experimental verification of the relation between CT-HU and proton stopping power. Phys. Med. Biol. 43; 1579-1592.

[Schn95] Schneider U and Pedroni E (1995): Proton radiography as a tool for quality control in proton therapy. Med. Phys. 22; 35363.

[Schn96] Schneider U, Pedroni E, Lomax A (1996): The calibration of CT Hounsfield units for radiotherapy treatment planning. Phys. Med. Biol. 41: 111-124.

[Schn00] Schneider W, Bortfeld T, Schlegel W (2000): Correlation between CT numbers and tissue parameters needed for Monte Carlo simulations of clinical dose distributions. Phys. Med. Biol. 45: 459-478.

[Schn04] Schneider U, Besserer J, Pemler P, Dellert M, Moosburger M, Pedroni E and Kaser-Hotz B (2004): First proton radiography of an animal patient. Med. Phys. 31; 104651.

[Seo06] Seo K, Kim C and Kim J (2006). Korean Phys. Soc. 48; 855.

[Shi08] Shih H, Knopf A, Parodi K, Paganetti H, Bortfeld T (2008): PET/CT Treatment Verification after Proton Therapy in Abdominopelvic Tumor Sites. Abstract, 50th ASTRO Meeting Boston.

[Sur06] Surti S, Karp J S, Popescu L M, Daube-Witherspoon ME and Werner M (2006): Investigation of Time-of-Flight Benefit for Fully 3-D PET. IEEE Transactions on Medical Imaging 25; 529-538.

[Thi06] Thilmann C, Nill S, Tcking T, Hss A, Hesse B, Dietrich L, Bendl R, Rhein B, Hring P, Thieke C, Oelfke U, Debus J and Huber P.(2006): Correction of patient positioning errors based on in-line cone beam CTs: clinical implementation and first experiences. Radiat Oncol. 24;1-16.

[Tom03] Tomitami T, Pawelke J, Kanazawa M et al. (2003): Waschout studies of ^{11}C in rabbit thigh muscle implanted by secondary beams of HIMAC. Phys. Med. Biol. 48; 875-889.

[Vyn93] Vynckier S, Derreumaux S, Richard F, Bol A, Michel C and Wambersie A (1993): Is it possible to verify directly a proton-treatment plan using positron emission tomogaphy?. Radiother. Oncol. 26; 275.

[UoA] University of Alabama at Birmingham Comprehensive Cancer Center, History of Radiation Oncology.

[Uri86] Urie M, Goitein M, Holley W R and Chen G T Y (1986): Degradation of the Bragg peak due to inhomogeneities. Phys. Med. Biol. 31.1; 1-15.

[Vas60] Vastupal Parikh (1960). Absolute cross-sections of C12(p,pn)C11 from 288 to 383 MeV. Nuclear Physics 18; 628.

[Wam99] Wambersie A (1999). Reference RBE and clinical RBE: applications of these concepts in hadron therapy. Strahlenther. Onkol. 175; 39.

[Who06] WHO (2006). Cancer. World Health Organization. Retrieved on 2007-06-25.

[Wie89] Wienhard W, Wagner R and Heiss W-D (1989): Grundlagen und Anwendungen der Positronen-Emissions-Tomographie. Springer Verlag, Berlin.

[Wil46] Wilson RR (1946): Radiological use of fast protons. Radiology 47; 487-491.

[Win01] Wintermark M, Thiran JP, Maeder P, Schnyder P, Meuli R (2001): Simultaneous measurement of regional cerebral blood flow by perfusion CT and stable Xenon CT: a validation study. AJNR Am J Neuroradiol 22; 905914.

[Xu08] Xu F, Wang J, Bai S, Xu QF, Shen YL and Zhong RM(2008):Interfractional and Intrafractional Setup Errors in Radiotherapy for Tumors Analyzed by Cone-beam Computed Tomography. Ai Zheng. 27(10):1111-6.

[Zha07] Zhang X, Dong L, Lee AK, Cox JD, Kuban DA, Zhu RX, Wang X, Li Y, Newhauser WD, Gillin M and Mohan R (2007):Effect of anatomic motion on proton therapy dose distributions in prostate cancer treatment. Int J Radiat Oncol Biol Phys. 67(2); 620-9.

ACKNOWLEDGMENT

I would like to thank my supervisors Thomas Bortfeld, Harald Paganetti, Uwe Oelfke and Katia Parodi for providing me the exceptional opportunity to work on this subject. I always enjoyed working with them and their comments and encouragements made the last three years the most productive and successful of my life.

I am grateful to all colleagues in the Departments of Radiation Oncology at DKFZ and MGH who made the last three years also a very enjoyable period in my life. In particular, I would like to thank Helen Shih and Martijn Engelsman for their exceptional helpfulness and their valuable support in countless situations.

I would like to thank the Department of Radiology at MGH for their fruitful collaboration, especially Ali Bonab and Diane Crowley for their never tiering efforts to keep the project alive.

My more private thank goes to my friends and family. Special thanks goes to Jule. Our paths of life directed us both to Boston, and in countless moments during the last three years I was deeply grateful to have her close by. I would like to thank Moni for her wonderful and loyal friendship despite the great distance. In many moments I would have been lost without her always open ears and her always wise advise. I would like to thank my parents, my brother, my grandparents, aunts and uncles for all the love and support and for being present from the long distance.

Finally, I would like to thank Andy, who is always in my heart. Despite the distance I feel that we have grown closer and stronger during the last three year. He always gave me a feeling of security, I hope the future will give us the chance to also live this security.

ERKLÄRUNG

Hiermit versichere ich, dass ich die vorliegende Arbeit ohne unzulässige Hilfe Dritter und ohne Benutzung anderer als der angegebenen Hilfsmittel angefertigt habe; die aus fremden Quellen direkt oder indirekt übernommenen Gedanken sind als solche kenntlich gemacht. Die Arbeit wurde bisher weder in Inland noch im Ausland in gleicher oder ähnlicher Form einer anderen Prüfungsbehörde vorgelegt.

Heidelberg, den 09.02.2009